PERFORMANCE STUDY FOR GUIDANCE OF A MISSILE USING FLOW EFFECTORS AT DIFFERENT ROLL ANGLE POSITIONS

PREPARED FOR

DEFENCE R&D CANADA – VALCARTIER
R&D POUR LA DÉFENSE CANADA - VALCARTIER
QUEBEC, QC G3J-1X5 CANADA
Contract No. : W7701-0-24237/001/QCA PO 41888
Nicolas Hamel, Scientific authority
Tel : 418-844-4000 ext. 4663

by

P.-A. Rainville
P. Gosselin

NUMERICA TECHNOLOGIES

NUMERICA TECHNOLOGIES INC.
3420, Lacoste Street
Québec, QC G2E-4P8 Canada

December / Décembre 2004

ABSTRACT / RÉSUMÉ

This project was part of DRDC technology investment found (TIF) project "Supersonic Missile Flight Control by Manipulation of the Flow Structure using Micro-Actuated Surfaces". The objective was to evaluate the performance of an active flow control in the form of a rectangular flow effectors and knife-edge flow effectors with the aim of controlling a missile. Flow effectors at different roll angle positions on the surface of the missile nose were evaluated numerically for their impact on overall system performance for a missile flying at angles of attack from five to twenty degrees.

A series of CFD analyses were carried out on an aerodynamic geometry with two different shapes of flow effectors. For the knife-edge flow effectors, five roll angle positions were analyzed. Seven roll angle positions with one rectangular flow effector and three roll angle positions with three rectangular flow effector were analysed. The experience gained during previous work was used as a guideline for determining the meshing strategy to be adopted, the turbulence model to be used with the correct near wall model with a Y+ around 1. From the gained experience, the mesh should be very fine and structured near the wall with a smooth mesh variation in the vortex perturbed region. The more accurate turbulence model was the realizable k-epsilon.

The calculations showed that a good side force generation was possible for one flow effector at roll angle position between 225 degrees and 270 degrees. Those results correlated well with wind tunnel measurement between 5 degrees and 15 degrees angle of attack. Calculations with three flow effectors showed a small improvement in the performance compared to the best performing single flow effector configuration. Finally, knife-edge flow effectors did not produce the same aerodynamic coefficients as the rectangular flow effector.

Ce projet fait parti du projet "Contrôle de vol d'un missile supersonique par manipulation des structures de l'écoulement en utilisant des surfaces avec micro-actuateur" de RDDC - Valcartier supporté par un fond d'investissement technologique (TIF). L'objectif du projet consistait à évaluer la performance des systèmes de contrôle de vol sous la forme d'un perturbateur d'écoulement rectangulaire ainsi que d'un perturbateur d'écoulement à coin biseauté dans le but de contrôler un missile. Des perturbateurs d'écoulement ont été placés à différentes positions angulaires de roulis sur la paroi d'un missile pour évaluer numériquement leur impact sur les performances. Ces simulations ont été exécutées avec un missile volant à un nombre de Mach de 1,5 avec des angles d'attaque variant entre cinq et vingt degrés.

Une série de simulations ont été exécutées sur une géométrie aérodynamique avec deux formes différentes de perturbateurs d'écoulement. La force latérale générée par les perturbateurs d'écoulement doit être suffisante pour faire tourner un missile. Pour les perturbateurs d'écoulement à coin biseauté, cinq positions angulaires de roulis ont été analysées. Sept positions angulaires de roulis pour un seul perturbateur d'écoulement rectangulaire ont été analysées alors que trois positions angulaires de roulis ont été analysées pour les groupes de trois perturbateurs d'écoulement. Les modèles et les ajustements ont été faits en se basant sur l'expérience acquise durant les projets précédents. La validation a été améliorée à l'aide des mesures préliminaires de la soufflerie qui ont été

présentées durant la deuxième réunion concernant le contrôle de missile avec des perturbateurs à micro-actuateur [Wong (2004)].

Les simulations montrent qu'une bonne génération de force latérale était possible avec un perturbateur rectangulaire à une position angulaire de roulis variant entre 225 degrés et 270 degrés. Ces résultats concordent bien avec les mesures pour la soufflerie entre 5 et 15 degrés d'angle d'attaque. Les simulations avec trois perturbateurs ne montrent qu'une faible amélioration de la performance comparée au perturbateur le plus efficace des trois. Finalement, les perturbateurs d'écoulement à coins biseautés ne génèrent pas les mêmes résultats pour les coefficients aérodynamiques que les perturbateurs d'écoulement rectangulaires.

TABLE OF CONTENTS

LIST OF FIGURES

LIST OF TABLES

NOMENCLATURE

c.g.	Centre of gravity	
C_A	Axial force coefficient	
C_l	Rolling moment coefficient	
C_m	Pitching moment coefficient	
C_n	Yawing moment coefficient	
C_N	Normal force coefficient	
C_p	Pressure coefficient	
C_Y	Side force coefficient	
L_W	First cells height	m
V_W	Velocity near the wall	m/s
x	Axial coordinate (North)	m
y	Side coordinate (East)	m
z	Normal coordinate (Down)	m
Y^+	Dimensional less height	
X_{cp}	Normal force, centre of pressure	
Y_{cp}	Side force, centre of pressure	
α	Angle of attack (AOA)	degrees
ϕ	Roll angle position	degrees
μ	Viscosity	kg/m s
μ_W	Viscosity near the wall	kg/m s
ρ	Density	kg/m³
ρ_W	Density near the wall	kg/m³
AOA	Angle of attack	
CFD	Computational Fluids Dynamics	
CFL	Courant-Freidrich Lewis number	
DRDC	Defence Research & Development Canada	
FE	Flow effectors	
KFE	Knife edge flow effectors	
MEMS	Micro Electro-mechanic systems	
TIF	Technology investment found	
WO FE	Without flow effectors	
W-T FE	Wind tunnel results with rectangular FE	

EXECUTIVE SUMMARY

The DRDC Valcartier Flight Mechanics Group is responsible for research in aerodynamic and flight dynamic behavior of weapon systems. To overcome some of the physical or financial constraints imposed by experiments, a Computational Fluid Dynamics (CFD) approach can be used to complement and enhance experimental results.

The objective of the contract was to evaluate the performance of an active flow control in the form of a rectangular flow effectors and a knife-edge flow effectors with the aim of controlling a missile. Using CFD, flow effectors at different roll angle positions on the surface of the missile were evaluated for their impact on overall system performance for a missile flying at Mach 1.5 at wind tunnel conditions for angle of attack from five to twenty degrees.

A series of CFD analysis were made on an aerodynamic geometry with some flow effectors. Two different shapes, knife-edge and rectangular, of Flow Effectors were evaluated for their side force performance. The side force generated by the Flow Effectors should be able to steer a missile. For the knife-edge flow effectors, five roll angle positions were analyzed (210°, 240°, 270°, 300°, 330°). Seven roll angle positions with one rectangular flow effectors were calculated (210°, 225°, 240°, 270°, 300°, 315°, 330°) and three roll angle position with three rectangular flow effectors were calculated (225°, 270°, 315°). The flow effectors were located at 2,53 cm (0,997 inches) from the nose tip. The experience gained during previous work was used as a guideline for determining the models and setting. The validation was improve with preliminary wind tunnel measurements presented during the second meeting on missile control using micro actuated flow effectors [Wong (2004)]. Finally, recommendations for improvements of the performance were stated.

This project was part of DRDC technology investment found (TIF) project "Supersonic Missile Flight Control by Manipulation of the Flow Structure using Micro-Actuated Surfaces". It resulted in an improved capability to predict numerically the aerodynamic behavior of rectangular Flow Effectors before they can be tested in DRDC Valcartier wind tunnel.

1.0 INTRODUCTION

Flow effectors (FE) are integrated devices located in strategic places on the surface of a missile. These systems can control and actuate in the micro scale of the flow, and they function individually or in arrays to generate effects on the macro scale flow. In the most general form, MEMS consist of mechanical microstructures, micro sensors, micro actuators and electronics integrated in the same environment (i.e. on a silicon chip). Miniaturization of mechanical systems promises unique opportunities for new directions of scientific and technological progress.

Missile guidance permits an increase in lethality for combat superiority. The performance of this system is function of the execution quality of this command. The majority of missiles use aerodynamic surfaces to accomplish this work. The control with the thrust vector constitutes another strategy for missile control. Nevertheless, these systems require a structure and an actuator. This implies number of systems to accomplish the task, which reduces the reliability and increases the weight of the mechanism. Aerodynamic surfaces need a relatively important space for storage. Removing conventional controls could lead to significant weight reductions or decrease the missile signature.

The present work analyses rectangular FE and knife-edge FE, which are placed at different positions around the nose. Side force measured by Corriveau (2004) indicated a good performance of the FE. Calculations done by Rainville and Gosselin (2004) presented a good correlation for side force with measurement up to 10 degrees of angle-of-attack (AOA). Hamel (2004) had determined that the k-ε model is better to capture side force. A general objective of research about FE is to investigate the position and the number of FE needed on the surface of a missile to obtain sufficient control authority for effective guidance during flight. This project was part of DRDC technology investment found (TIF) project "Supersonic Missile Flight Control by Manipulation of the Flow Structure using Micro-Actuated Surfaces".

The aim of this study was achieved by a Computational Fluid Dynamics (CFD) analysis. The commercial CFD code Fluent™ was used to accomplish these calculations. One should note that the meshing for every CFD simulation was generated with the commercial code Gambit™. Experience gained during the previous work [Rainville and Gosselin (2004)] was used as a guideline.

This document is divided in three parts. At first, a description of the flow effectors, their positions, their dimensions and the different angles of attack that were used are described. Presentation of the results was done accordingly. In the third part, an analysis of the results is given and a discussion is presented. Finally, a conclusion and suitable recommendations are given in the last section.

2.0 METHODOLOGY

The methodology for a Computational Fluid Dynamics (CFD) study includes the model used, the description of the grid and the parameters set in the boundary condition. Normally, a complete validation study must be undertaken to gain confidence in the numerical results. Those numerical results are then compared to the experimental results. In this case, no complete experimental data was available for comparison. The present methodology was established from the experience gained in previous studies [DeChamplain et al. (2002)], [Rainville and Gosselin (2004)], and also by the information presented [Wong (2004)]. In the previous work, the side force was under-predicted for angles of attack (AOA) over 10 degrees. The information about the various models available in Fluent™ will not be given in this report. Nonetheless, it could be useful to indicate briefly some parameters that were selected for the present simulations. Finally, a mesh refinement was done in the boundary layer to obtain a better correlation with the wind tunnel results that were presented.

2.1 Geometry

The FE were fixed on the nose of a cylinder body with a conical nose. The diameter of the geometry was 30 mm. The conical part of the geometry was 90 mm in length and the cylindrical part was 300 mm in length. The total length of the geometry was 390 mm (15,353 inches). Figure 1 presents the body alone geometry. The axis of origin was at the base of the geometry. Wong (2004) had specified the coordinate system orientation to a north, east down coordinate system. Figure 2 presents the coordinate system orientation. The red arrows represent the coordinate system and the green arrows present the aerodynamic coefficients vectors.

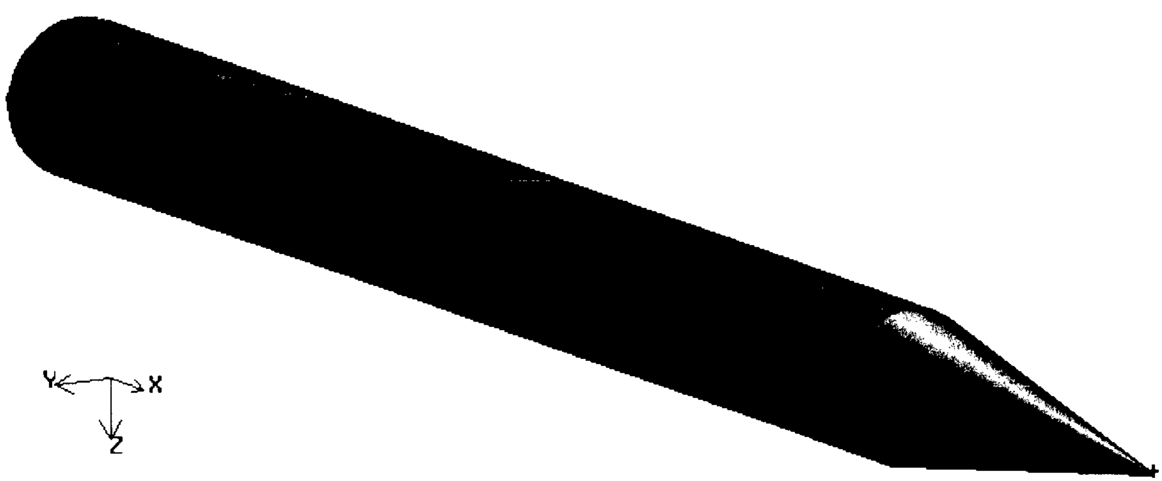

Figure 1 : Body alone geometry with the axis orientation

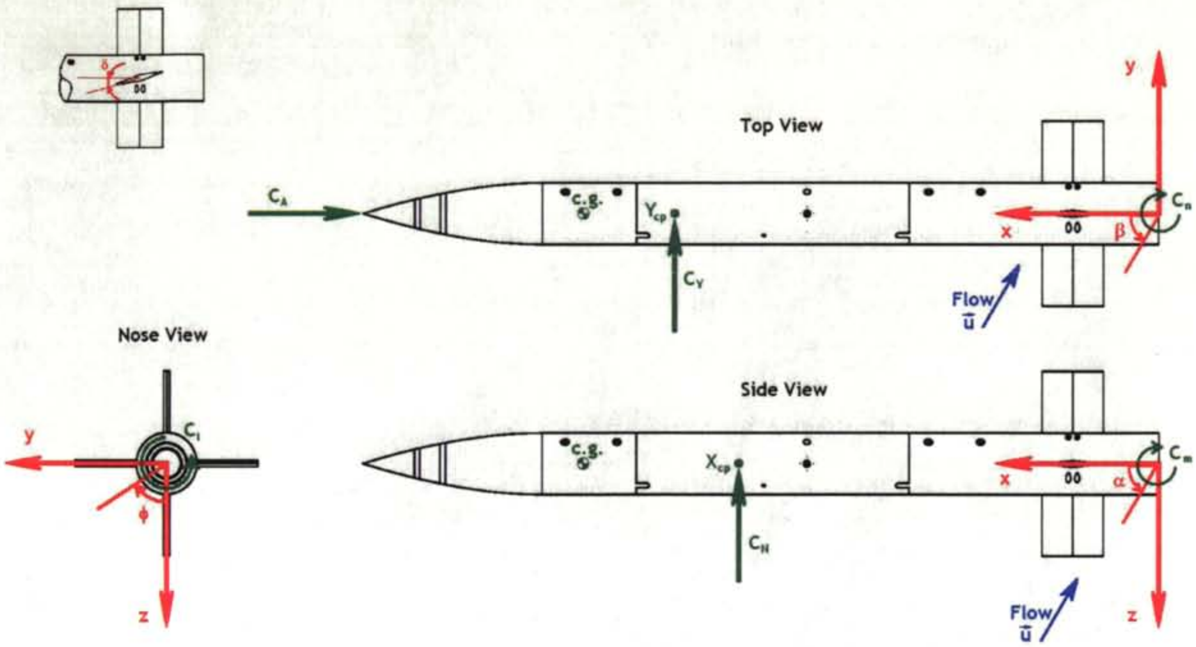

Figure 2 : North, east, down reference coordinate system

The FE were placed around the body at 25,3 mm (0,997 inches) from the nose tip. The position of the FE around the body was defined by ϕ_{FE}, which was defined as the roll angle position. The baseline FE geometry was a rectangle. It was approximately 1 mm (0,0394 in) high, 2,67 mm long (0,105 in) and 0,78 mm (0,031 inches) in width. Figure 3 presents an isometric view of the baseline FE.

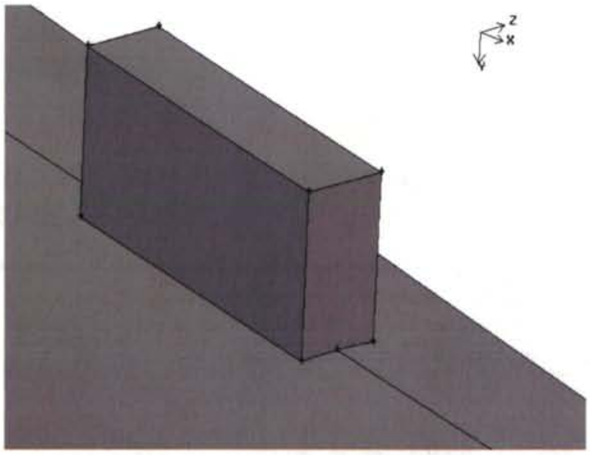

Figure 3 : Isometric view of the baseline FE

It was decided to analyse another geometry that would be easier to mesh. This geometry was named as the knife-edge FE. The leading edge and the training edge were cut over a third of the length to build the first design of the knife-edge FE. The knife-edge FE was almost the same dimension than the baseline FE. The geometry was similar to a small wing. Figure 4 presents an isometric view of the first knife-edge FE geometry on the missile. With this FE, the mesh was easier to build in the boundary layer up to the FE high. At the upper FE, the mesh became very difficult to build, and the

mesh quality became a problem. Since the aim of this knife-edge FE was to be easier to mesh than the baseline FE, the geometry was not calculated.

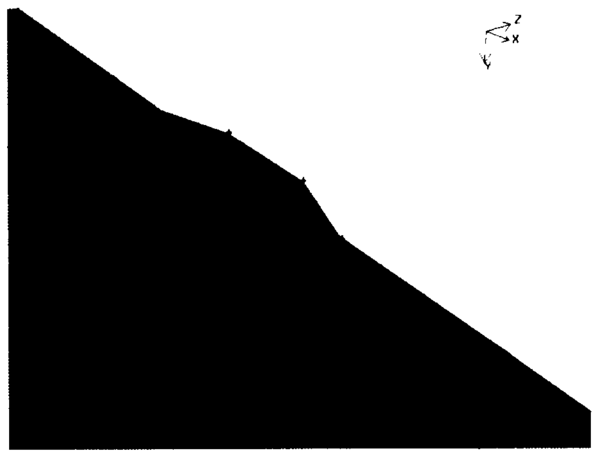

Figure 4 : Isometric view of the first knife edge FE

A second knife-edge FE geometry was built to simplify the mesh. The leading edge, the trailing edge and the top edge were sharpened with an angle of 50 degrees as shown on figure 5. The dimension of the knife-edge FE was approximately the same as the baseline FE. Figure 6 presents an isometric view of the second knife-edge FE geometry. The shape of the second knife-edge FE was more similar to the baseline FE. It was possible for this FE to be used as a design geometry to accelerate the development of a guiding system.

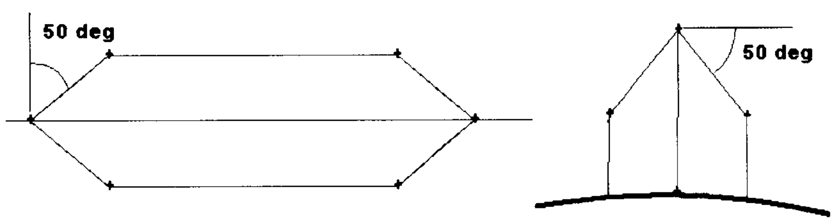

Figure 5 : Cutting plane to obtain the second knife edge FE

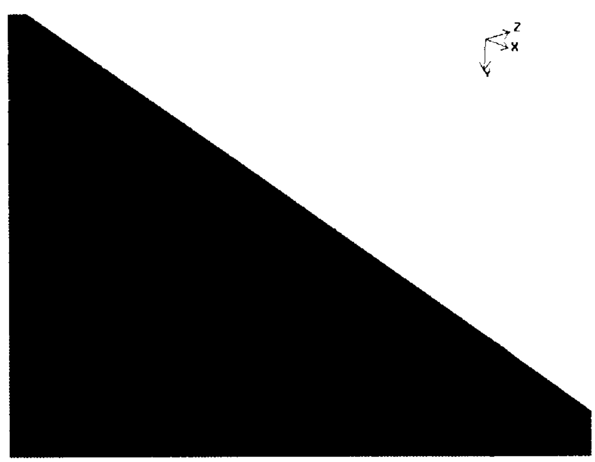

Figure 6 : Isometric view of the second knife edge FE

To improve the side force generated by the baseline FE, it was possible to group them. In the present work, only a group of three FE placed with 30 degrees between them were calculated. Figure 7 presents an isometric view of the three FE.

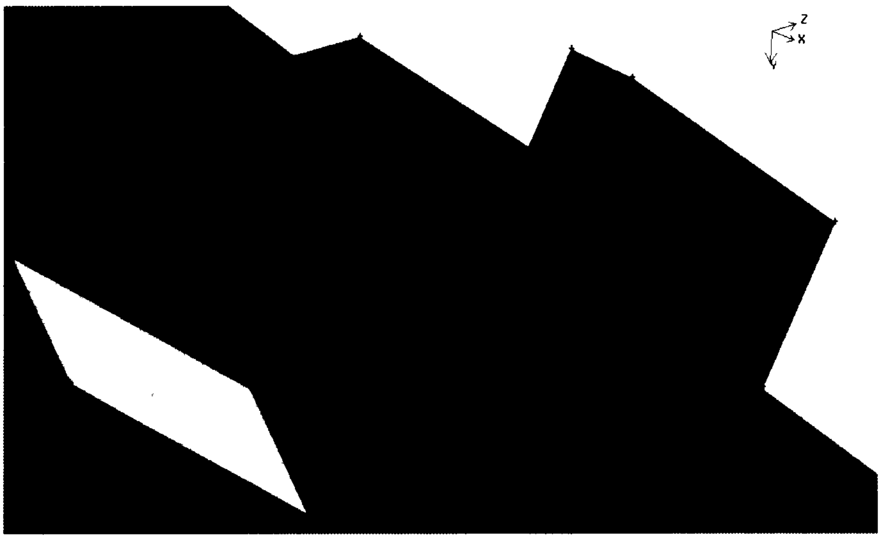

Figure 7 : Isometric view of three FE at 30 degrees

2.2 Model

Fluent™ include many parameters for calculation purposes and all the possibilities will not be described here. In the present simulations, Navier-Stokes equations are resolved with the coupled form of the code where the energy equation is solved simultaneously with the fluid equations. Those equations are solved with an explicit pseudo-time formulation. This formulation calculates more rapidly and need less computer memory.

Hamel (2004) concluded that the k-ε turbulence model with a structured grid was the most successful option to predict the side force. Calculations done in the preliminary work showed a very small difference between the Realizable k-ε and the RNG k-ε model. The realizable k-ε model was adopted because its robustness. Finally, the effects of the boundary layer were evaluated with the Enhanced-Wall treatment model. This model proposes two options to improve the calculation. Only the pressure one was activated, because the thermal heat transfer was not calculated. The working fluid was air. Density was calculated with the ideal-gas law and viscosity, with the Sutherland three coefficients model. All other properties stayed at default settings.

Convergence of the solution was normally defined, in Fluent™, with the reduction of the residuals for the main flow parameters, which were continuity, x, y and z velocity, energy, and turbulence variables, which were k and ε. For the present work, the convergence also included the side force variation. At every 50 iterations, the side force was reported. If the variation of the side force was under 0,5 % for 100 iterations, the calculation was considered converged.

2.3 Boundary conditions

The calculation domain was surrounded by a pressure far-field boundary condition in front and around it. The outlet of the domain was determined by a pressure outlet boundary condition to reduce boundary condition effects and to be sure that no shock wave reflection could exist. The missile had a free steam Mach number of 1,5. The static temperature was 206 K and the static pressure was 26 000 Pa. Furthermore, four angles-of-attack (AOA) were selected for calculations: 5, 10, 15 and 20 degrees.

2.4 Grids

In accordance with previous MEMS studies, grids generated were built with cubic cells. In previous works, computers systems did not permitted to use a mesh bigger than 1,2 million cells. It was not possible to perform a mesh independence study. The first step of this work was to run a mesh independence study. An important mechanism to generate side force is to create asymmetric vortices. The refinement of the near wall mesh was high enough for the turbulence model. In the far field, the mesh was coarse to accelerate the calculation. The near wall zone was meshed with a structured boundary layer mesh. The far field mesh was built with an unstructured quad mesh to permit a transition between the refine mesh near the wall and a more coarse mesh in the far field. In the first calculation, the transition between the structured boundary layer and the far field was really strong at the back of the missile. This strong transition in the mesh could explain the small side force calculated, because the vortices could be lost within the transition. Figure 8 presents this mesh transition at the back of the missile. A layer that group mesh cells was tried outside the boundary layer mesh to solve this problem. But, this layer caused a lot of skewness in the mesh, without reducing the transition problem.

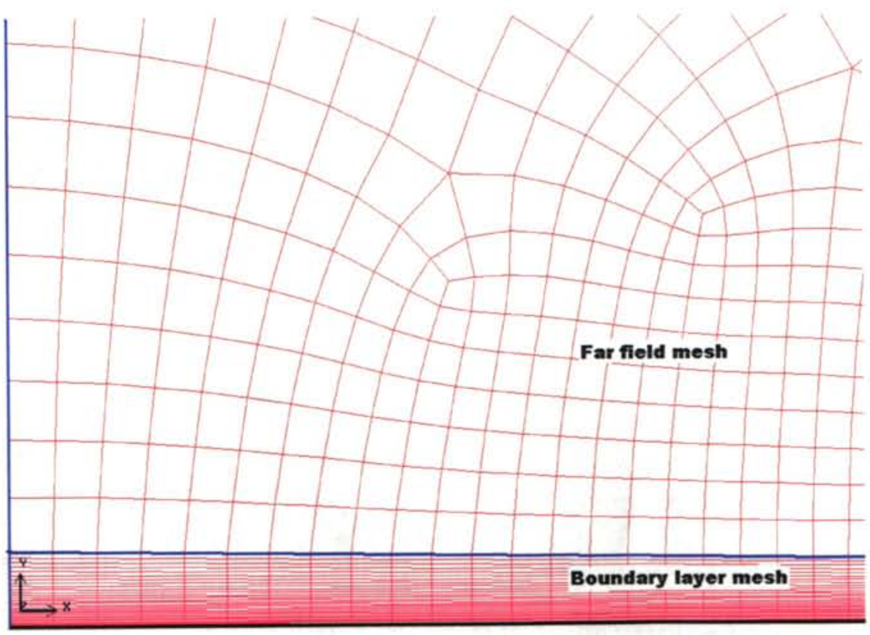

Figure 8 : First mesh transition at the back of the missile

To be sure that the vortices were well propagated, a new mesh strategy for the far field included a structured layer between the boundary layer and the far field mesh. This layer permitted a smooth transition and was big enough so the vortices could be propagated in a structured mesh. Figure 9 presents the mesh transition used at the back of the missile. In the mesh strategy, a skewness criterion was applied mainly in the region around the FE. The skewness in the mesh should be under 0,6 to reduce mesh perturbation. Figure 10 shows that the vortices were propagated mostly in the transition layer. In the figure, the circle shows the limit between the transition layer mesh and the far field mesh. A calculation with one rectangular FE placed at a roll angle position of 240 degrees and an AOA of 20 degrees measured at the back of the missile was used to present the limit on the figure.

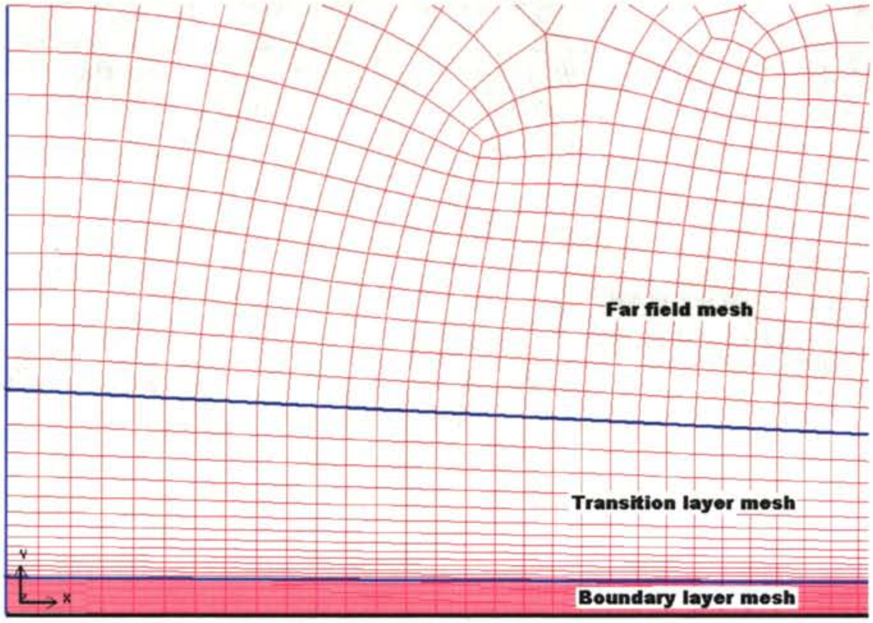

Figure 9 : Second mesh transition at the back of the missile

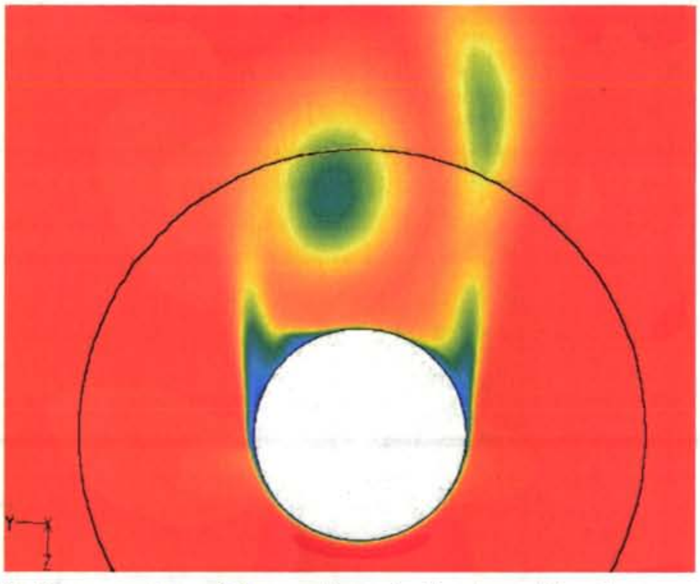

Figure 10 : Propagation of the vortices in the transition layer on the exit

Aerodynamic coefficients for the numerical solution and the wind tunnel measurements were compared for the case of one FE placed at a roll angle position of 270 degrees with an AOA of 15 degrees. Coefficients for the wind tunnel measurements with one FE placed at a roll angle of 90 degrees were also included, but to simplify performance comparison, the sign of the side force was changed. Table 1 compares these aerodynamic coefficients. The numerical solution was between the two experimental measurements. This coherence between the solutions proposes a good validation of the solution.

Table 1 : Comparison of the aerodynamic coefficients between wind tunnel measurements and numerical solution

	C_A	C_Y	C_N	C_l	C_m	C_n
Measure 90	0.3059	0.1681	0.9349	-0.0031	8.8387	0.4986
Measure 270	0.3053	0.2666	0.9584	-0.0032	9.0736	0.9730
Numerical	0.2351	0.2273	1.2891	0.0003	10.4974	0.8446

All grids that were related to FE needed some refinement in the grid in their vicinity. Since the Enhanced-Wall treatment was used, the mesh had to have a Y^+ parameter around 1 over the entire missile wall. With supersonic shock waves, it is difficult to establish a Y^+ with the same value over the entire missile. An effort was made to have a more favourable Y^+ on the FE device and region. In the results tables, the Y^+ was calculated over the entire missile and around the FE region as a mean Y^+. It may be important to remember that the Y^+ parameter is calculated like a Reynolds number at the first cell near the wall. Equation 1 is used to calculate the Y^+ value. This value is normally calculated by Fluent™ code. This equation includes density ρ_W, velocity V_W, height of the first cells L_W and viscosity μ_W. All those values were calculated at the first cell near the wall.

$$Y^+ = \frac{\rho_W V_W L_W}{\mu_W} \qquad [1]$$

At the beginning of this work, many mesh strategies were used to improve the mesh quality, and to obtain a more coherent side force. The goal to obtain a better mesh strategy did not solve the problem of the mesh independence. For every group of calculation, a mesh independence study was done. The first step was done with a mesh with 120 grid intervals all around. The second step used 160 grid intervals and the last step used 200 grid intervals. The first mesh included approximately 1,5 millions cells, the second, 3,3 millions and the third mesh included around 6,7 millions cells. Results of the mesh independence are presented with calculations results. Additional figures are presented in appendix A. Those figures present the configuration of the calculation domain and mesh around FE for the 160 grid intervals used in the calculations.

3.0 RESULTS

In this work, results included aerodynamic coefficients and pressure profiles over the body. For each FE geometries, validation results, mesh Y^+ parameter, FE position and aerodynamic coefficients are presented. Finally, the strategy to group the wall pressure profile data over the body will be presented. Some contour profiles of the flow are included in appendix B. Plots of pressure profiles at the pressure taps are included in appendix C.

3.1 Without FE

Calculation without the FE was done to evaluate the mesh. With an homogeneous mesh, the missile should not generate any side force. The calculations without the FE were done with the mesh used for the calculation with one rectangular FE. The volume around the FE was modified to remove the solid zone of the FE. Table 2 presents the calculation characteristics and table 3 presents the aerodynamic coefficients for those calculations.

Table 2 : Without FE calculation characteristics

Name	Mesh		AOA
	Nb cells	Y^+ (All)	
WO FE-A05	3389138	0.83	5
WO FE-A10	3389138	0.87	10
WO FE-A15	3389138	0.89	15
WO FE-A20	3389138	0.90	20
WO FE-A25	3389138	0,91	25
WO FE-A30	3389138	0,91	30

Table 3 : Aerodynamic coefficients for calculation without FE

Name	Forces			Moments			Pressure centre	
	C_A	C_Y	C_N	C_l	C_m	C_n	X_{cp}	Y_{cp}
WO FE-A05	0.244	-0.000	0.246	0.000	2.413	-0.000	9.82	3.05
WO FE-A10	0.245	-0.000	0.642	0.000	5.609	-0.002	8.74	5.21
WO FE-A15	0.233	0.007	1.279	0.000	10.456	0.021	8.17	2.89
WO FE-A20	0.211	0.018	2.505	0.000	19.357	0.080	7.73	4.35
WO FE-A25	0,194	-0,019	4,200	0,000	30,401	-0,099	7,24	5,19
WO FE-A30	0,186	-0,012	6,220	0,000	42,325	0,040	6,80	-3,20

Calculations show that a small side force was generated. The small cells stretched around the normal FE position can explain this. The side force increase appeared to be gradual with the AOA. At an AOA of 20 degrees, the factor C_Y / C_N had a value of 0,7 %, which was relatively small.

3.2 Knife-edge FE

The first step of the calculation was the mesh independence. The mesh independence was done with a knife-edge FE placed at a roll angle of 270 degrees with an angle of attack of 15 degrees. Table 4 presents the mesh characteristics and table 5 presents the aerodynamic coefficients for the mesh. Table 6 presents the difference between the aerodynamic coefficients for mesh independence study. Calculations were compared to the second mesh. In this table, the knife-edge geometry is referred as KFE and the V1, V2 and V3 are referred as the version of the mesh.

Table 4 : Mesh characteristics for mesh independence with the knife-edge FE

Name	Mesh			
	Distribution	Nb cells	Y^+ (FE)	Y^+ (All)
KFE V1	120	1442395	1.11	0.89
KFE V2	160	3389138	1.11	0.90
KFE V3	200	6702396	1.10	0.90

Table 5 : Aerodynamic coefficients for mesh independence with the knife edge FE

Name	Forces			Moments			Pressure centre	
	C_A	C_Y	C_N	C_l	C_m	C_n	X_{cp}	Y_{cp}
KFE V1	0.234	0.210	1.305	0.000	10.593	0.783	8.12	3.73
KFE V2	0.234	0.222	1.289	0.000	10.492	0.811	8.14	3.69
KFE V3	0.235	0.221	1.271	0.000	10.429	0.812	8.21	3.68

Table 6 : Difference between the mesh independent calculations with the knife-edge FE

Difference	Forces		
	C_A	C_Y	C_N
KFE V2 vs KFE V1	0.28 %	4.55 %	1.28 %
KFE V2 vs KFE V3	0.33 %	0.43 %	1.38 %

The side force difference between the first mesh and the second mesh was around 4,5 %, which was too high for the mesh independence, because it was higher than 1 %. The difference for the aerodynamic coefficients between the second mesh and the third mesh was small enough to have mesh independence. These results defined that the second mesh could be used for the calculations with the knife-edge FE at every position. A plot of the side force with the number of iterations was done in appendix B. On this plot, the first optimum point for the side force was the converged solution with the side force criterion. Calculations with the knife-edge FE needed approximately 3500 iterations to converge and the continuity criteria was around to 1×10^{-4}.

With the mesh independence completed, calculations for every configuration with the knife-edge FE could be done. Table 7 presents the mesh characteristics, FE characteristics and the angle of attack. Since all calculations were done with the same mesh, table 7 only includes the Y^+ around the FE and over the entire body. The distribution and the number of cells were the same as the KFE V2 calculation in the mesh independence study. Number, type and roll angle position of the FE defined

the characteristic of FE. Table 8 includes the aerodynamic coefficients and centre of pressure for the knife-edge calculations. The name of the calculation includes the type of FE, the roll angle position of the FE and the angle of attack.

Table 7 : Knife-edge FE calculation characteristics

Name	Mesh		Flow Effectors	AOA
	Y^+ (FE)	Y^+ (All)	ϕ_{FE} (deg.)	(deg.)
KFE 210-A05	1.08	0.83	210	5
KFE 210-A10	1.05	0.87	210	10
KFE 210-A15	1.00	0.89	210	15
KFE 210-A20	0.92	0.90	210	20
KFE 240-A05	1.12	0.83	240	5
KFE 240-A10	1.10	0.87	240	10
KFE 240-A15	1.06	0.89	240	15
KFE 240-A20	1.01	0.90	240	20
KFE 270-A05	1.14	0.83	270	5
KFE 270-A10	1.14	0.87	270	10
KFE 270-A15	1.11	0.90	270	15
KFE 270-A20	1.06	0.90	270	20
KFE 300-A05	1.17	0.83	300	5
KFE 300-A10	1.18	0.87	300	10
KFE 300-A15	1.19	0.90	300	15
KFE 300-A20	1.27	0.90	300	20
KFE 330-A05	1.18	0.83	330	5
KFE 330-A10	1.21	0.87	330	10
KFE 330-A15	1.24	0.90	330	15
KFE 330-A20	1.19	0.90	330	20

Table 8 : Aerodynamic coefficients for calculation with knife-edge FE

Name	Forces			Moments			Pressure centre	
	C_A	C_Y	C_N	C_l	C_m	C_n	X_{cp}	Y_{cp}
KFE 210-A05	0.245	0.002	0.247	0.000	2.419	0.015	9.79	7.05
KFE 210-A10	0.246	0.055	0.644	0.000	5.621	0.218	8.73	3.94
KFE 210-A15	0.234	0.310	1.301	0.000	10.508	1.108	8.08	3.58
KFE 210-A20	0.211	0.477	2.571	0.000	19.516	2.106	7.59	4.42
KFE 240-A05	0.245	0.002	0.247	0.000	2.420	0.016	9.81	6.96
KFE 240-A10	0.246	0.057	0.644	0.000	5.627	0.232	8.74	4.06
KFE 240-A15	0.234	0.324	1.302	0.000	10.526	1.241	8.08	3.82
KFE 240-A20	0.211	0.648	2.606	0.001	19.651	3.020	7.54	4.66
KFE 270-A05	0.247	-0.000	0.252	0.000	2.439	0.003	9.68	-8.05
KFE 270-A10	0.247	0.027	0.650	0.000	5.659	0.121	8.70	4.49
KFE 270-A15	0.234	0.220	1.289	0.000	10.492	0.811	8.14	3.69
KFE 270-A20	0.212	0.439	2.558	0.001	19.514	2.021	7.63	4.61
KFE 300-A05	0.245	0.002	0.247	0.000	2.418	0.006	9.79	3.80
KFE 300-A10	0.246	0.030	0.644	0.000	5.618	0.093	8.73	3.07
KFE 300-A15	0.234	0.083	1.281	0.000	10.464	0.281	8.17	3.39
KFE 300-A20	0.212	0.003	2.505	0.000	19.352	0.013	7.73	3.99
KFE 330-A05	0.245	0.001	0.246	0.000	2.415	0.003	9.81	2.86
KFE 330-A10	0.246	0.029	0.645	0.000	5.620	0.099	8.71	3.38
KFE 330-A15	0.234	-0.012	1.279	0.000	10.452	-0.044	8.17	3.67
KFE 330-A20	0.212	0.133	2.511	0.001	19.374	0.604	7.72	4.54

3.3 Rectangular FE

The mesh independence was done with the rectangular baseline FE placed at a roll angle of 270 degrees with an angle of attack of 15 degrees. Table 9 presents the mesh characteristics and table 10 presents the aerodynamic coefficients for the mesh independence. Table 11 presents the differences of the aerodynamic coefficients for the independent mesh compared to the third one. In this table, the rectangular FE geometry is referred as 1 FE and V1, V2, V3 and V4 refers to the version of the mesh. The third version of the mesh had a smaller Y^+ value because a boundary layer was included in the mesh over the FE.

Table 9 : Mesh characteristic for mesh independence with one FE

Name	Mesh			
	Distribution	Nb cells	Y^+ (FE)	Y^+ (All)
1 FE V1	120	1449763	10.37	0.89
1 FE V2	160	3387890	7.14	0.89
1 FE V3	160	3387890	2.02	0.89
1 FE V4	200	6679116	5.29	0.90

Table 10 : Mesh characteristic for mesh independence with one FE

Name	Forces			Moments			Pressure centre	
	C_A	C_Y	C_N	C_l	C_m	C_n	X_{cp}	Y_{cp}
1 FE V1	0.234	0.214	1.306	0.000	10.601	0.804	8.12	3.75
1 FE V2	0.235	0.228	1.290	0.000	10.497	0.848	8.14	3.72
1 FE V3	0.235	0.227	1.289	0.000	10.497	0.845	8.14	3.72
1 FE V4	0.236	0.228	1.271	0.000	10.430	0.846	8.20	3.72

Table 11 : Difference between the mesh independence calculations with one FE

Difference	Forces		
	C_A	C_Y	C_N
1 FE V3 vs 1 FE V1	0.31 %	5.68 %	1.30 %
1 FE V3 vs 1 FE V2	0.00 %	0.27 %	0.04 %
1 FE V3 vs 1 FE V4	0.35 %	0.16 %	1.39 %

The side force difference between the first mesh and the third mesh was around 5,7 %, which is too high for the mesh independence. The difference of the aerodynamic coefficients between the other meshes is small enough to have mesh independence. The difference between the second and the third mesh is caused by the boundary layer refinement on the top of the FE. Without the refinement, the mesh had a better quality around the FE. With the refinement, two small zones with skewness appeared over the top edges of the FE. The pink cells in figure A6 of appendix A represent those two small zones of skewness. The differences between the aerodynamic coefficients for those two calculations were small enough to consider that the skewness zone did not affected the solution. Calculations for rectangular FE were done with the third mesh, which included the boundary layer refinement over the FE. This mesh was chosen to obtain a better resolution of the turbulence effect on the FE.

A plot of the side force coefficient with the number of iterations was done in appendix B. This plot showed that the solution did not converged with the side force criterion at the first optimum point. Calculations for the baseline FE needed approximately 6000 iterations to converge. The calculations were considered converged when the continuity convergence criterion was around 1×10^{-5}. Table 12 presents the mesh characteristics, the FE characteristics and the angle of attack. Table 13 presents the aerodynamic coefficients for the rectangular FE.

Table 12 : Rectangular FE calculation characteristics

Name	Mesh		Flow Effectors	AOA (deg.)
	Y^{+} (FE)	Y^{+} (All)	ϕ_{FE} (deg.)	
1 FE 210-A05	1,68	0,83	210	5
1 FE 210-A10	1,69	0,88	210	10
1 FE 210-A15	1,66	0,90	210	15
1 FE 210-A20	1,54	0,90	210	20
1 FE 225-A05	1,72	0,83	225	5
1 FE 225-A10	1,77	0,87	225	10
1 FE 225-A15	1,78	0,89	225	15
1 FE 225-A20	1,73	0,89	225	20
1 FE 225-A25	1,45	0,91	225	25
1 FE 240-A05	1,77	0,83	240	5
1 FE 240-A10	1,85	0,87	240	10
1 FE 240-A15	1,87	0,89	240	15
1 FE 240-A20	1,81	0,89	240	20
1 FE 270-A05	1,84	0,83	270	5
1 FE 270-A10	1,95	0,87	270	10
1 FE 270-A15	2,02	0,89	270	15
1 FE 270-A20	2,00	0,90	270	20
1 FE 300-A05	1,84	0,83	300	5
1 FE 300-A10	1,98	0,87	300	10
1 FE 300-A15	2,10	0,89	300	15
1 FE 300-A20	2,21	0,90	300	20
1 FE 315-A05	1,82	0,83	315	5
1 FE 315-A10	1,97	0,87	315	10
1 FE 315-A15	2,09	0,89	315	15
1 FE 315-A20	2,24	0,90	315	20
1 FE 330-A05	1,80	0,83	330	5
1 FE 330-A10	1,93	0,87	330	10
1 FE 330-A15	2,03	0,89	330	15
1 FE 330-A20	2,18	0,90	330	20

Table 13 : Aerodynamic coefficients for calculation with rectangular FE

Name	Forces			Moments			Pressure centre	
	C_A	C_Y	C_N	C_l	C_m	C_n	X_{cp}	Y_{cp}
1 FE 210-A05	0,246	0,005	0,246	0,000	2,417	0,026	9,82	5,49
1 FE 210-A10	0,247	0,073	0,643	-0,000	5,627	0,292	8,75	3,98
1 FE 210-A15	0,234	0,373	1,302	-0,000	10,504	1,382	8,07	3,70
1 FE 210-A20	0,211	0,538	2,579	0,001	19,554	2,478	7,58	4,61
1 FE 225-A05	0,246	0,005	0,246	0,000	2,419	0,030	9,82	5,47
1 FE 225-A10	0,247	0,082	0,644	0,000	5,632	0,330	8,74	4,04
1 FE 225-A15	0,234	0,419	1,313	0,000	10,558	1,608	8,04	3,84
1 FE 225-A20	0,212	0,728	2,637	0,001	19,737	3,469	7,49	4,76
1 FE 225-A25	0,194	0,433	4,280	0,001	30,615	2,287	7,15	5,29
1 FE 240-A05	0,246	0,004	0,247	0,000	2,421	0,025	9,82	6,05
1 FE 240-A10	0,247	0,075	0,644	0,000	5,635	0,305	8,75	4,05
1 FE 240-A15	0,235	0,389	1,308	0,000	10,553	1,510	8,07	3,88
1 FE 240-A20	0,212	0,717	2,628	0,001	19,728	3,434	7,51	4,79
1 FE 270-A05	0,246	0,003	0,246	0,000	2,419	0,015	9,82	5,42
1 FE 270-A10	0,247	0,040	0,644	0,000	5,628	0,159	8,74	3,98
1 FE 270-A15	0,235	0,227	1,289	0,000	10,497	0,845	8,14	3,72
1 FE 270-A20	0,213	0,400	2,549	0,001	19,483	1,856	7,64	4,64
1 FE 300-A05	0,246	0,001	0,246	0,000	2,415	0,004	9,82	4,63
1 FE 300-A10	0,246	0,008	0,642	0,000	5,613	0,028	8,74	3,45
1 FE 300-A15	0,235	0,049	1,280	0,000	10,463	0,174	8,18	3,55
1 FE 300-A20	0,213	0,086	2,508	0,001	19,365	0,395	7,72	4,58
1 FE 315-A05	0,245	0,000	0,246	0,000	2,414	0,001	9,82	5,18
1 FE 315-A10	0,246	-0,002	0,642	0,000	5,607	-0,009	8,74	5,12
1 FE 315-A15	0,235	-0,009	1,279	0,000	10,454	-0,031	8,17	3,45
1 FE 315-A20	0,212	0,007	2,505	0,001	19,354	0,035	7,73	5,07
1 FE 330-A05	0,245	0,000	0,246	0,000	2,414	0,001	9,82	12,17
1 FE 330-A10	0,246	-0,005	0,641	0,000	5,603	-0,020	8,74	3,86
1 FE 330-A15	0,235	-0,038	1,279	0,000	10,449	-0,132	8,17	3,46
1 FE 330-A20	0,212	-0,032	2,505	0,000	19,353	-0,144	7,73	4,47

3.4 Three rectangular FE

The last geometry was the three rectangular FE. The mesh independence study for this geometry was also done with a roll angle position of 270 degrees and an angle of attack of 15 degrees. With three FE, the roll angle position was defined with the centre FE. Table 14 presents the mesh characteristics and table 15 presents the aerodynamic coefficients for the mesh independence. Table 16 presents the differences of the aerodynamic coefficients of the mesh independence compared to the second one.

Table 14 : Mesh characteristics for mesh independence with three FE

Name	Mesh			
	Distribution	Nb cells	Y^+ (FE)	Y^+ (All)
3 FE V1	120	1448899	4,03	0,89
3 FE V2	160	3446672	4,22	0,89
3 FE V3	200	6654676	4,23	0,90

Table 15 : Mesh characteristics for mesh independence with three FE

Name	Forces			Moments			Pressure centre	
	C_A	C_Y	C_N	C_l	C_m	C_n	X_{cp}	Y_{cp}
3 FE V1	0,237	0,418	1,329	0,001	10,680	1,606	8,04	3,85
3 FE V2	0,238	0,422	1,312	0,001	10,571	1,618	8,06	3,83
3 FE V3	0,239	0,422	1,295	0,001	10,512	1,618	8,12	3,84

Table 16 : Difference between the mesh independence calculations with three FE

Difference	Forces		
	C_A	C_Y	C_N
3 FE V2 vs 3 FE V1	0,26 %	1,12 %	1,27 %
3 FE V2 vs 3 FE V3	0,37 %	0,15 %	1,31 %

The difference between the aerodynamic coefficients was smaller with this geometry. The side force difference between the first mesh and the second mesh was 1,1 %. The quality of the mesh around the FE was much better with the second mesh. For this reason, the second mesh was chosen for the calculations with three rectangular FE. The Y^+ value on the top of the FE was relatively large. The boundary layer refinement on the top of the FE was coarser to eliminate the mesh skewness around the FE.

A plot of the side force with the number of iterations was done in appendix B. The side force continually increased until the solution converged with the side force criterion. The calculation converged at around 7000 iterations. The continuity convergence criterion was around $1x10^{-5}$ when the solution was considered converged. Table 17 presents the mesh characteristics, the FE characteristics and the angle of attack. Table 18 presents the aerodynamic coefficients for the rectangular FE.

Table 17 : Three FE calculation characteristics

Name	Mesh		Flow Effectors	AOA
	Y^+ (FE)	Y^+ (All)	ϕ_{FE} (deg.)	(deg.)
3 FE 225-A05	3.96	0.83	225	5
3 FE 225-A10	4.08	0.87	225	10
3 FE 225-A15	3.89	0.89	225	15
3 FE 225-A20	3.29	0.90	225	20
3 FE 270-A05	4.05	0.83	270	5
3 FE 270-A10	4.34	0.87	270	10
3 FE 270-A15	4.22	0.89	270	15
3 FE 270-A20	4.05	0.90	270	20
3 FE 315-A05	4.02	0.83	315	5
3 FE 315-A10	4.13	0.88	315	10
3 FE 315-A15	4.25	0.90	315	15
3 FE 315-A20	4.31	0.91	315	20

Table 18: Aerodynamic coefficients for three FE calculation

Name	Forces			Moments			Pressure centre	
	C_A	C_Y	C_N	C_l	C_m	C_n	X_{cp}	Y_{cp}
3 FE 225-A05	0.248	0.008	0.246	0.000	2.416	0.043	9.82	5.40
3 FE 225-A10	0.249	0.112	0.646	0.000	5.641	0.457	8.73	4.06
3 FE 225-A15	0.237	0.456	1.318	0.000	10.587	1.812	8.03	3.98
3 FE 225-A20	0.214	0.733	2.637	0.002	19.777	3.635	7.50	4.96
3 FE 270-A05	0.248	0.006	0.246	0.000	2.419	0.033	9.82	5.60
3 FE 270-A10	0.250	0.079	0.644	0.000	5.636	0.320	8.75	4.05
3 FE 270-A15	0.238	0.422	1.312	0.001	10.571	1.618	8.06	3.83
3 FE 270-A20	0.215	0.666	2.613	0.002	19.697	3.206	7.54	4.82
3 FE 315-A05	0.248	0.002	0.246	0.000	2.417	0.010	9.82	6.27
3 FE 315-A10	0.249	0.003	0.640	0.000	5.600	0.015	8.75	5.68
3 FE 315-A15	0.237	-0.008	1.273	0.001	10.420	-0.003	8.18	0.42
3 FE 315-A20	0.215	0.032	2.503	0.001	19.348	0.165	7.73	5.15

3.5 Pressure profile

The second interesting parameter to compare the numerical solution with the wind tunnel was the pressure profile around the missile. In the wind tunnel, pressure taps will be placed at six positions from the nose. These positions were: 33,32 mm (1,3118 inch), 63,83 mm (2,5130 inch), 86,34 (3,3990 inch), 116,23 mm (4,5759 inch), 153,73 mm (6,0524 inch) and 198,74 mm (7,8242 inch). Figure 11 show the pressure taps positions. With the Fluent™ code, the wall pressures can be determined in two ways: pressure contours over all the body and pressure profiles at the six defined positions. To obtain pressure profiles at the defined positions, a plane should be created at the position. This plane includes all the mesh nodes from the missile wall up to the far field. An "iso-clip" surface should be created from the previous plane to limit the node selection in a near wall ring of about 0,1 mm high. A bigger ring was used to be sure have pressure data all around the missile body.

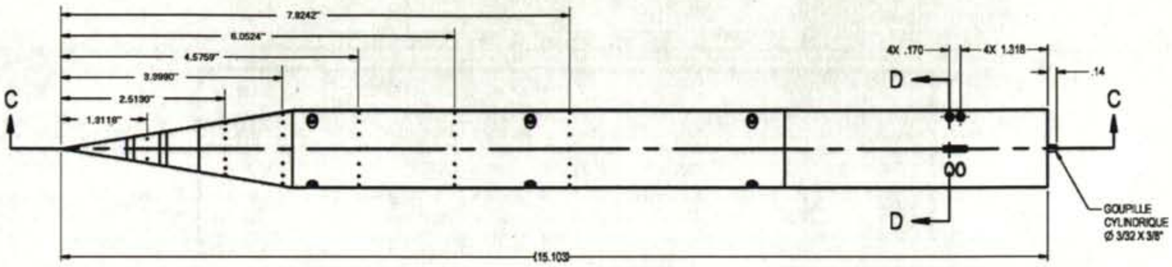

Figure 11 : Pressure taps position for pressure profile

The plot of the iso-clip surface included a number of pressure values between 800 and 1200 because the ring was too high. The near wall mesh included 160 node points with every FE configuration. The pressure values from an iso-clip were distributed in small groups around the near wall mesh node. Since the iso-clip surface included many points with the same value, it was necessary to group the value to the number of the near wall node point. To be able to do this, a small Matlab™ program was built. This program included three steps. First step was to eliminate incoherent values. At approximately every pressure profile, there were about one and three incoherent values. These incoherent values were simply neglected. Figure 12a shows the result of the fist step. The second step was to group the values around each near wall points. The points were grouped together with the roll angle position coordinate. If the point was nearest than a certain criterion, the point was grouped with the actual grouping points. The value of the grouping points was calculated by the mean value of all the points grouped together. If the point was further away than the criterion, the point was considered to be part of another group of points. This criterion was set to a quarter of the space between two near wall mesh nodes. Figure 12b presents the effect of this step. Third step was to apply the coordinate system that was adopted for this project. Fluent™ presents the values with an angular coordinate from $-\pi$ radian to π radian and the origin is align with the positive y axis of the north, east, down reference coordinate system. In Fluent™, a positive angle is counter-clockwise. For this work, the angular origin was aligned with the positive z axis, which is directly down and a positive angle is clockwise. Finally, in this work, the roll angle positions were presented with values between 0 and 360 degrees. Pressure profiles for every calculation were done on a plot. The pressure is presented as a pressure coefficient. Those plots are presented in appendix C.

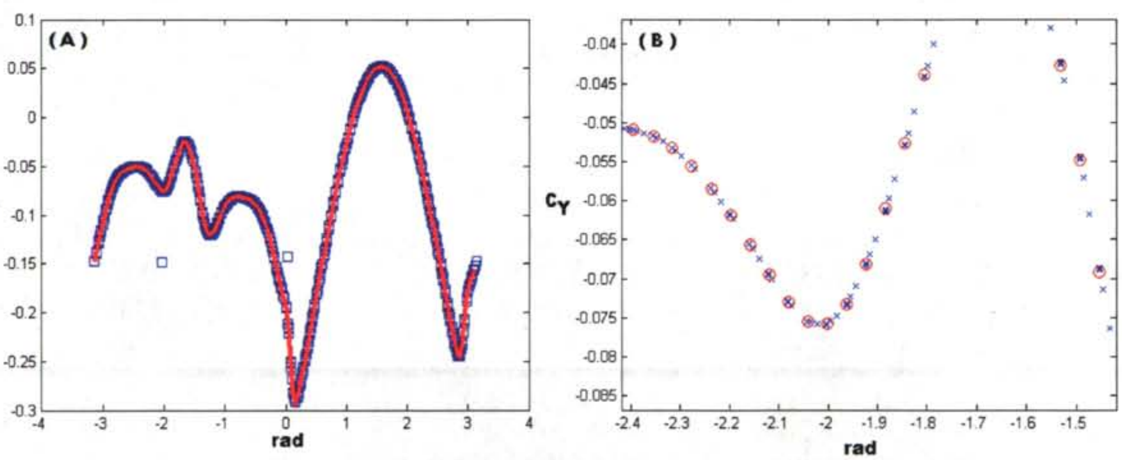

Figure 12 : Effect of Matlab™ program on pressure profile data for the first step (A) and the second step (B)

4.0 DISCUSSION

The comparison between the numerical results and the wind tunnel measurements had a better correlation for this study than for the other. The side force calculated appeared to be interesting for some roll angle positions of the FE, but the side force could also be near zero in other roll angle position of the FE. Calculations showed that the FE generated a more important side force if it was placed on the leeward side. The centre of pressure for the side force Y_{cp} was mostly between 3,5 and 6, which meant that the side force was acting mainly at the centre of the cylinder body. These results suggested that the side force was created by an asymmetry of the main vortices. Two important results in this work were the aerodynamic coefficients and the wall pressures profiles. Also, the knife-edge FE was analysed to find a simpler geometry to reduce the meshing time in a design operation. A comparison between the rectangular FE and the knife-edge FE was done. Finally, effects of the FE were explained.

4.1 Aerodynamic coefficients

In the performance of a FE, the side force is the more important factor. Calculation results showed two important factors that influenced the performance of the FE, which are roll angle position and angle of attack. Figure 13 presents a graphic of the side force aerodynamic coefficient with AOA for the knife-edge FE with the results for calculations without FE (WO FE).

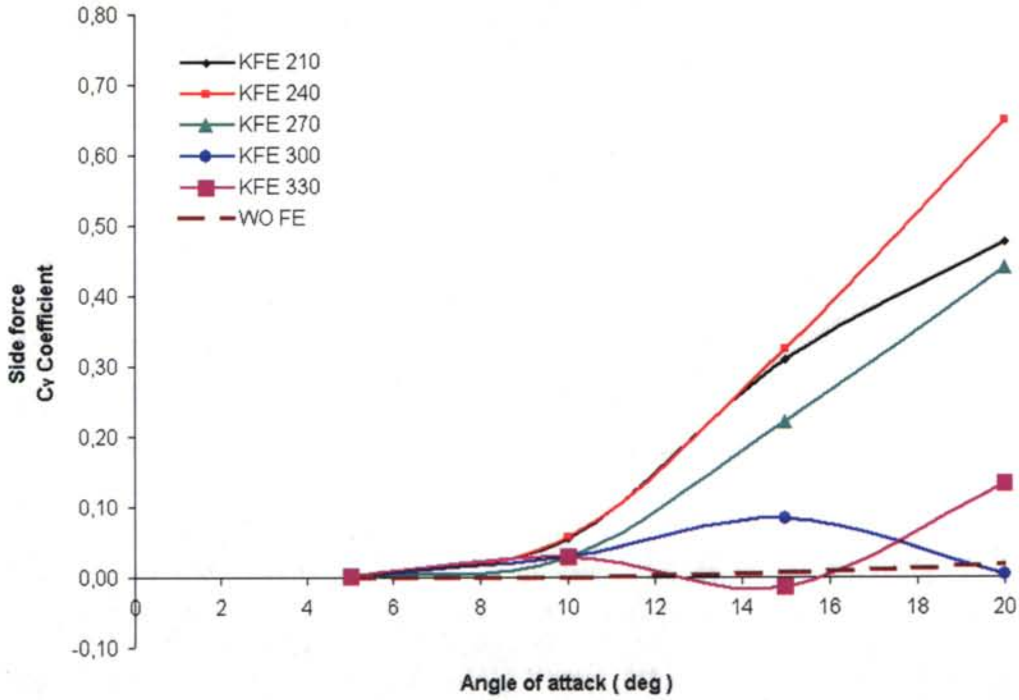

Figure 13 : Side force performance of the knife-edge FE with AOA

The first factor is the roll angular position of the FE. DeChamplain et al. (2002) calculated no side force when the FE were placed on the top of the missile or roll angle position of 180 degrees with the present coordinate system. Rainville and Gosselin (2004) found an interesting side force when the FE were placed in a perpendicular plane with the AOA, or roll angle position of 270 degrees. In this

work, many roll angle positions were studied. As it shows on figure 13 for the knife-edge FE, the maximum side force was obtained with a roll angle position of 240 degrees. In the case of one rectangular FE, the maximum side force appeared with a roll angle position between 225 degrees and 240 degrees. When the FE was on the windward side, with a roll angle between 300 degrees and 330 degrees, the side force was near zero. With 330 degrees of roll angle position, the side force was switching side with AOA.

The second factor was the AOA. Figure 14 presents the performance for the rectangular FE. This figure includes results from the wind tunnel for the rectangular FE at roll angle positions of 225 degrees (W-T FE 225) and 270 degrees (W-T FE 270). Results showed that at less than 10 degrees of AOA, the performance of the FE were very small. Numerical calculations suggested that the FE obtained a maximum performance around 20 degrees of AOA. Wind tunnel measurements showed a maximum side force between 15 degrees and 17 degrees AOA.

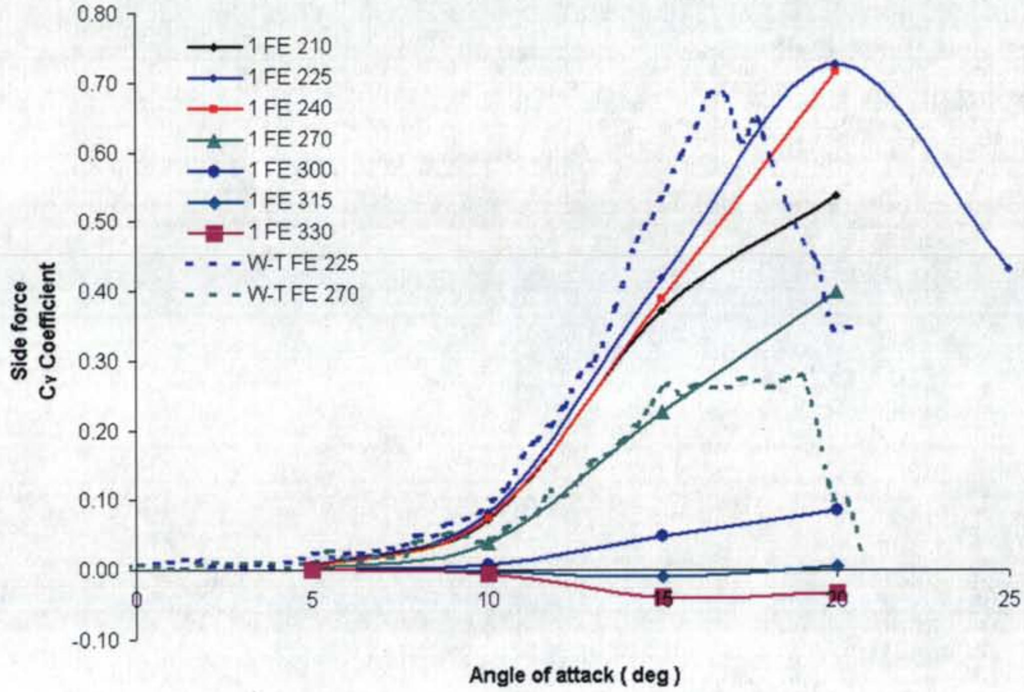

Figure 14 : Side force performance of rectangular FE with AOA

Over the maximum point, the side force performance was reduced as was observed with three time baseline FE in previous work [Rainville and Gosselin (2004)]. Side force reduction can be explained by two phenomena's. In the case of the three time baseline FE, the side force reduction can be mainly explained by a separation of the boundary layer over the FE wall. With the separation of the boundary layer, the FE generated a smaller wake that had less effects on the flow field structure.

A second phenomenon, that is more realistic with the baseline FE, is the transition of the main vortices structures. With a very small angle of attack, no main vortices were generated. With a small angle of attack, a steady symmetric main vortices were generated and they mostly followed the body. In the case of a conical nose body, like the one used in this work, Ericsson and Reding (1991) predicted that a vortex appeared when the AOA became bigger than the cone half-angle. With a

higher angle of attack, the main vortices became asymmetric and they separated off the body. Chapman (2000) reported a rapid drop of the maximum side generated by asymmetric vortices in a supersonic flow. Transition between symmetric vortices and asymmetric vortices happened when the AOA was around the cone angle of the nose [Ericsson and Reding (1991)]. When the AOA continued to increase, the main vortices became unsteady and they slowly took the shape of a classical Von-Karman vortex street.

In the present work, the missile had a conical nose with an angle of 18,9 degrees. Vortices appeared at around 10 degrees, which explained very small side forces under 10 degrees AOA. Vortices were to become asymmetric, when the AOA was 20 degrees. An additional calculation was done with an AOA of 25 degrees for a rectangular FE placed at a roll angle position of 225 degrees, to know if the calculation code Fluent™ was able to predict vortex transition. Figure 14 shows that the side force with an AOA of 25 degrees has reduced with a factor of two from the case with an AOA of 20 degrees. This result showed that the transition of the vortices happened when the AOA became bigger than the cone angle. The difference between the transition AOA in the calculation and in the wind tunnel may be explained by small defaults on the wind tunnel model and by vibration of the system.

Calculation without the FE was also done with an AOA of 25 degrees and 30 degrees to study the transition of the vortices. Figure 15 presents the side force evolution with AOA. Between 10 degrees and 20 degrees AOA, the side force slowly increased, and became negative over 20 degrees of AOA. Those transitions were in agreement with the transition point of the vortices.

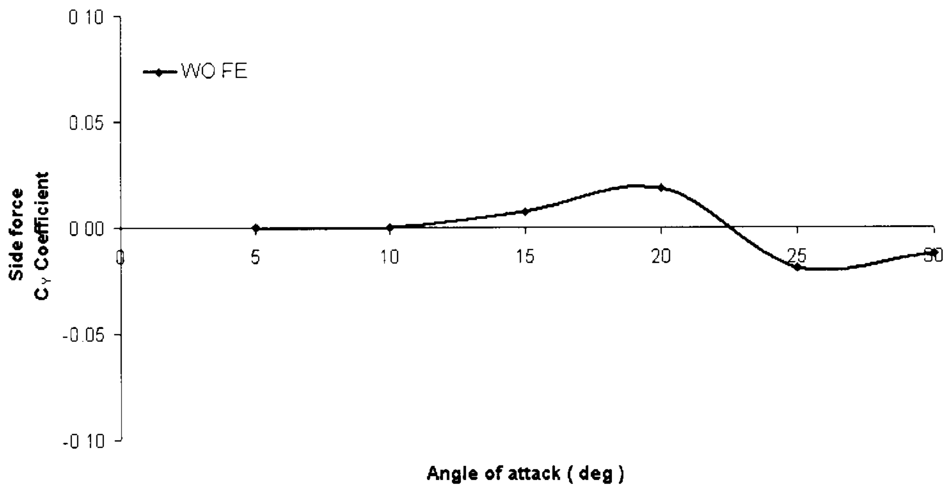

Figure 15 : Side force performance without FE with AOA

The number of FE did not represent an important factor. It was observed that three FE placed at a roll angle position of 270 degrees generated a more important force than one FE at the same place. But in this configuration, one FE was located at 240 degrees, the other one at 270 degrees and the last one at 300 degrees. Table 19 presents a comparison of results between three FE and one FE at the three positions of the three FE. Table 19 includes the configuration of the three FE calculations, and the side force aerodynamic coefficient. The middle part of the table presents the side force aerodynamic coefficient for one FE placed at a roll angle position of 240 degrees (1 FE 240), 270

degrees (1 FE 270) and 300 degrees (1 FE 300). Finally, a side force comparison between three FE and one FE with a roll angle position of 240 degrees. Except for an AOA of 5 degrees, the difference between three FE and one FE at 240 is less than 10 %. Figure 16 presents the side force performance for three FE. This figure demonstrates the performance similarity between three FE geometry and the most performing FE alone for all the roll angle positions.

Table 19 : Difference between three FE and one FE

Name	AOA (deg.)	Force C_Y	Force C_Y			Difference
			1 FE 240	1 FE 270	1 FE 300	3 FE vs 1FE 240
3 FE 270-A05	5	0.0059	0.0042	0.0027	0.0008	29.3 %
3 FE 270-A10	10	0.0789	0.0752	0.0400	0.0081	4.6 %
3 FE 270-A15	15	0.4223	0.3893	0.2273	0.0491	7.8 %
3 FE 270-A20	20	0.6657	0.7165	0.4002	0.0862	7.6 %

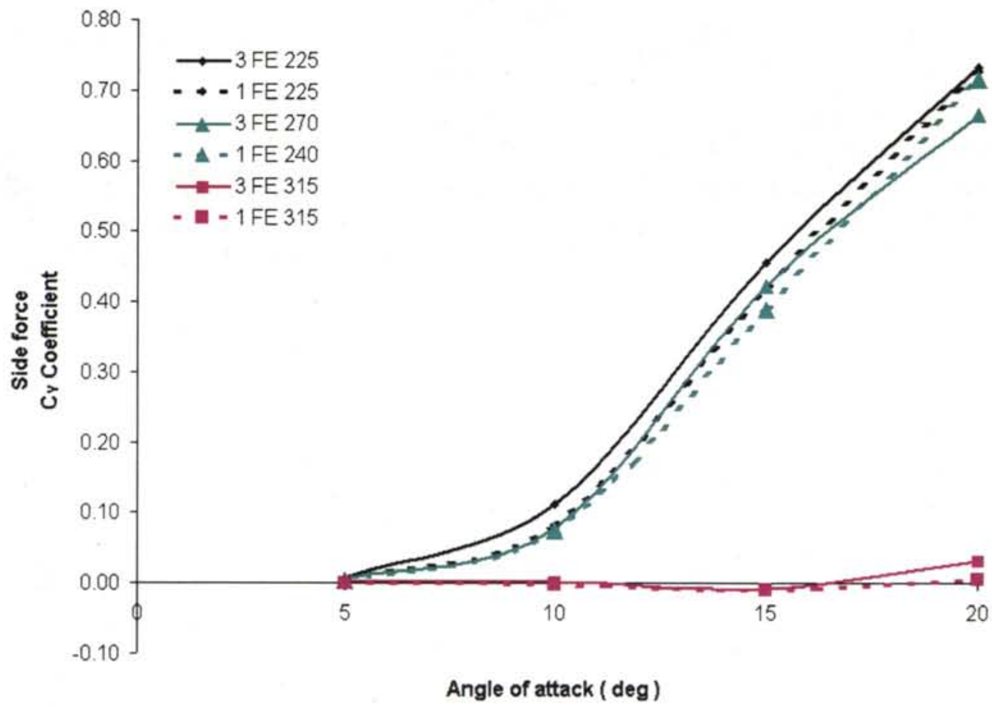

Figure 16 : Side force performance of three rectangular FE with AOA

4.2 Pressure profile

Discussion about aerodynamic coefficient showed that the best roll angle position was around 225 degrees to generate a side force. Wall pressure profile can give an idea of the effect of the FE and how the side force is generated. Figure 17 presents an example of the wall pressure profile plot. This example is from a calculation with a rectangular FE placed at a roll angle position of 270 degrees and at an AOA of 20 degrees. Wall pressure profiles for all configurations are presented in appendix C.

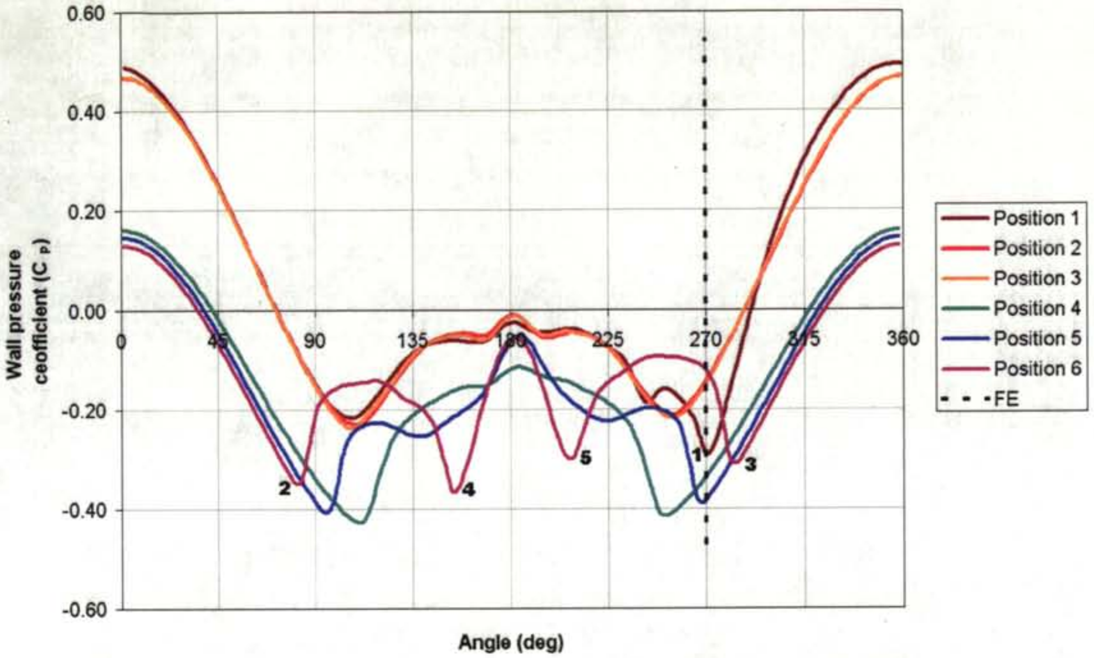

Figure 17 : Wall pressure profiles calculation with a rectangular FE placed at a roll angle position of 270 degrees and an AOA of 20 degrees

The figure included three interesting elements. The first element showed the direct effect of the FE on the near downstream flow field # 1. Positions 2 and 3 did not seem to be affected by the FE. On the cylinder body, two other elements appeared. The first is the boundary layer separation on each side of the body, identified with # 2 and # 3. The second is on the top the body and it could be observed only at the pressure tap position 6 as # 4 and # 5. Figure 18 presents the pressure contours on the wall body and on a plane at the pressure tap position 6. This figure shows a small formation of the main vortices over the body. The base of the main vortices is connected to the low-pressure zone # 4 and # 5 of figure 17. These low-pressure zones appeared to be generated by the main vortices. At pressure position 5 this low-pressure zone appeared to be small and wide. Figure 19 presents the evolution of the main vortices, with a vorticity contour.

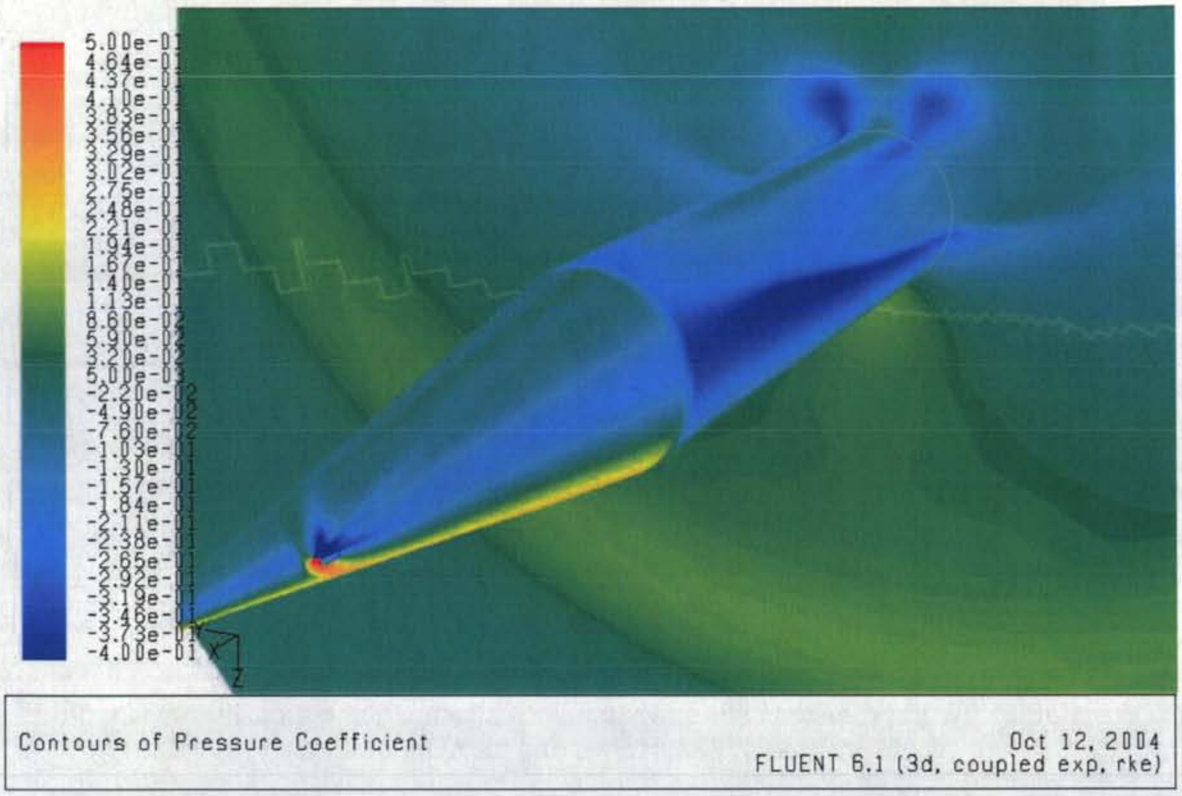

Figure 18 : Pressure contour on the wall of the body and on a plane at pressure tap position 6

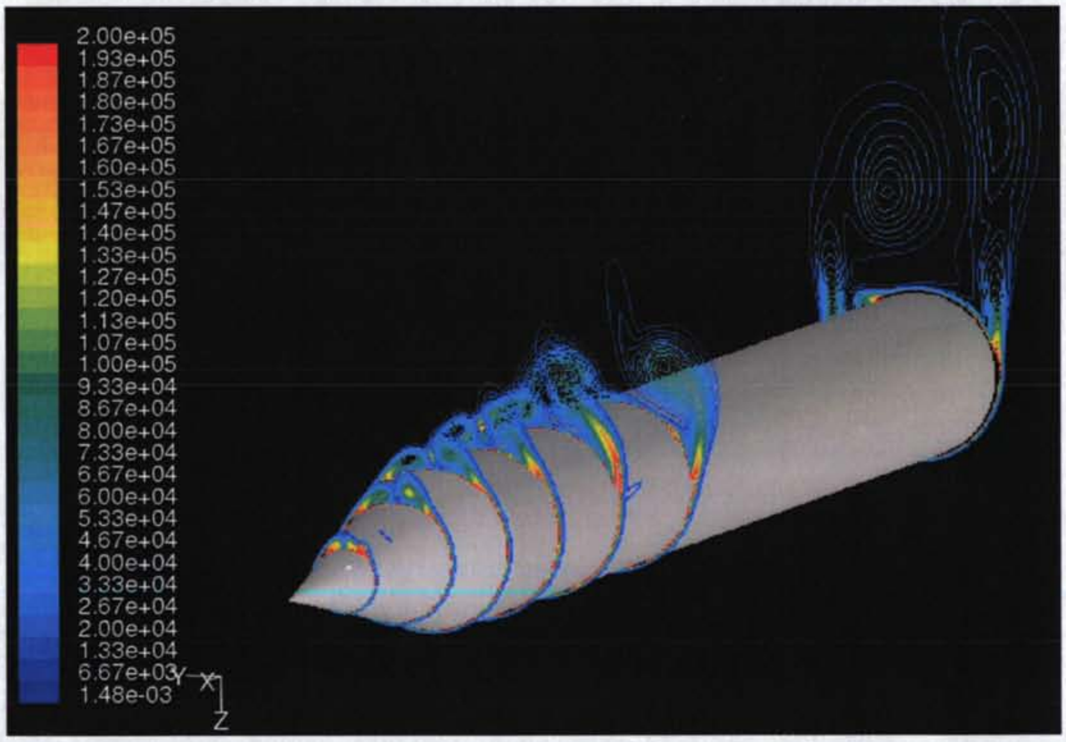

Figure 19 : Main vortices propagation over the body

4.3 Comparison rectangular FE and knife edge FE

A new geometry was defined with the aim to simplify mesh generation. As discussed in section 2.1 about the geometry, only the second knife-edge FE was calculated. The knife-edge geometry should have approximately the same performance to become design geometry. The performance was evaluated by two criteria. First, it should produce the same pressure profile curve over the body. Second, it should produce the same side force.

Wall pressure profiles presented a good correlation between the knife-edge FE and the rectangular FE. The difference between the knife-edge FE and the rectangular FE happened only at the first pressure tap position, where it was very near of the FE. Pressure perturbations were stiffer around the rectangular FE. At other pressure tap positions, the curves for the two geometries were exactly one over the other. Those graphics suggested that the difference of performance between the knife-edge FE and the rectangular FE should be small. Wall pressure profiles comparison plot were done for the FE placed at a roll angle position of 270 degrees at an AOA of 15 degrees for every pressure tap positions in appendix D. The plot for the first pressure tap positions were also included for the FE placed at a roll angle position of 210 degrees and 330 degrees with an AOA of 15 degrees.

Aerodynamic coefficients did not presented the same correlation for the side force. Table 20 presents a comparison of the aerodynamic coefficients between the knife-edge FE and the rectangular FE. Table 20 compares the axial coefficient (C_A), the side force coefficient (C_Y), the normal coefficient (C_N) and the Y pressure center (Y_{CP}). For each parameter, the coefficient values for the knife-edge FE (KFE) and for the rectangular FE (1 FE) were presented. The differences between the coefficients for the two geometries are identified in the column Diff. For differences bigger than 30 %, the values were written in italic. The values of Y_{CP} for the knife-edge FE placed at a roll angle position of 270 degrees with an AOA of 5 degrees and for the FE placed at a roll angle position of 330 degrees with an AOA of 5 degrees were also in italic because they were incoherent. The first one was incoherent because the pressure center was before the nose of the body. The second one was just on the back of the missile, but it was too far away compared to the other results.

For the axial coefficient, the difference between the geometry was small with a value under 1 %. The difference was also small for the normal coefficient. Except when the FE was placed at a roll angle position of 270 degrees with an angle of attack of 5 degrees, the difference stayed under 1 %. The incoherent values of Y_{CP} for the knife-edge FE at a roll angle position of 270 degrees with an angle of attack of 5 degrees might explain the important difference. The difference for the side force was around 30 % when the FE were placed over the body (210°, 240° and 270°). The difference was extreme when the FE was under the geometry (300° and 330°), but the FE did not generated a side force at that position. The correlation is better with an AOA of 15 degrees or 20 degrees. This comparison between the knife-edge FE and the rectangular FE showed that the two geometries did not had the same effect on the flow and did not had the same performance.

Table 20 : Comparison of aerodynamic coefficients between the knife-edge FE and the rectangular FE

Configuration		C_A			C_Y			C_N			Y_{cp}		
ϕ_{FE}	AOA	KFE	1 FE	Diff.	KFE	1 FE	Diff.	KFE	1 FE	Diff.	KFE	1 FE	Diff.
210°	5°	0.245	0.245	0.12%	0.002	0.005	*54%*	0.247	0.246	0.30%	7.05	5.49	28%
	10°	0.246	0.246	0.20%	0.055	0.073	24%	0.644	0.643	0.21%	3.94	3.98	1.1%
	15°	0.234	0.234	0.21%	0.310	0.373	17%	1.301	1.302	-0.06%	3.58	3.70	3.4%
	20°	0.211	0.211	0.07%	0.477	0.538	11%	2.571	2.579	-0.30%	4.42	4.61	4.1%
240°	5°	0.245	0.246	0.20%	0.002	0.004	*46%*	0.247	0.246	0.06%	6.96	6.05	15%
	10°	0.246	0.247	0.28%	0.057	0.075	24%	0.644	0.644	-0.10%	4.06	4.05	0.2%
	15°	0.234	0.235	0.28%	0.324	0.389	17%	1.302	1.308	-0.46%	3.82	3.88	1.4%
	20°	0.211	0.212	0.27%	0.648	0.716	10%	2.606	2.628	-0.84%	4.66	4.79	2.7%
270°	5°	0.247	0.246	0.64%	0.000	0.003	*114%*	0.252	0.246	2.25%	*-8.05*	5.42	*248%*
	10°	0.247	0.247	0.18%	0.027	0.040	*32%*	0.650	0.644	1.06%	4.49	3.98	13%
	15°	0.234	0.235	0.28%	0.220	0.227	3%	1.289	1.289	-0.03%	3.69	3.72	0.8%
	20°	0.212	0.213	0.22%	0.439	0.400	10%	2.558	2.549	0.37%	4.61	4.64	0.6%
300°	5°	0.245	0.245	0.07%	0.002	0.001	*79%*	0.247	0.246	0.42%	3.80	4.63	18%
	10°	0.246	0.246	0.16%	0.030	0.008	*274%*	0.643	0.642	0.21%	3.07	3.45	11%
	15°	0.234	0.235	0.21%	0.083	0.049	*69%*	1.281	1.280	0.08%	3.39	3.55	4.6%
	20°	0.212	0.213	0.44%	0.003	0.086	*96%*	2.505	2.508	-0.12%	3.99	4.58	13%
330°	5°	0.245	0.245	0.10%	0.001	0.000	*2292%*	0.246	0.246	0.16%	2.86	*12.17*	*77%*
	10°	0.246	0.246	0.08%	0.029	-0.005	*661%*	0.645	0.641	0.56%	3.38	3.86	12%
	15°	0.234	0.234	0.16%	-0.012	-0.038	*68%*	1.279	1.279	0.00%	3.67	3.46	6.2%
	20°	0.212	0.212	0.05%	0.133	-0.032	*512%*	2.511	2.505	0.23%	4.54	4.47	1.6%

4.4 Effect of FE

Results of the present work showed an interesting side force generated by the FE. Plot of the dynamic pressure at the base of the missile showed asymmetric main vortices when a side force was generated. Asymmetries also affected the wall pressure profiles that generated a side force on missile. Now that it is discovered that the FE can generate a side force with a roll angle position over the body, two interesting question remains. How can a FE modify the flow field around the body to generate a side force? What happens when a FE is under the body?

To answer the first question, the case of one FE placed at a roll angle position of 225 degrees will suggest one option. Figure 20 presents the wall pressure profile for the calculation with one FE placed at a roll angle position of 225 degrees and at a AOA of 20 degrees. The FE generates a wake that causes a low-pressure zone # 1 at pressure tap position 1 near the top of the missile. This low-pressure zone of # 1 attracts the high-pressure zone on the top of the missile # 2. At pressure tap position 2 and 3, the spike of pressure # 2 is slightly moved in the FE side direction. Between pressure tap positions 3 and 4, there is a transition between the conical section and the cylinder section of the body. At pressure tap position 4, the pressure profile has important asymmetries on the side of the FE that is identify with # 3. The shifting of the flow structure at pressure taps position 5 and 6 caused an earlier separation of the boundary layer. This boundary layer separation on body # 4 generated the side force.

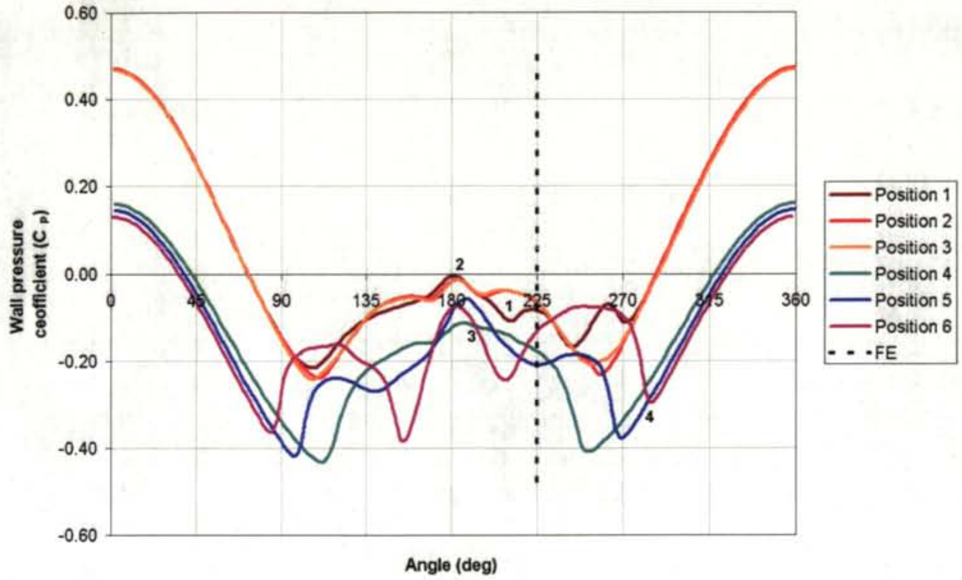

Figure 20 : Wall pressure profile for calculation with one FE at a roll angle position of 225 degrees and an AOA of 20 degrees

Figure 21 presents the wall pressure profile for the calculation with one FE placed at a roll angle position of 315 degrees, at an AOA of 20 degrees. It will be used to answer the second question. This calculation showed that the effect of the FE stayed around the FE geometry. Since the surface under the body receives an unperturbed flow, perturbation of the FE did not really propagated on the body. For this reason, the pressure profile on the pressure tap position 2 and 3 stayed unperturbed. The effect of the FE appeared on pressure tap position 1 at # 1. This pressure profile showed that a kind of air bubble appeared under the body. At # 2, pressure was less important with the bubble, which caused a lift reduction.

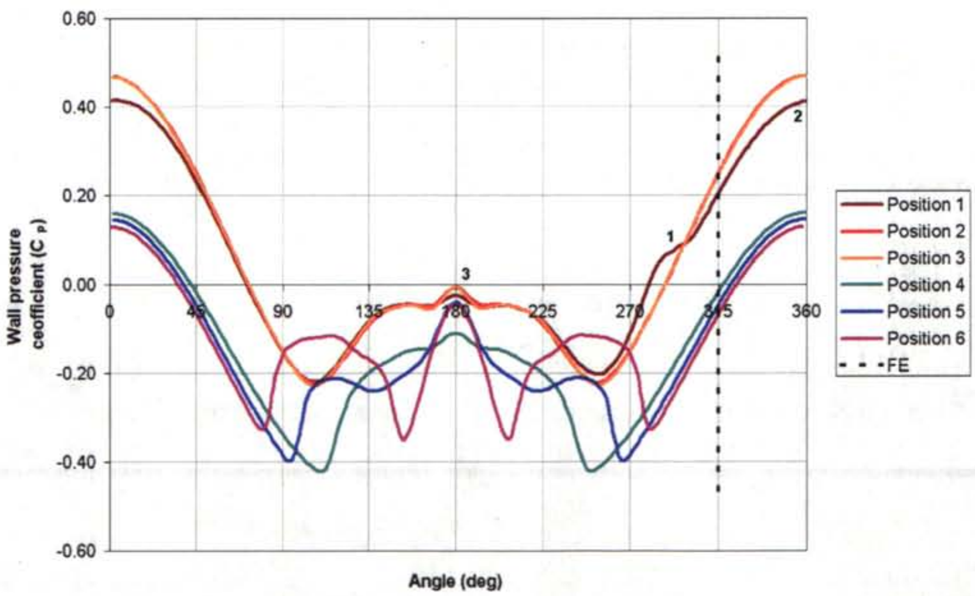

Figure 21 : Wall pressure profile for calculation with one FE at a roll angle position of 315 degrees and an AOA of 20 degrees

5.0 CONCLUSION

This study on FE aimed at defining the influence of the position of the FE on a missile body with the AOA. The calculations were done with three FE configurations: one knife-edge FE, one rectangular FE and three rectangular FE. For each configuration, some roll angle positions were analysed to define the effect of the position of the FE on the performance. For each calculation, wall pressure profiles were drawn to compare with the DRDC - Valcartier wind tunnel measurements. Model set-up for this work was defined with the experience acquired during previous work. Validation was done with some initial forces measurement done in the wind tunnel. A FE placed at a roll angle of 270 degrees was included on the wall body during the validation. During the validation step, the mesh was modified to have a more precise zone where the main vortices could propagate between the boundary layer zone near the wall and the far field zone. Finally, for each configuration, a mesh independence study was done.

Calculations showed that a FE was more efficient when it was placed at a roll angle position between 225 degrees and 240 degrees. A side force was also generated when the FE was placed at a roll angle position of 270 degrees. The side force was generated by a small rotation of the flow structure initiated by the wake of the FE. When the FE was under the body, with a roll angle position over 300 degrees, no side force was generated. In this case, the FE generated a small zone of low pressure, at the first pressure tap position, that reduced slightly the lift.

The Knife-edge FE should be a design geometry easier to mesh. Calculations with this geometry showed a small difference with the rectangular FE for the axial and the normal aerodynamic coefficient. But the knife-edge FE had a side force performance that was around 30 % with the rectangular FE. For many studies, this difference was too important to use a knife-edge FE instead of a rectangular FE. Results for the calculation with three FE showed a small effect of the number of FE. The side force generated by three FE were almost the same than the side force generated by the most efficient FE alone. This result showed that the position of the FE had a more important effect than number of FE.

Finally, comparison of the numerical results for one rectangular FE to the wind tunnel measurements showed that the side force generation was well connected to the vortices structures. The side force aerodynamic coefficients correlated well, between the calculation and the measurements up to an AOA of 15 degrees. But the measurements showed a side force maximum at around 17 degrees AOA. The side force reduction represented the transition of the main vortices from symmetric to asymmetric. Theory considers that transition of vortices happened when the AOA was equal to the cone angle of 19 degrees. To know if the vortices transition could be captured with Fluent™ code, additional calculations with an AOA bigger than 20 degrees were done. Results showed that the transition could be captured. The difference of AOA in the transition between numerical solution and measurement could be explained by the model imperfections. Maybe the use of a roughness model on the missile nose wall could reduce the difference.

6.0 REFERENCE

Chapman, G.T., *Fluids Structures and Instabilities for Application of MEMS to Supersonic Flow Control*, Virginia USA : Report submitted to DynCorp, September 2000.

DeChamplain, A., Gosselin, P., Hamel, N., Rainville, P.-A., *Feasbility of Active Flow Control with MEMS for Missile or Rocket Guidance*, Quebec : Numerica Technologies Inc, July 2001. UNCLASSIFIED

DeChamplain, A., Gosselin, P., Harrisson, V., Rainville, P.-A., *Feasbility of Missile Guidance using MEMS based Active Flow Control – Part 2*, Quebec : Numerica Technologies Inc, March 2002. UNCLASSIFIED

Ericsson, J.E., Reding, J.P., Chapter 10 *Asymmetric Flow Separation and Vortex Shedding on Bodies of Revolution*, California : (Hemsch, M.J., Seebass, A.R.), Tactical Missile Aerodynamics: General Topics, Volume 141, Progress in Astronautics and Aeronautics, AIAA, p. 731. 1991.

Garon, L.K.D., Abate, G.L., Hathaway, W., *Free-Flight Testing of Generic Missile with MEMs Protuberances*, Nevada USA : AIAA 2003-1242, January 2003.

Ho, C.-M., Tai, Y.-C., *Review : MEMS and its Applications for Flow Control*, California USA : Journal of Fluids Engineering, V118 No 3, September 1996.

Lesage, F., Boulianne, M.-A., *Navier-Stokes Prediction of Missile Flowfields with Wings and Body Vortices*, DREV-TM-9835, Valcartier : DREV, February 1999.

Patel, M.P., Prince, T.S., Carver, R., DiCosso, J.M., Lisy, F.J., Ng, T.T., *Deployable Flow Effectors for Phantom Yaw Control of Missiles at High Alpha,* Missouri : AIAA 2002-2827, June 2002.

Rainville, P.-A., Gosselin, P., *Performance for Guidance of a Generic Missile using Flow Effectors on the Nose*, Quebec : Numerica Technologies Inc, March 2004. UNCLASSIFIED

Tsao, T., Jiang, F., Miller, R.A., Tai, Y.C., Gupta, B., Goodman, R., Tung, S., Ho, C.M., An Integrated MEMS System for Turbulent Boundary Layer Control, Technical Digest, Chicago USA : International Conference on Solid-State Sensors and Actuators, Vol. 1, p. 315-318, June 1997.

Wong, F.C., *Missile Flight Control using Micro-Actuated Flow Effectors, Technical Note DRDC Valcartier TN 2004-066*, Valcartier : DRDC-Valcartier, May 2004.

- Corriveau, D., *Missile Forebody Flow Perturbation for Enhanced Control and Maneuvrability*
- Hamel, N., *Effect of the Turbulence Models of the Side Force Generated by Cylindrical Protrusions*
- Rainville, P.-A., Gosselin, P., *Performance for Guidance of a Generic Missile using Flow Effectors on the Nose*

APPENDIX A

MESH FIGURES

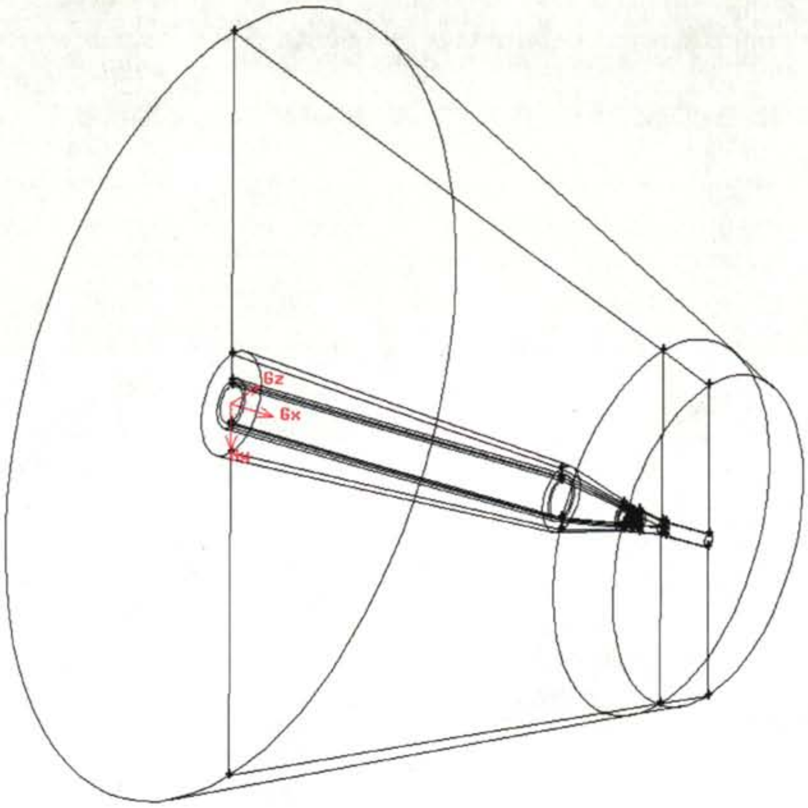

Figure A1 : Mesh structure of the complete calculation domain

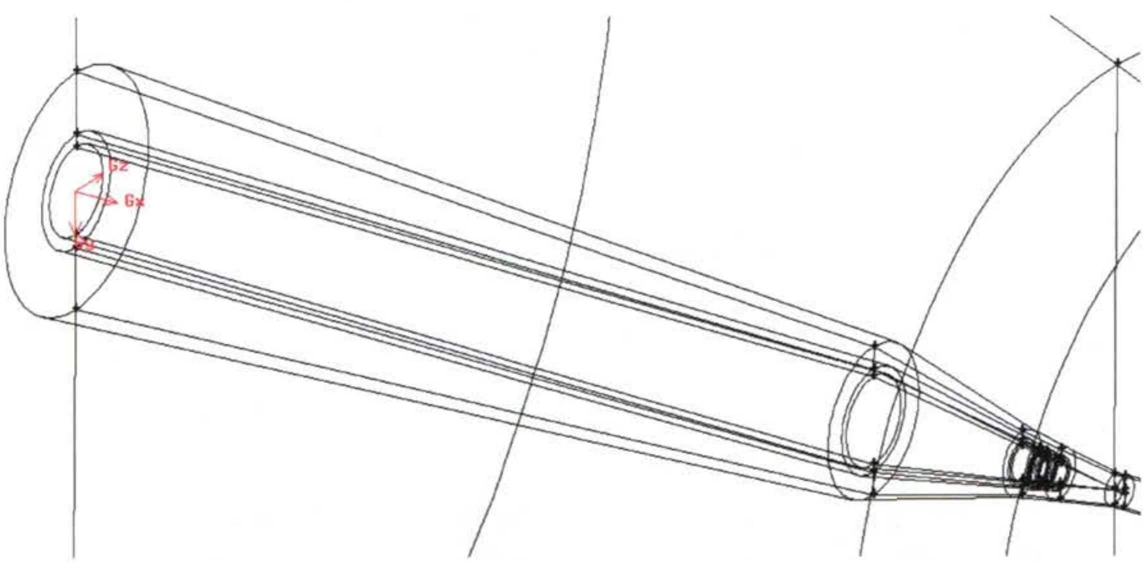

Figure A2 : Mesh structure for the boundary layer and the propagation zone of the vortex

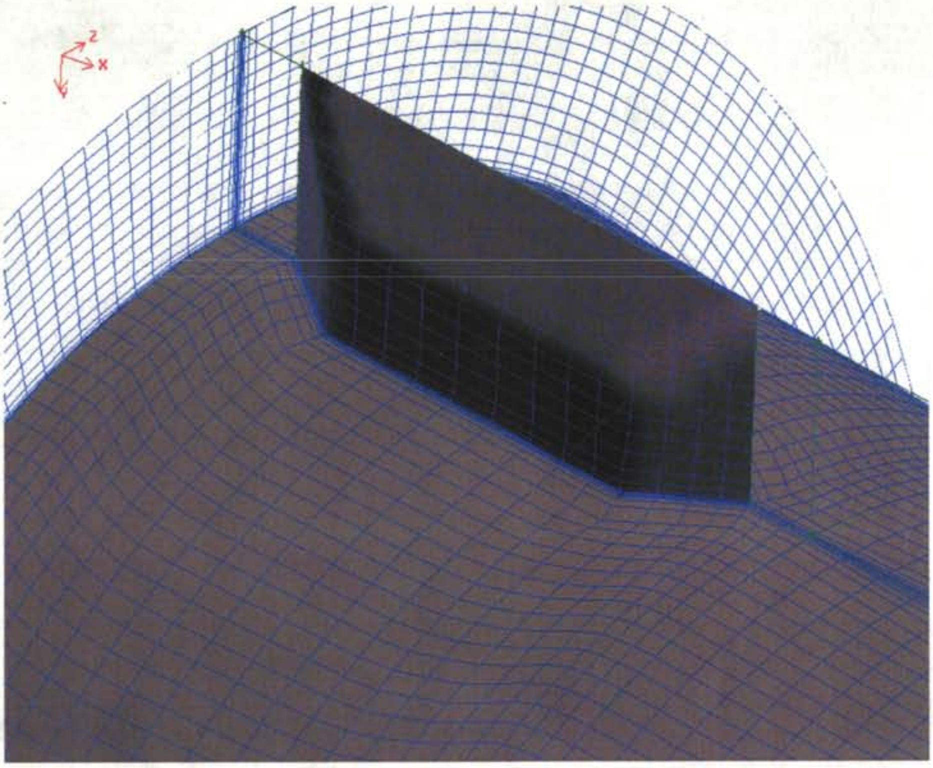

Figure A3 : Surface mesh around the knife-edge FE

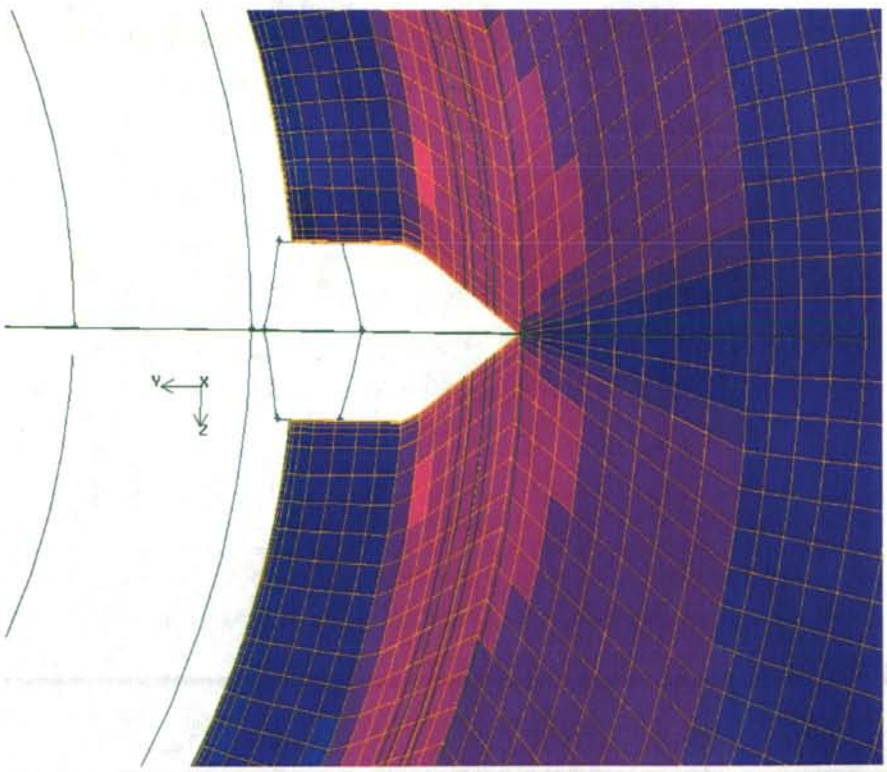

Figure A4 : Volume mesh around the knife-edge FE

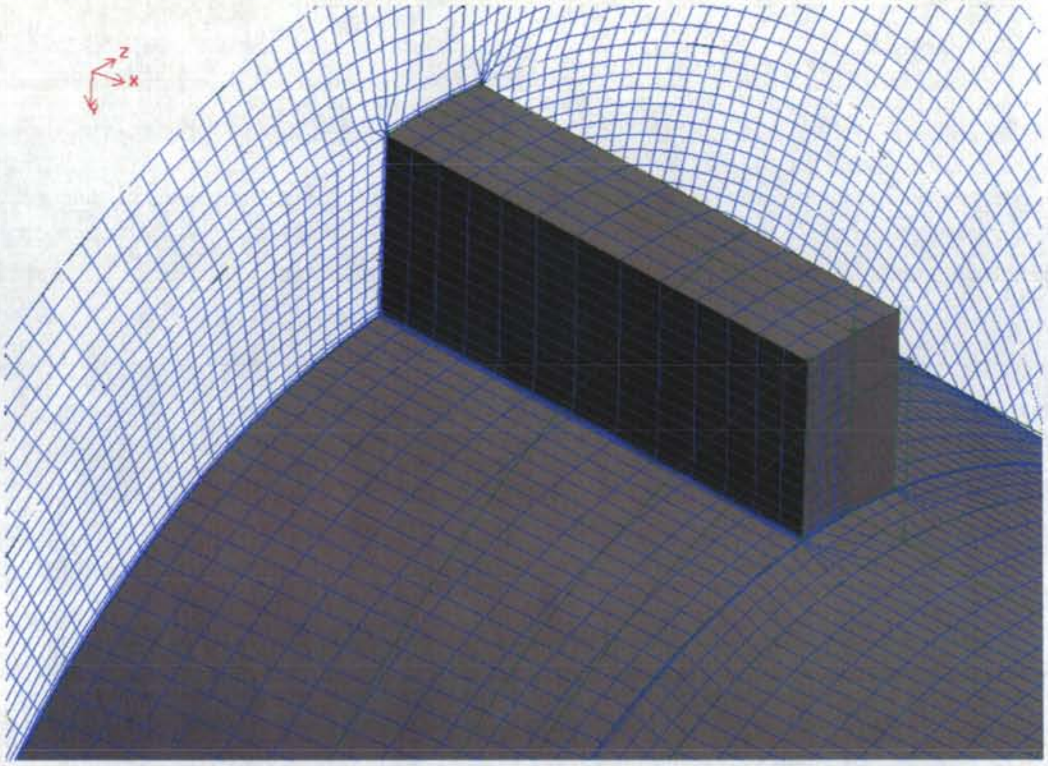

Figure A5 : Surface mesh around the rectangular FE

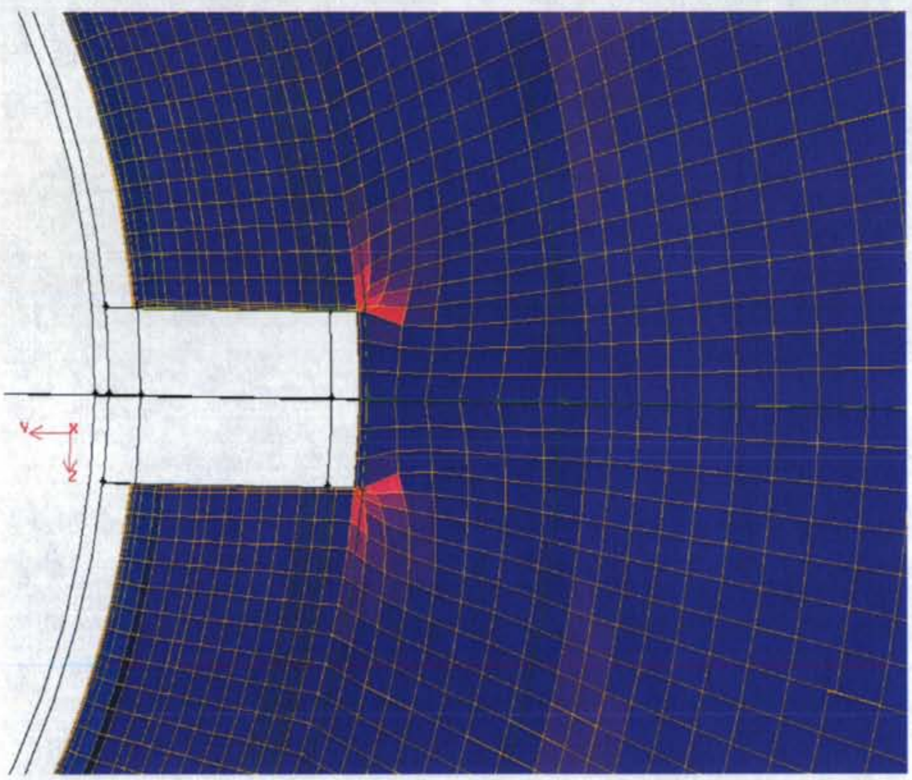

Figure A6 : Volume mesh around the rectangular FE

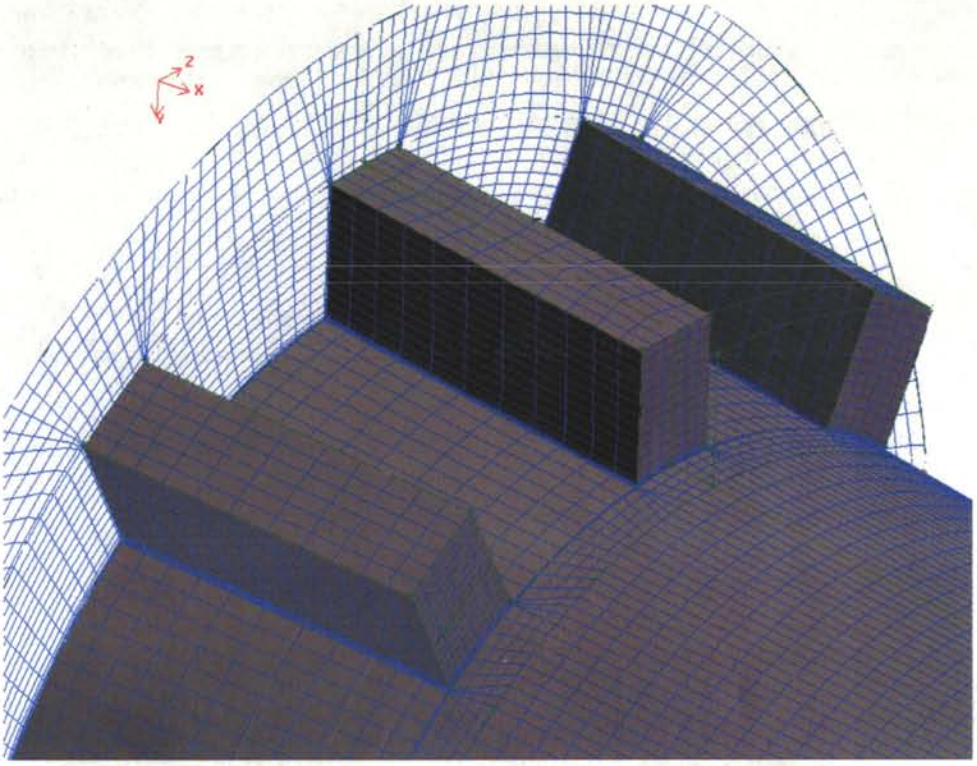

Figure A7 : Surface mesh around three rectangular FE

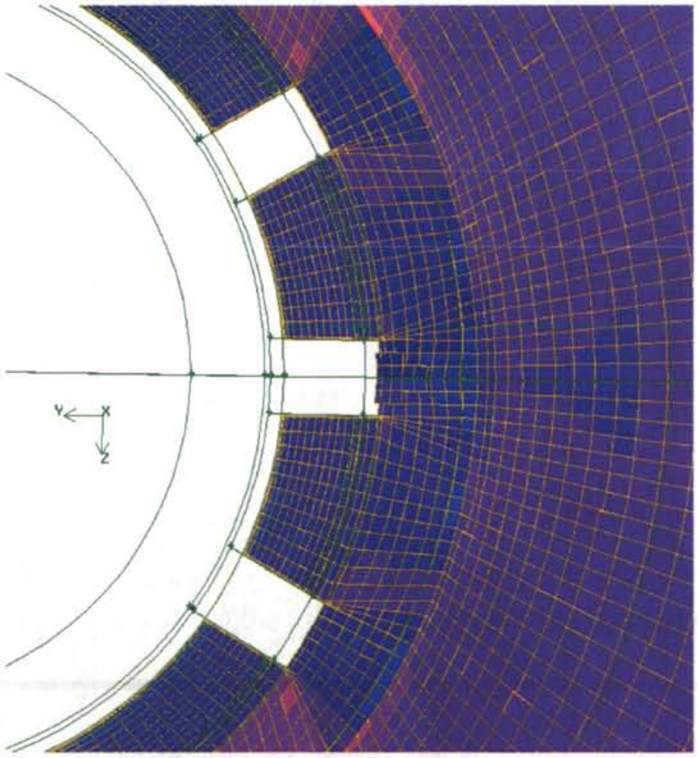

Figure A8 : Volume mesh around three rectangular FE

APPENDIX B

CALCULATION FIGURES

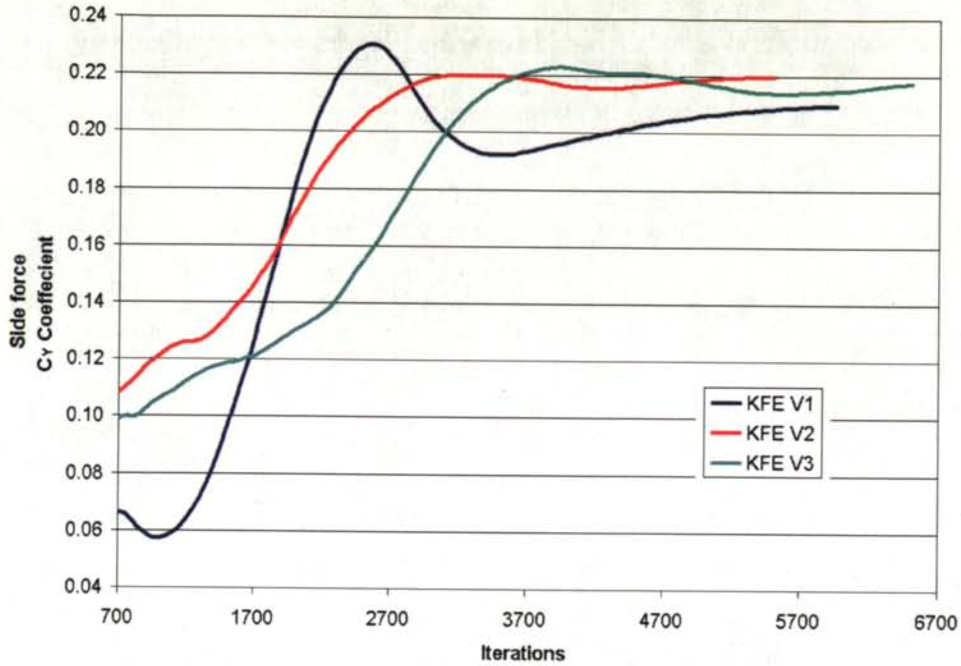

Figure B1 : Side force evolution with iterations for mesh independence with the knife-edge FE.

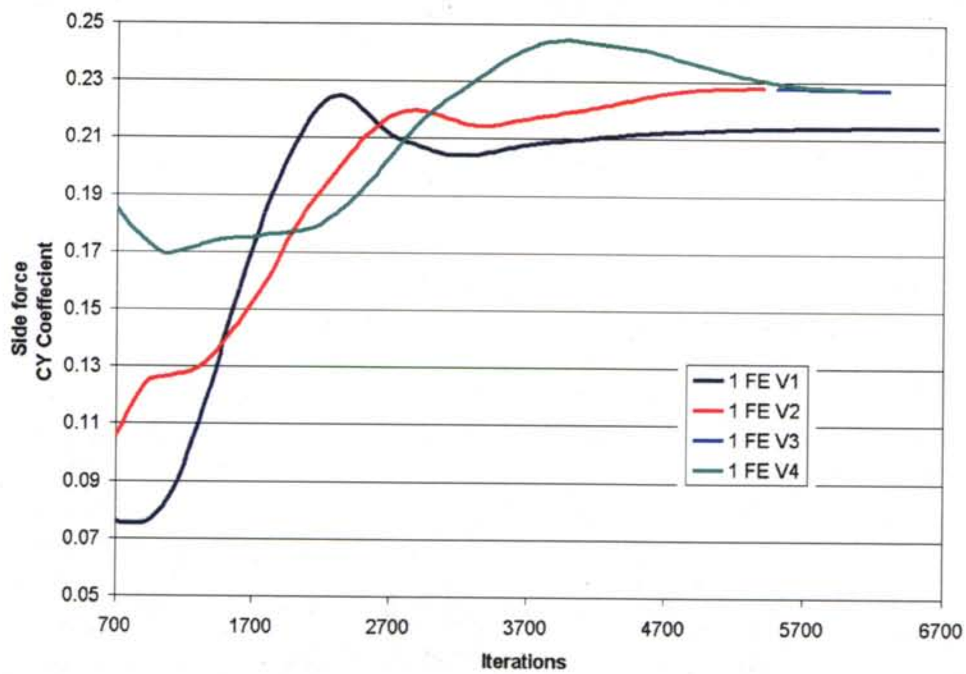

Figure B2 : Side force evolution with iterations for mesh independence with the rectangular FE

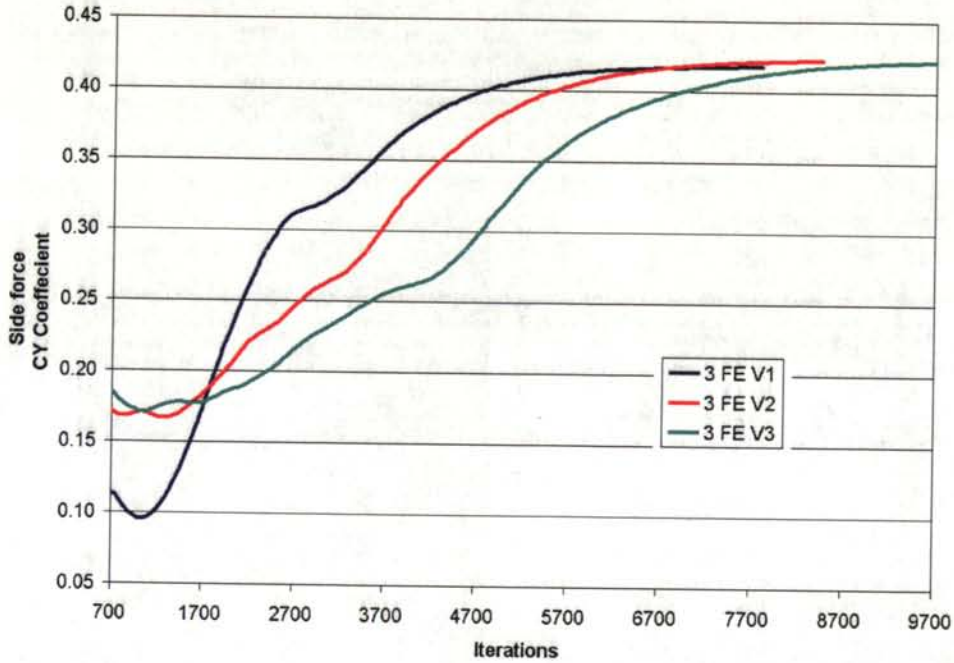

Figure B3 : Side force evolution with iterations for mesh independence with three rectangular FE

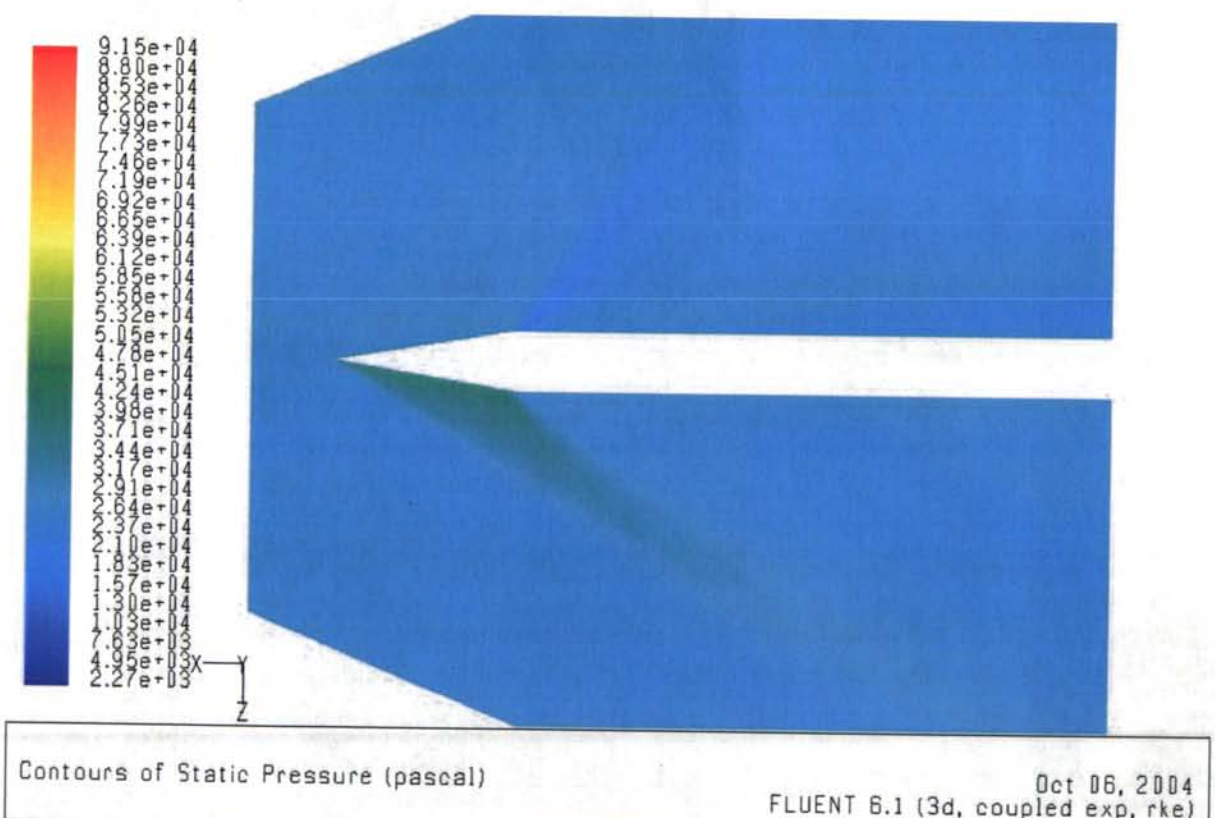

Figure B4 : Pressure contour around the missile with a 1 FE at 270° and 15° AOA

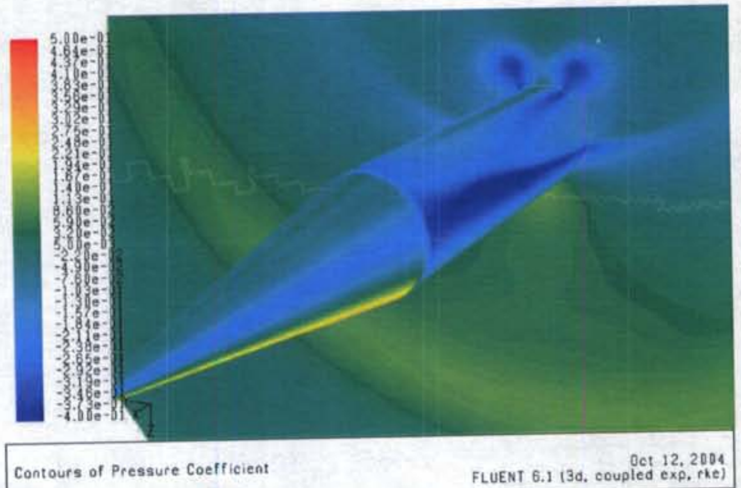

Figure B5 : Pressure profile on the wall and on a plane at pressure tap position 6 without FE

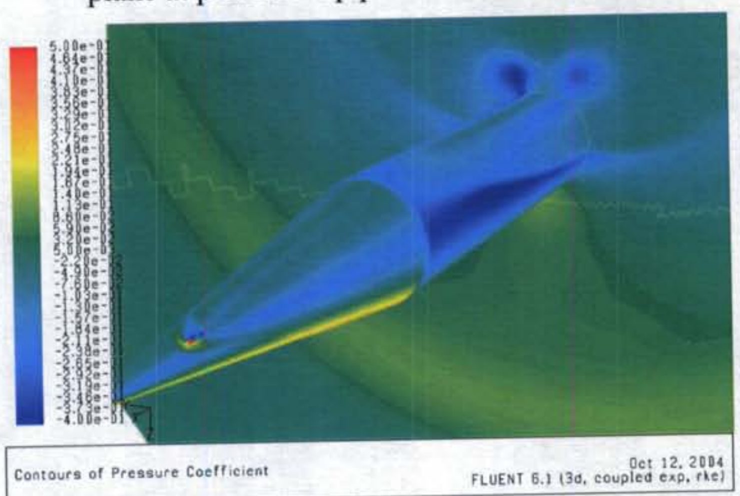

Figure B6 : Pressure profile on the wall and on a plane with 1 FE at 225° and an AOA 20°

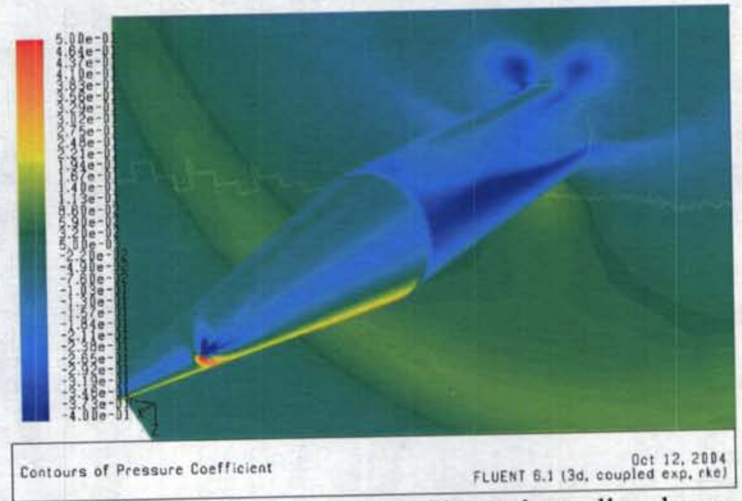

Figure B7 : Pressure profile on the wall and on a plane with 1 FE at 270° and an AOA 20°

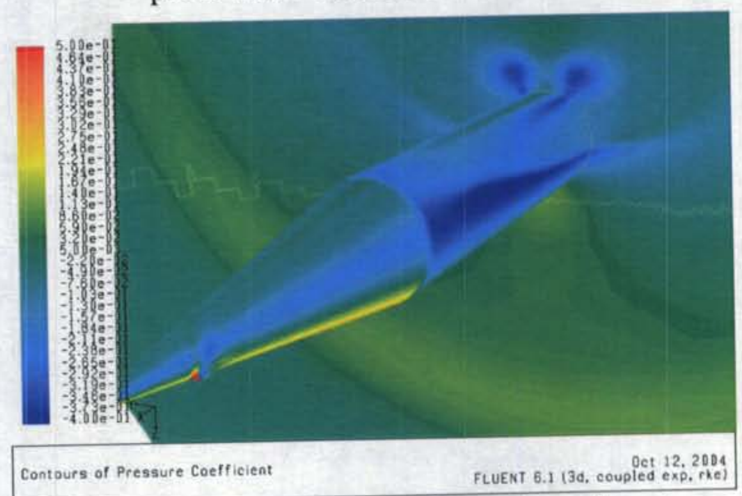

Figure B8 : Pressure profile on the wall and on a plane with 1 FE at 315° and an AOA 20°

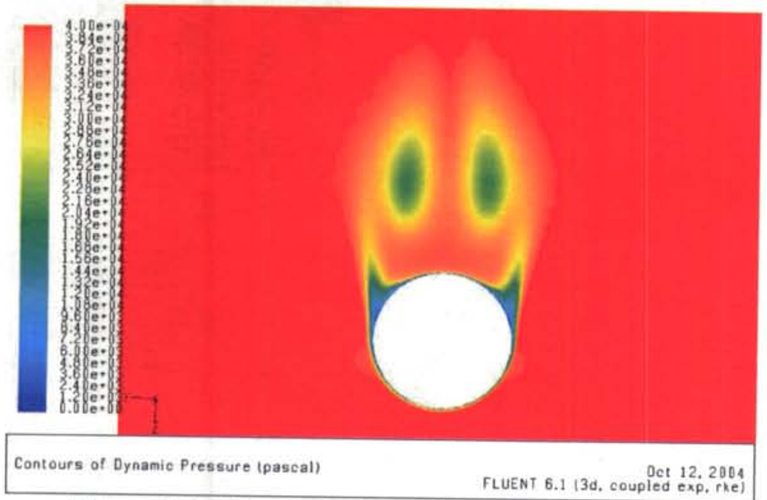

Figure B9 : Dynamic pressure at the base of the missile without FE

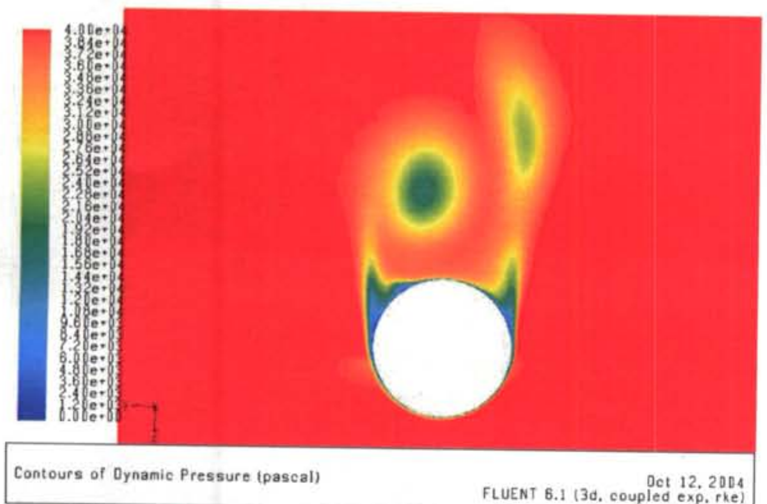

Figure B10 : Dynamic pressure at the base of the missile with 1 FE at 225° and an AOA 20°

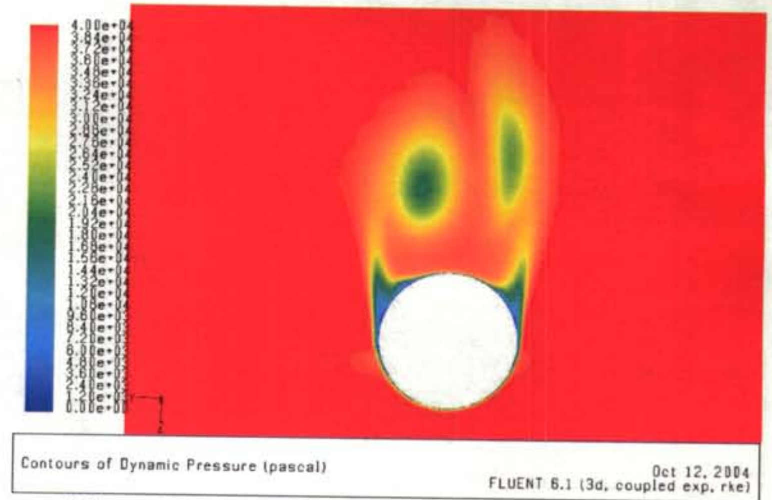

Figure B11 : Dynamic pressure at the base of the missile with 1 FE at 270° and an AOA 20°

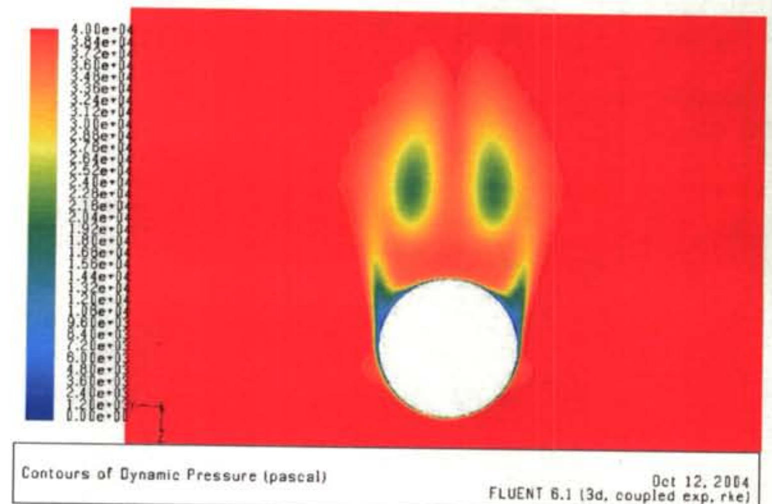

Figure B12 : Dynamic pressure at the base of the missile with 1 FE at 315° and an AOA 20°

APPENDIX C

WALL PRESSURE PROFILES

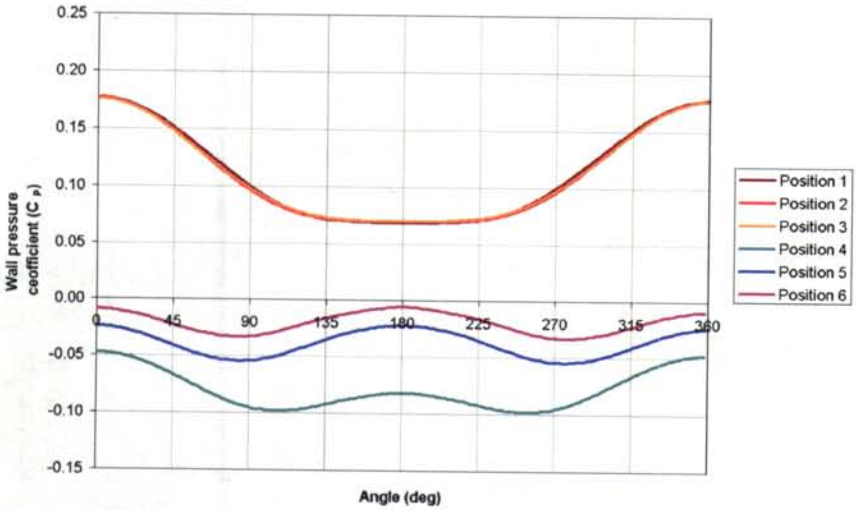

Figure C1 : Wall pressure profiles without FE at 5° AOA

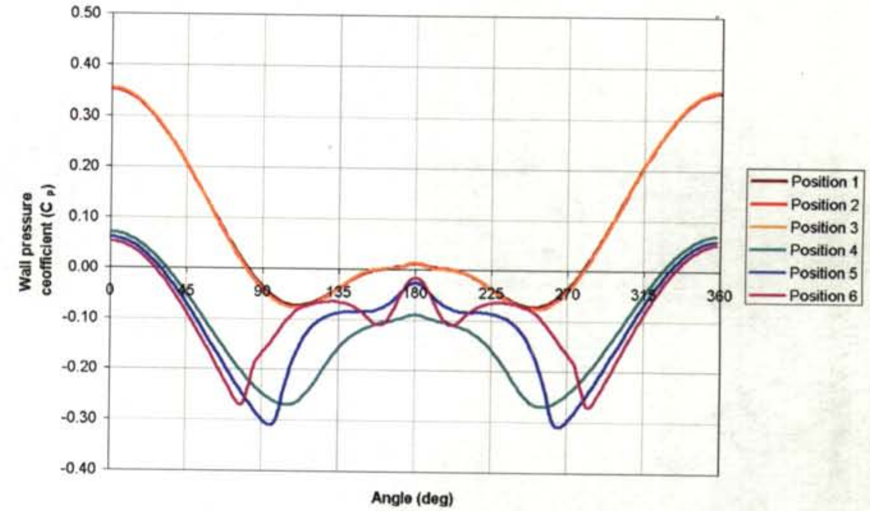

Figure C3 : Wall pressure profiles without FE at 15° AOA

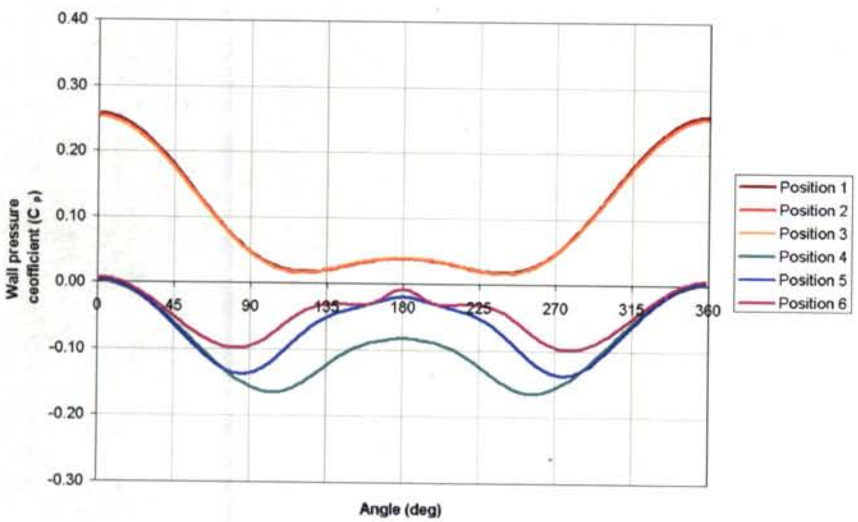

Figure C2 : Wall pressure profiles without FE at 10° AOA

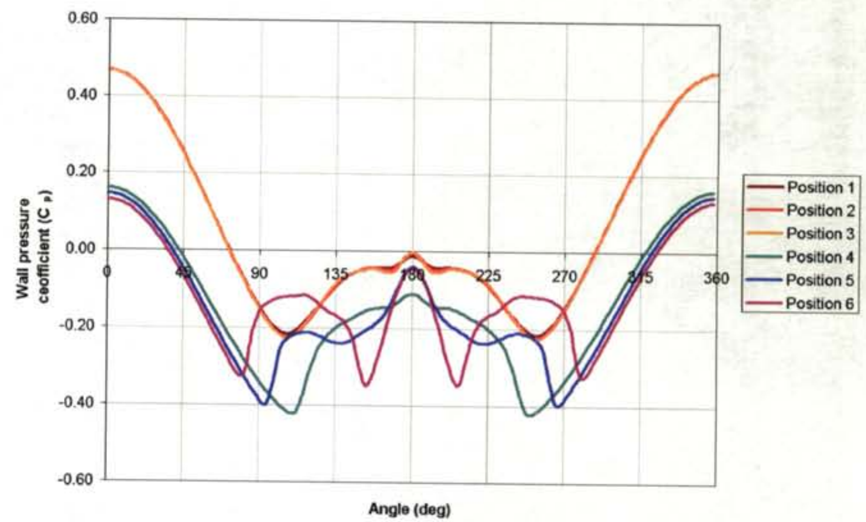

Figure C4 : Wall pressure profiles without FE at 20° AOA

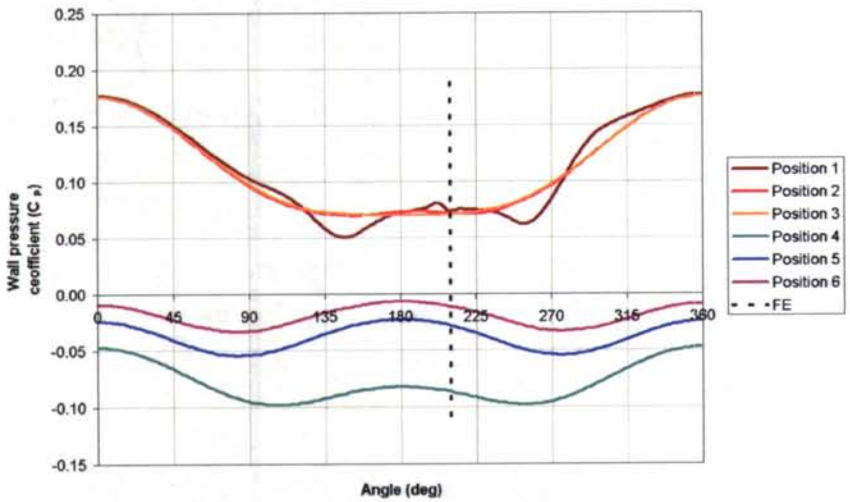

Figure C5 : Wall pressure profiles with KFE at 210° and 5° AOA

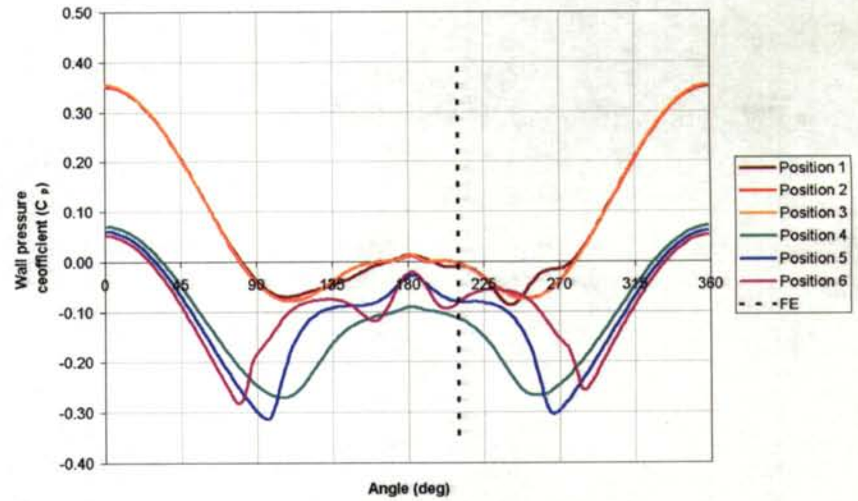

Figure C7 : Wall pressure profiles with KFE at 210° and 15° AOA

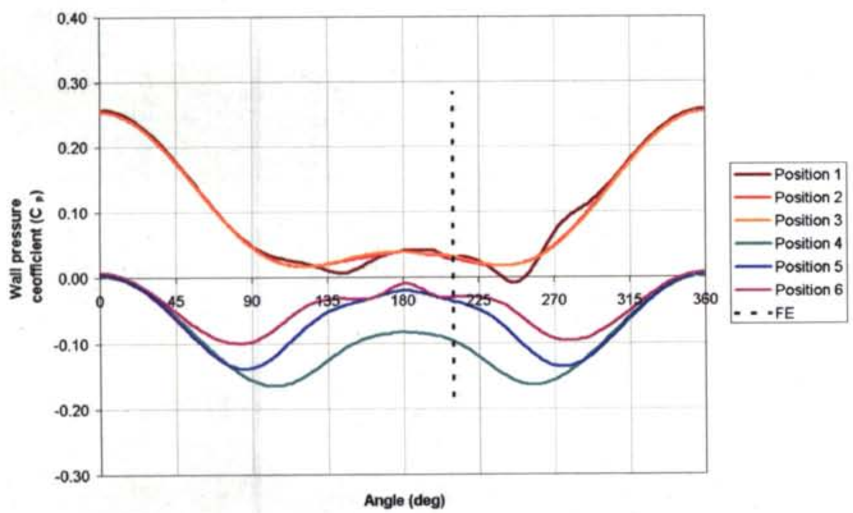

Figure C6 : Wall pressure profiles with KFE at 210° and 10° AOA

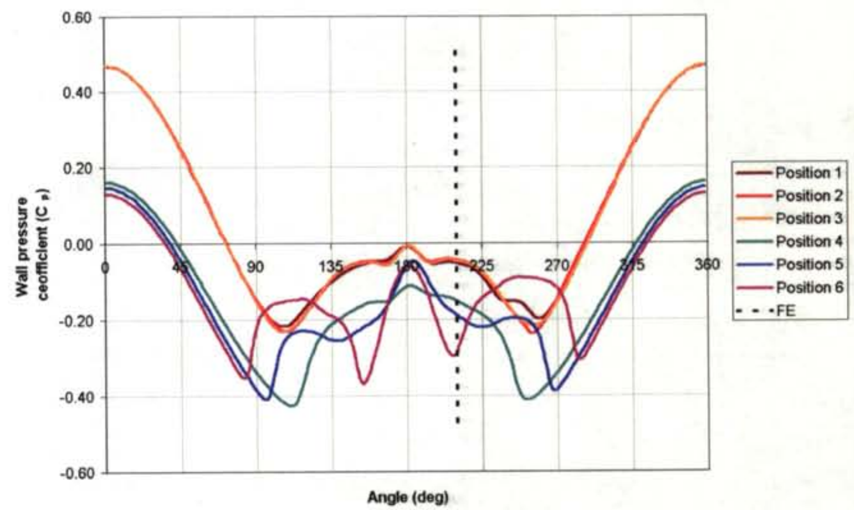

Figure C8 : Wall pressure profiles with KFE at 210° and 20° AOA

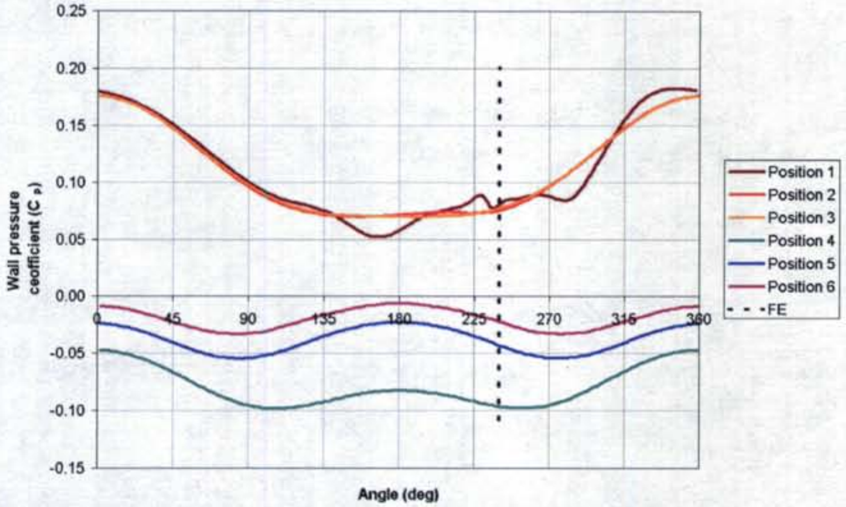

Figure C9 : Wall pressure profiles with KFE at 240° and 5° AOA

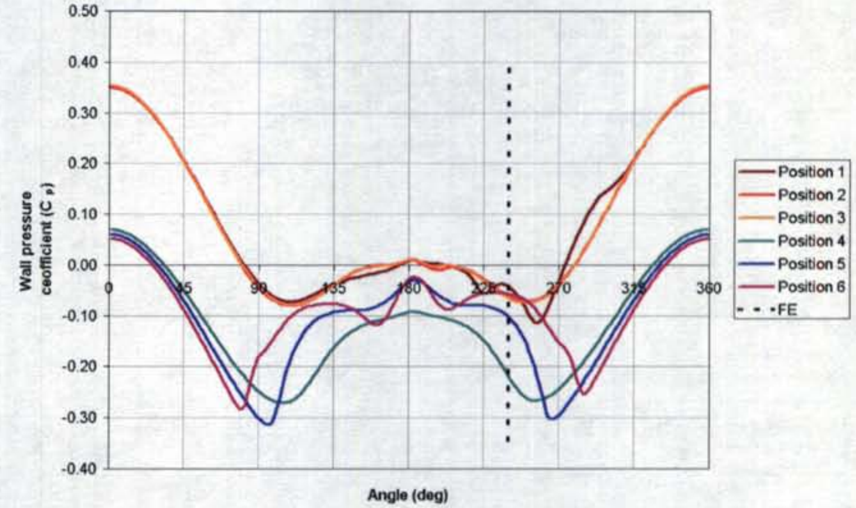

Figure C11 : Wall pressure profiles with KFE at 240° and 15° AOA

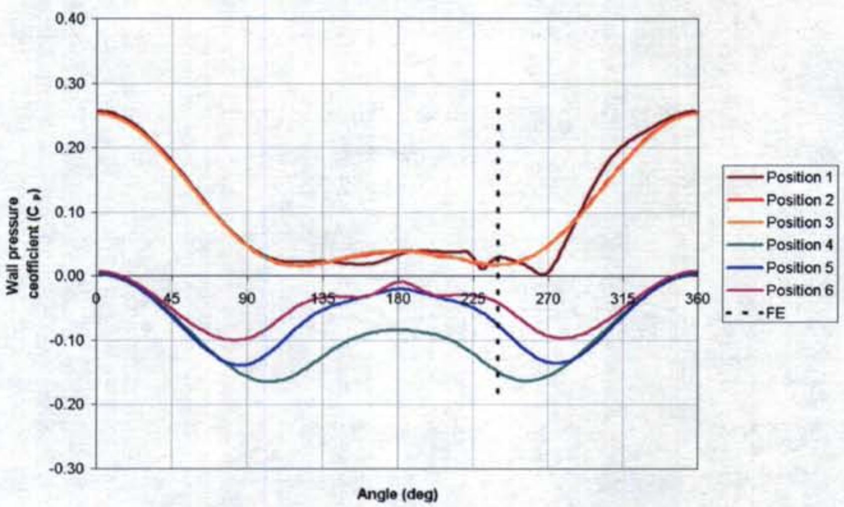

Figure C10 : Wall pressure profiles with KFE at 240° and 10° AOA

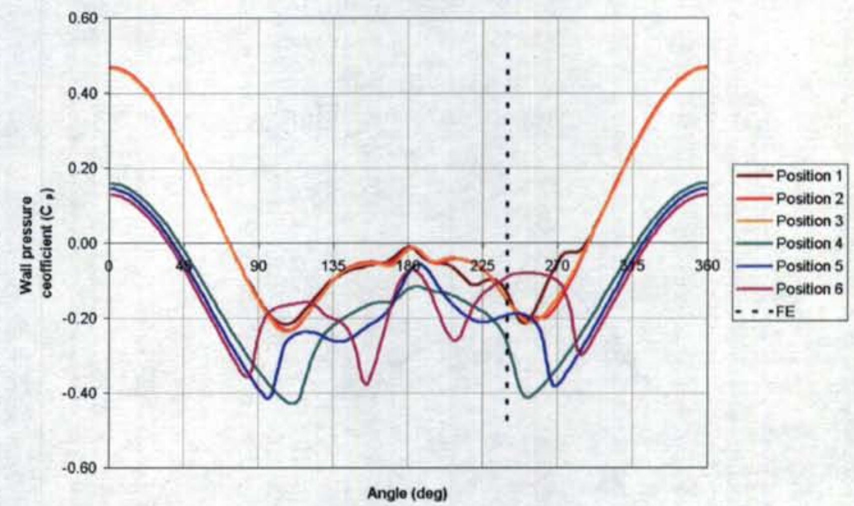

Figure C12 : Wall pressure profiles with KFE at 240° and 20° AOA

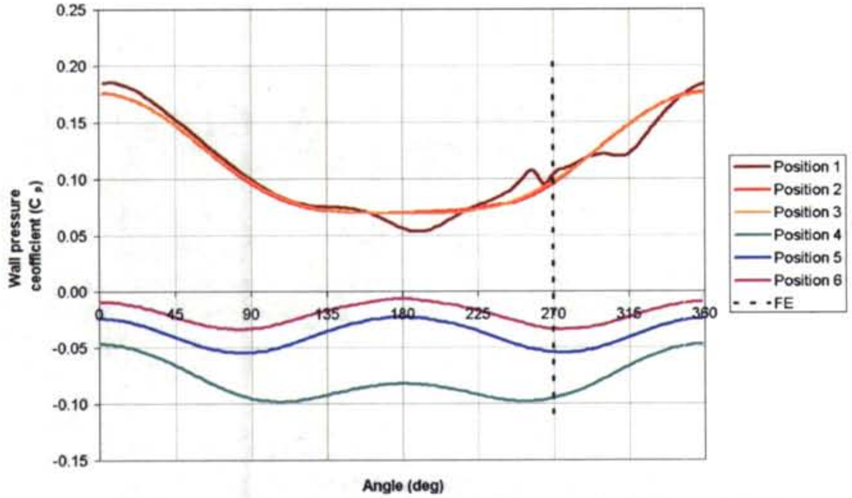

Figure C13 : Wall pressure profiles with KFE at 270° and 5° AOA

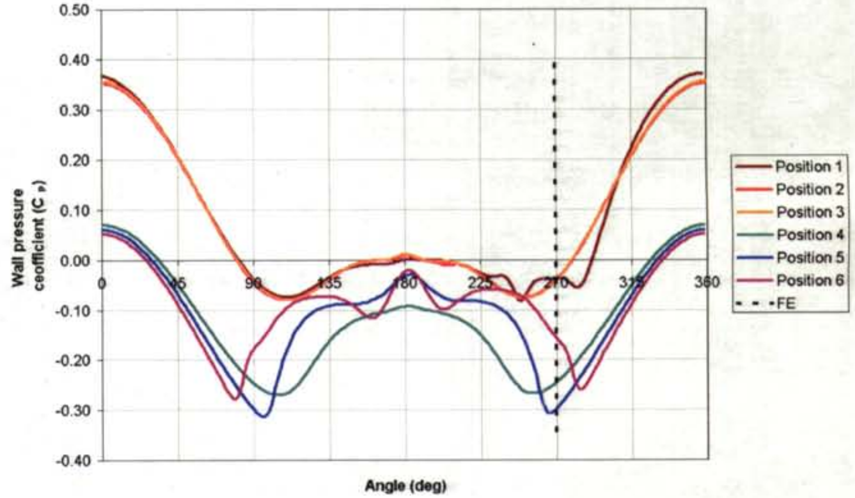

Figure C15 : Wall pressure profiles with KFE at 270° and 15° AOA

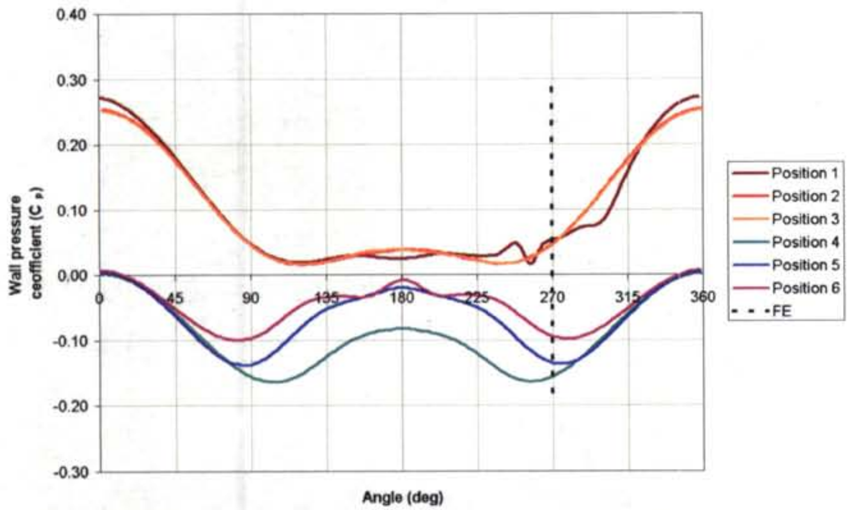

Figure C14 : Wall pressure profiles with KFE at 270° and 10° AOA

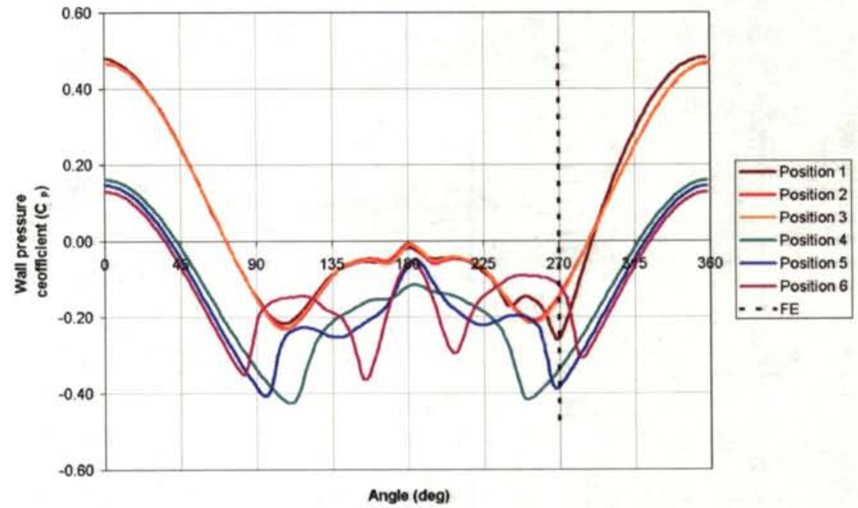

Figure C16 : Wall pressure profiles with KFE at 270° and 20° AOA

48

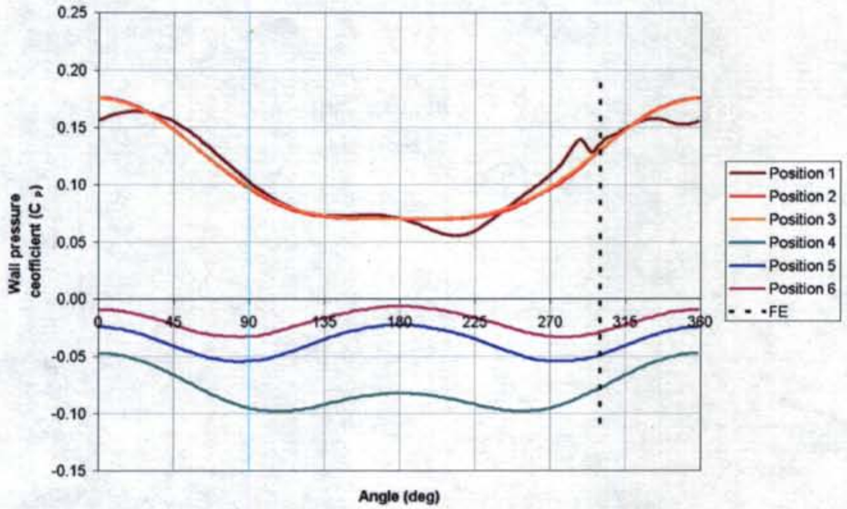

Figure C17 : Wall pressure profiles with KFE at 300° and 5° AOA

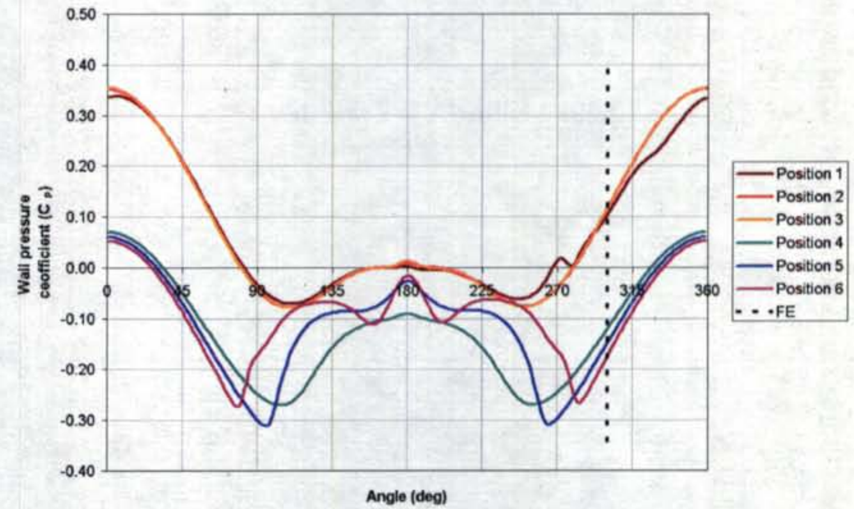

Figure C19 : Wall pressure profiles with KFE at 300° and 15° AOA

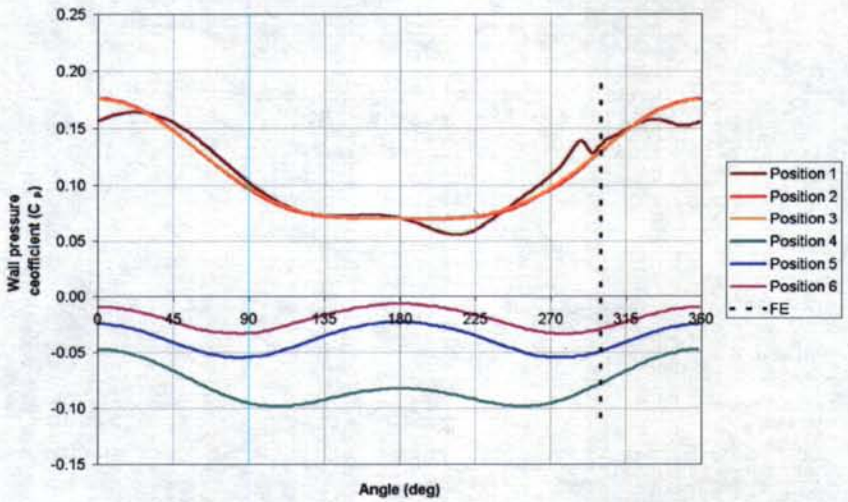

Figure C18 : Wall pressure profiles with KFE at 300° and 10° AOA

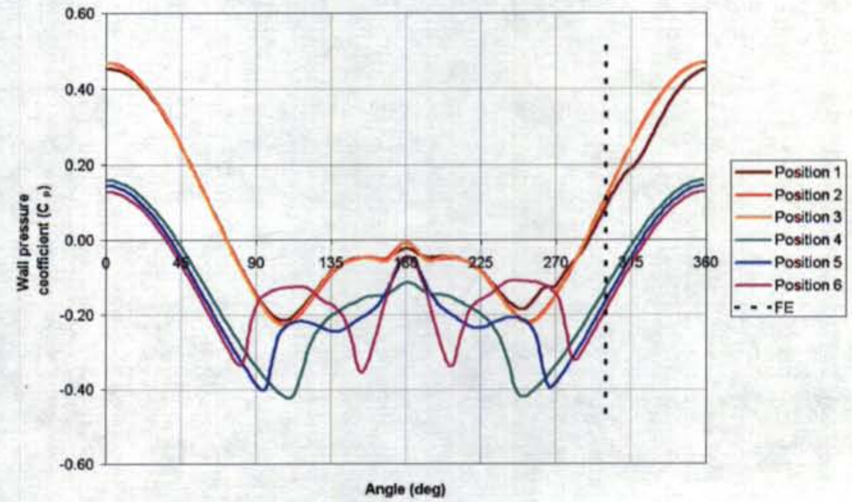

Figure C20 : Wall pressure profiles with KFE at 300° and 20° AOA

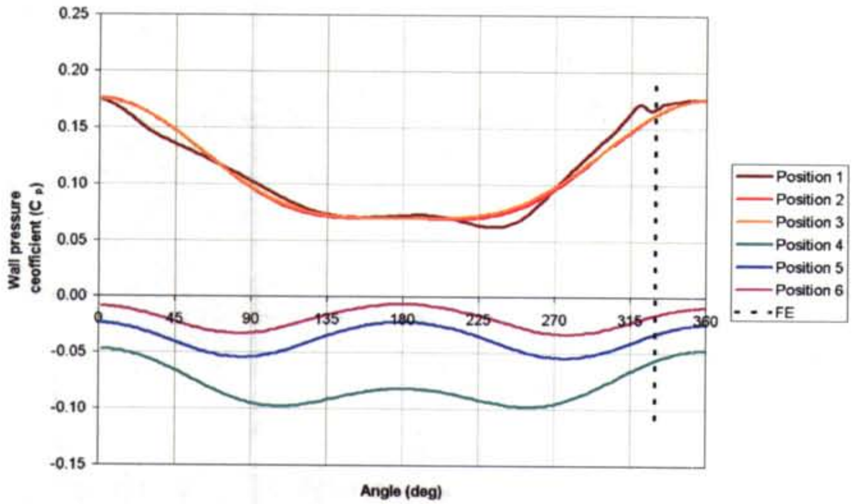

Figure C21 : Wall pressure profiles with KFE at 330° and 5° AOA

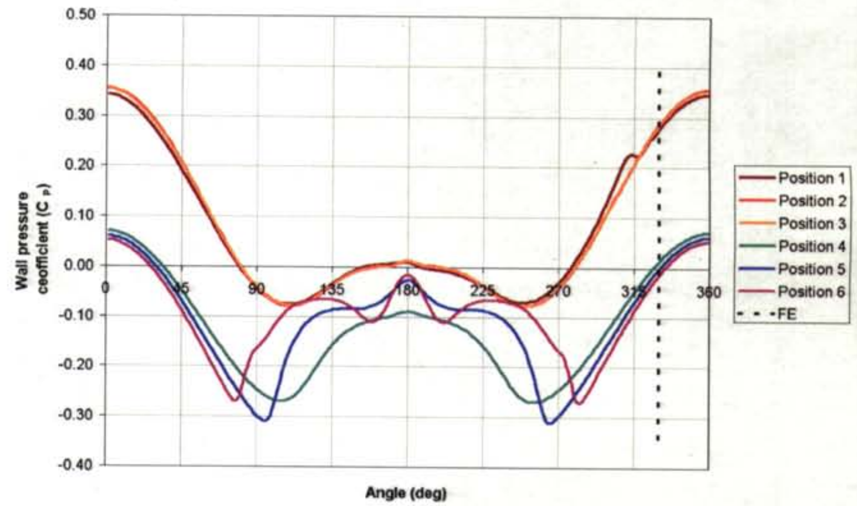

Figure C23 : Wall pressure profiles with KFE at 330° and 15° AOA

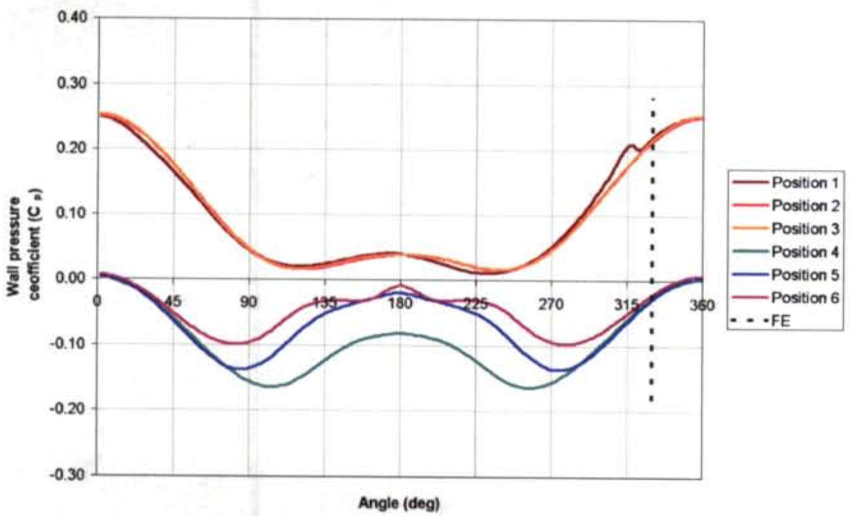

Figure C22 : Wall pressure profiles with KFE at 330° and 10° AOA

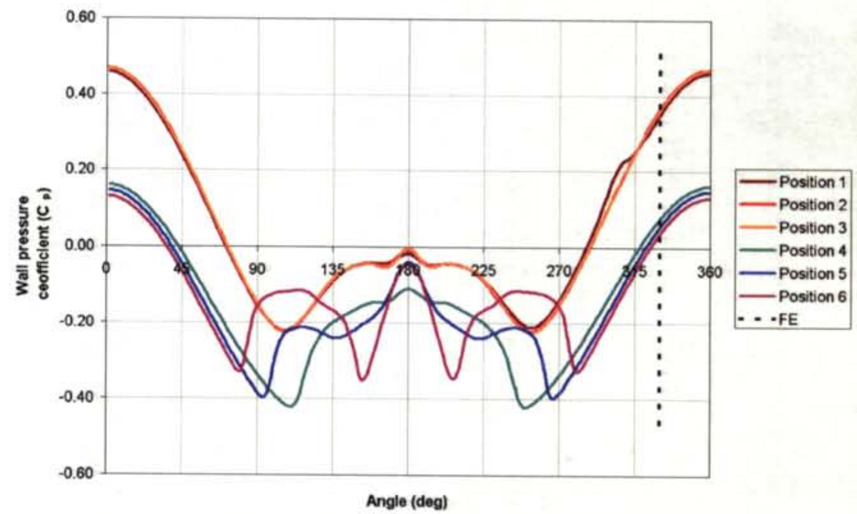

Figure C24 : Wall pressure profiles with KFE at 330° and 20° AOA

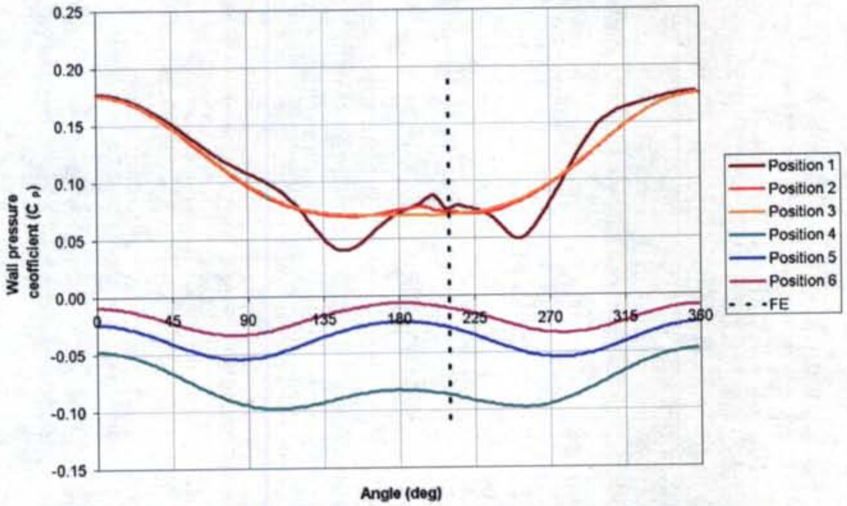

Figure C25 : Wall pressure profiles with 1 FE at 210° and 5° AOA

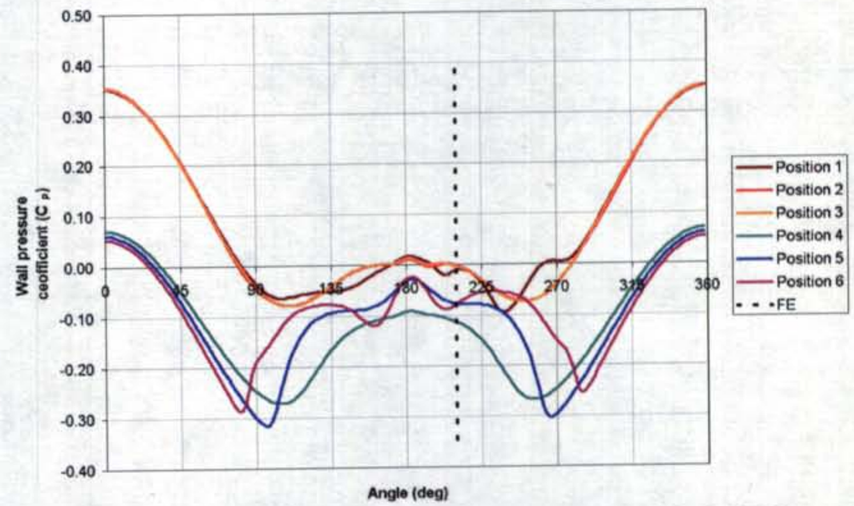

Figure C27 : Wall pressure profiles with 1 FE at 210° and 15° AOA

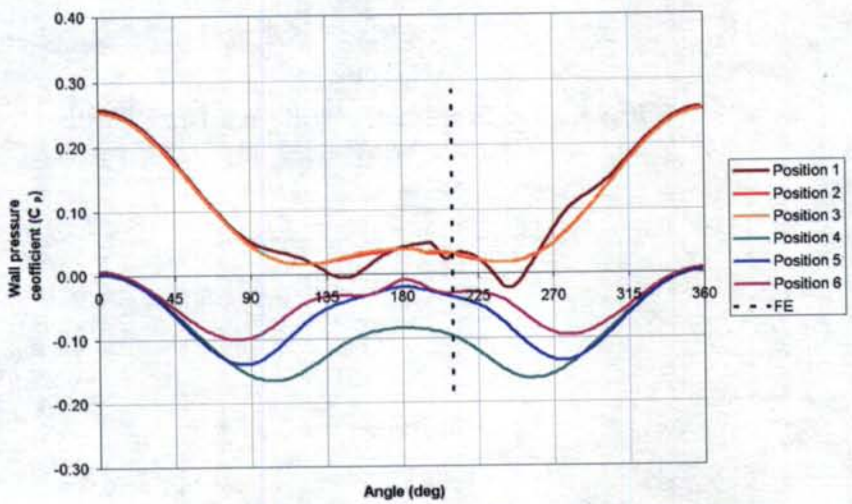

Figure C26 : Wall pressure profiles with 1 FE at 210° and 10° AOA

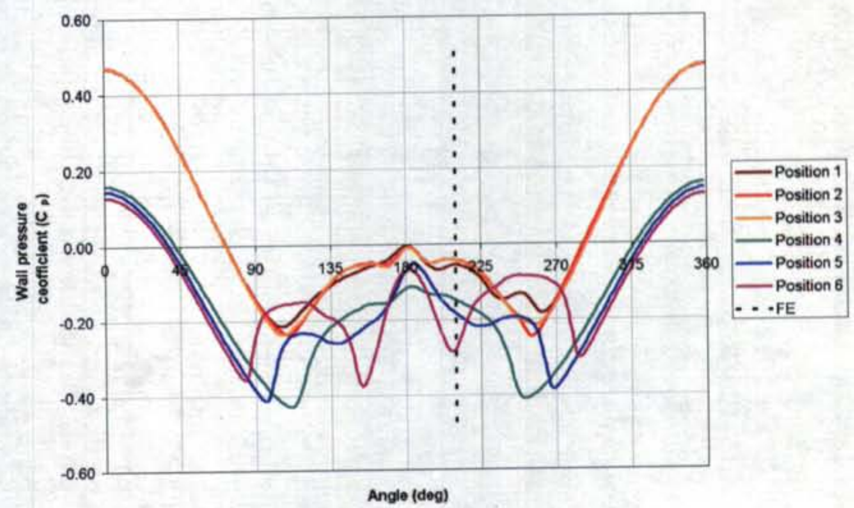

Figure C28 : Wall pressure profiles with 1 FE at 210° and 20° AOA

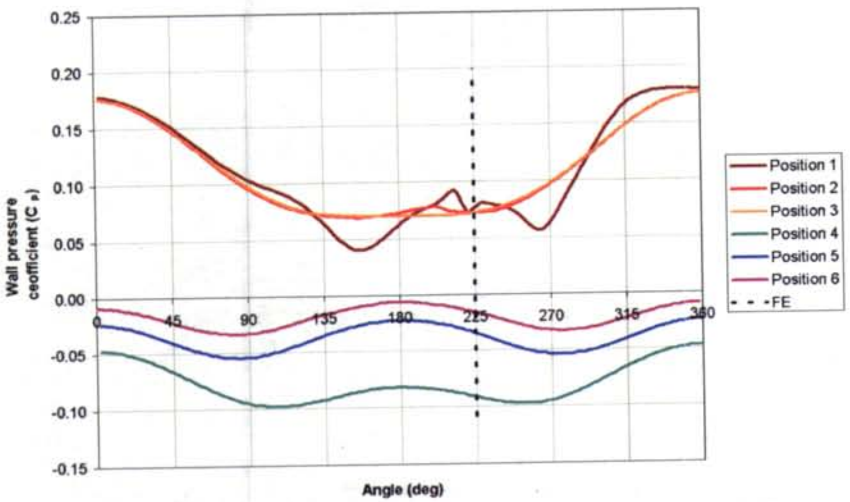

Figure C29 : Wall pressure profiles with 1 FE at 225° and 5° AOA

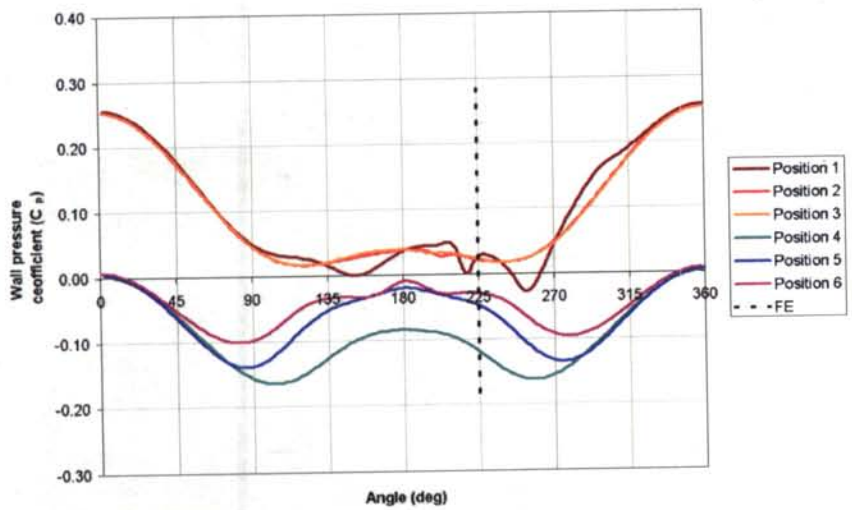

Figure C30 : Wall pressure profiles with 1 FE at 225° and 10° AOA

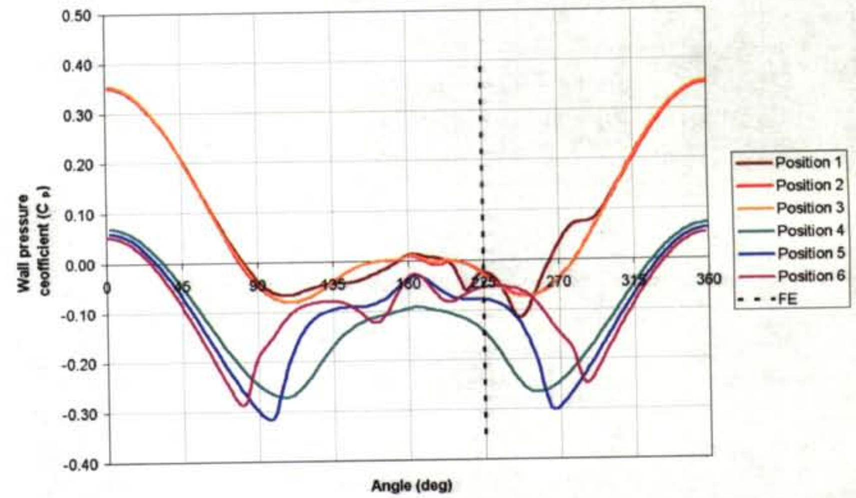

Figure C31 : Wall pressure profiles with 1 FE at 225° and 15° AOA

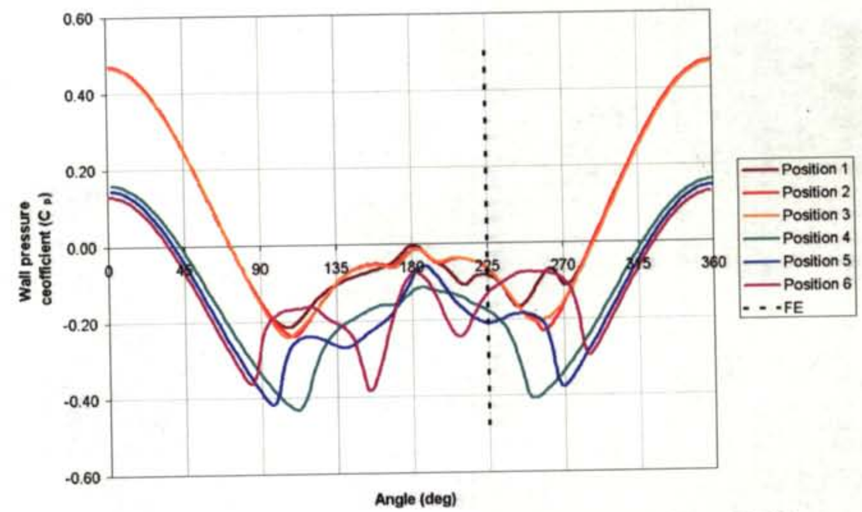

Figure C32 : Wall pressure profiles with 1 FE at 225° and 20° AOA

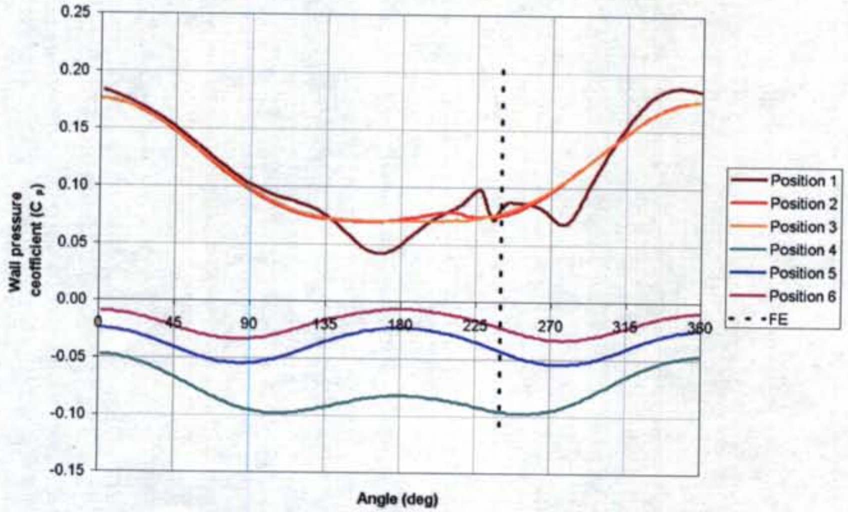

Figure C33 : Wall pressure profiles with 1 FE at 240° and 5° AOA

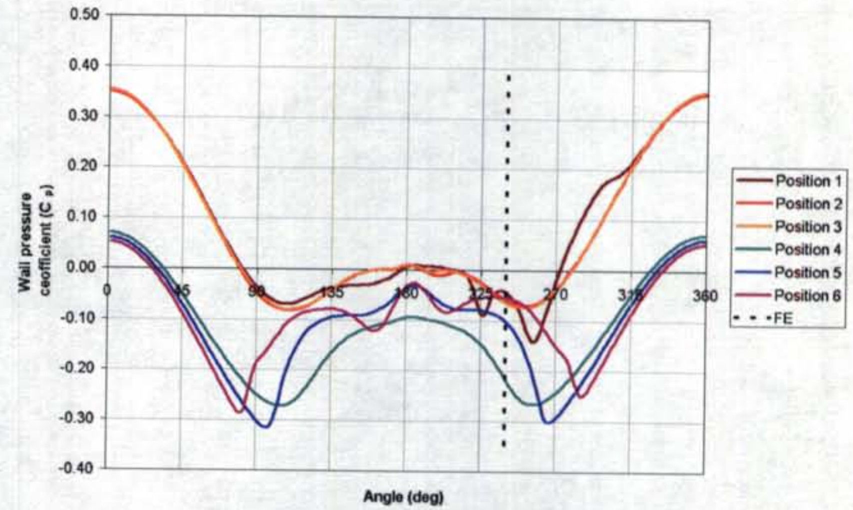

Figure C35 : Wall pressure profiles with 1 FE at 240° and 15° AOA

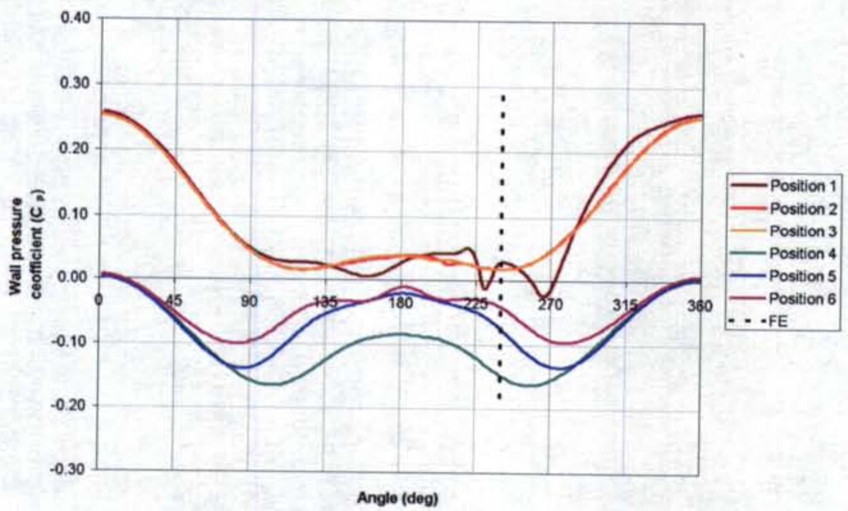

Figure C34 : Wall pressure profiles with 1 FE at 240° and 10° AOA

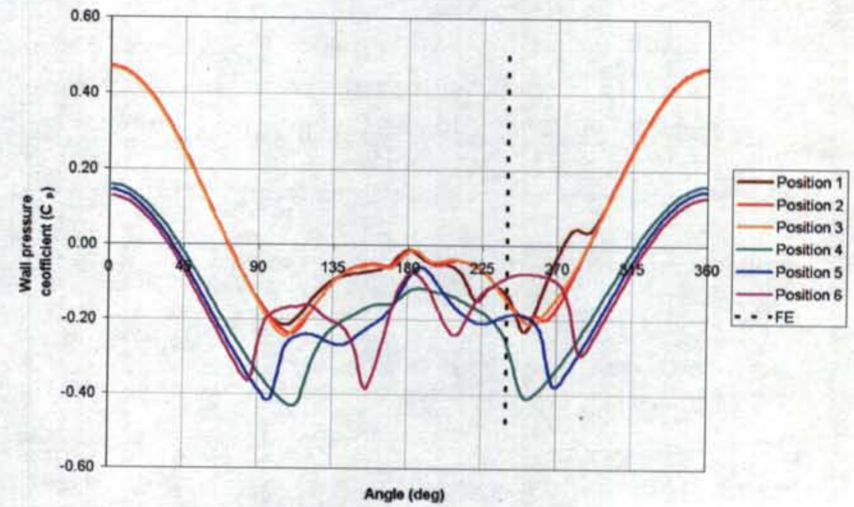

Figure C36 : Wall pressure profiles with 1 FE at 240° and 20° AOA

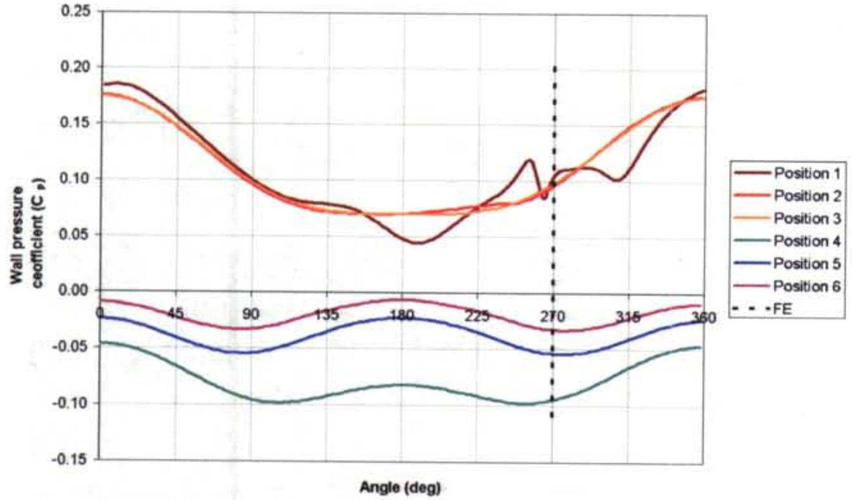

Figure C37 : Wall pressure profiles with 1 FE at 270° and 5° AOA

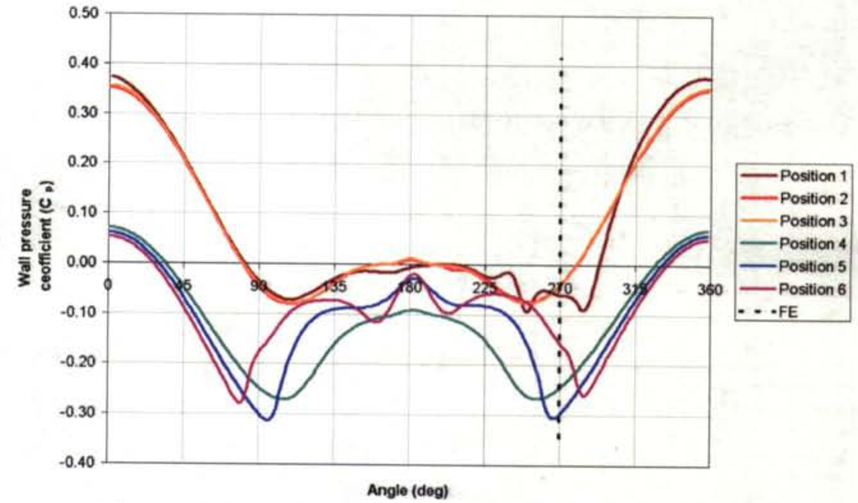

Figure C39 : Wall pressure profiles with 1 FE at 270° and 15° AOA

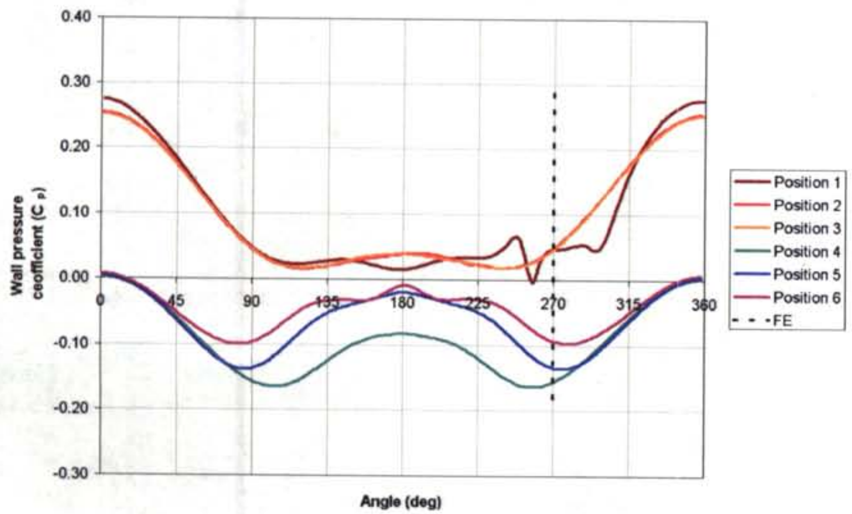

Figure C38 : Wall pressure profiles with 1 FE at 270° and 10° AOA

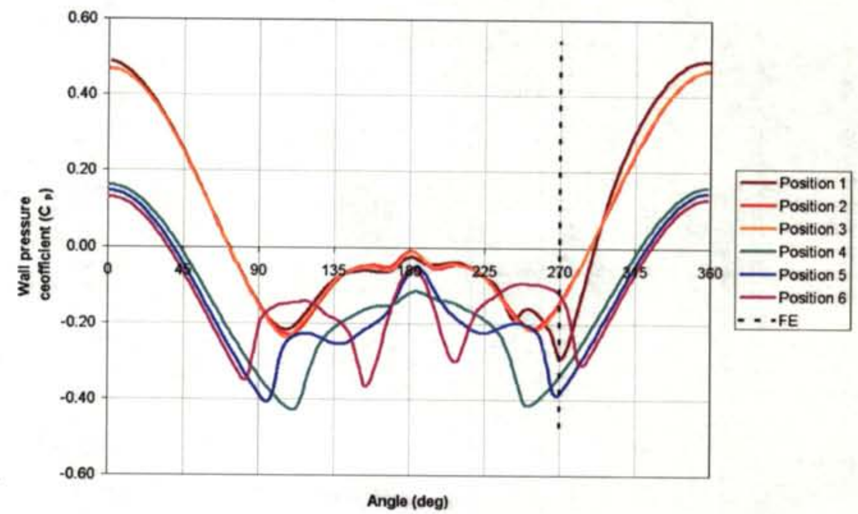

Figure C40 : Wall pressure profiles with 1 FE at 270° and 20° AOA

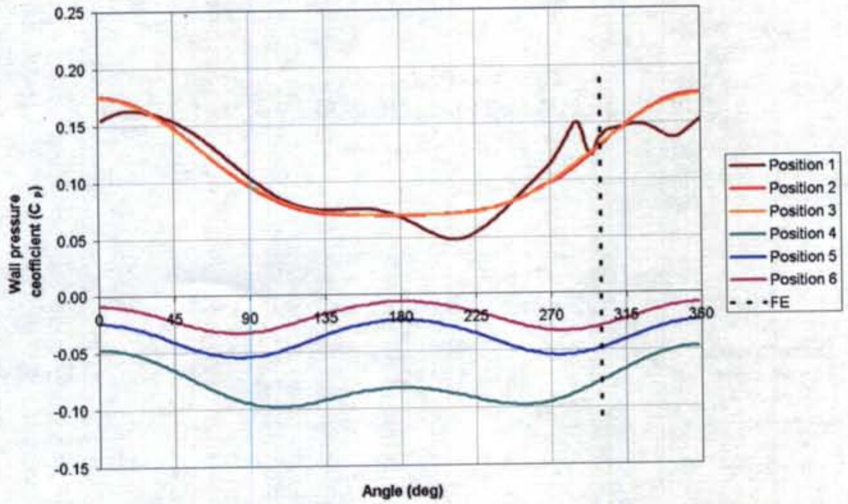

Figure C41 : Wall pressure profiles with 1 FE at 300° and 5° AOA

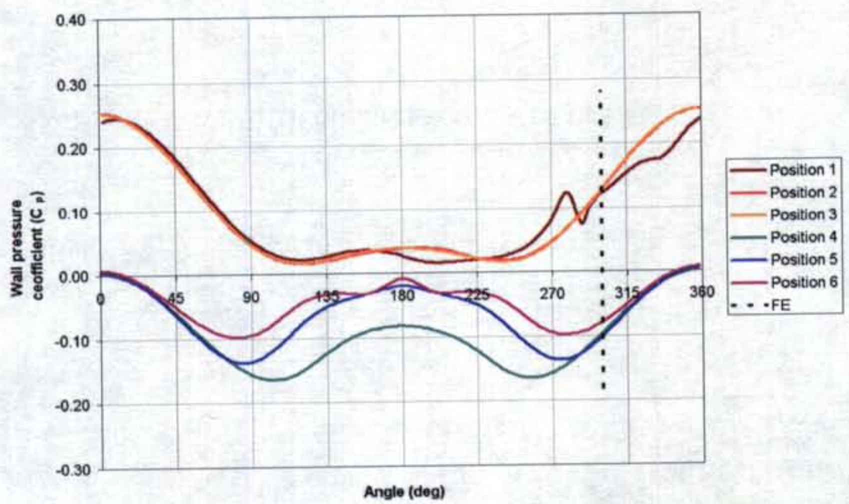

Figure C42 : Wall pressure profiles with 1 FE at 300° and 10° AOA

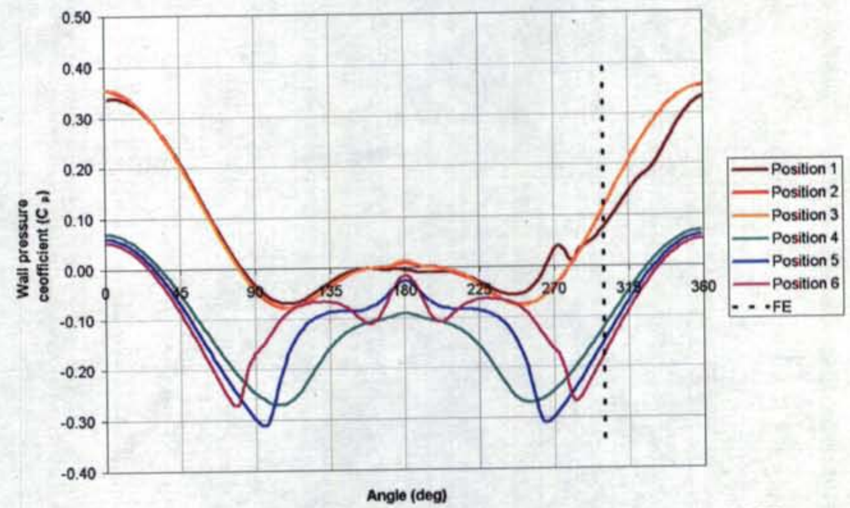

Figure C43 : Wall pressure profiles with 1 FE at 300° and 15° AOA

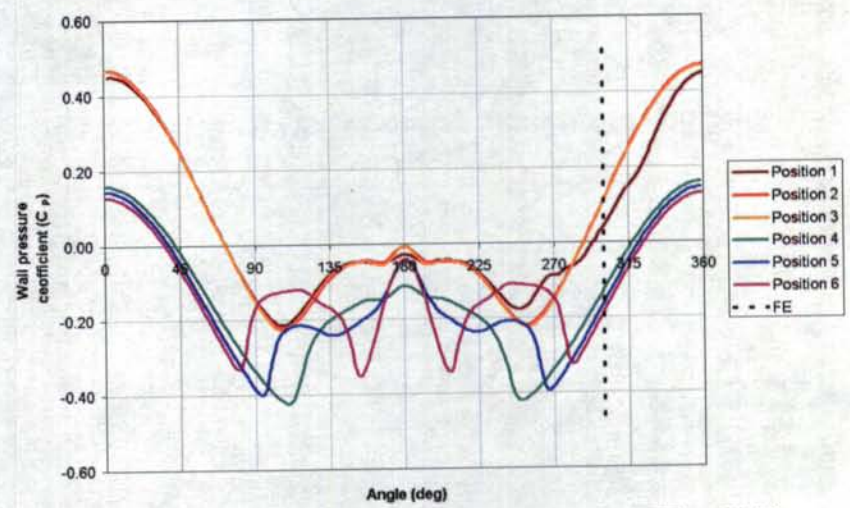

Figure C44 : Wall pressure profiles with 1 FE at 300° and 20° AOA

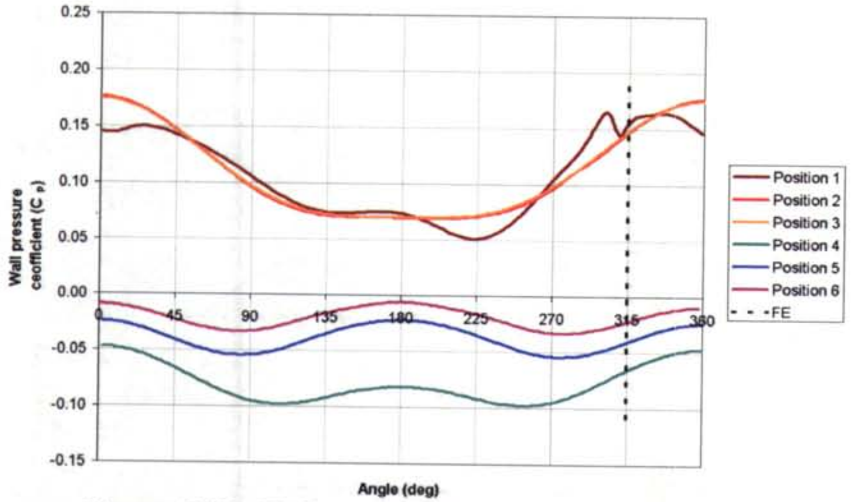

Figure C45 : Wall pressure profiles with 1 FE at 315° and 5° AOA

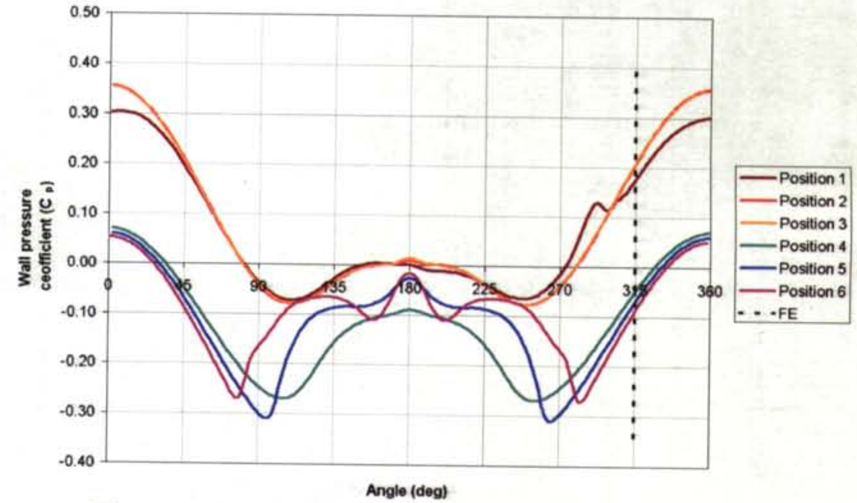

Figure C47 : Wall pressure profiles with 1 FE at 315° and 15° AOA

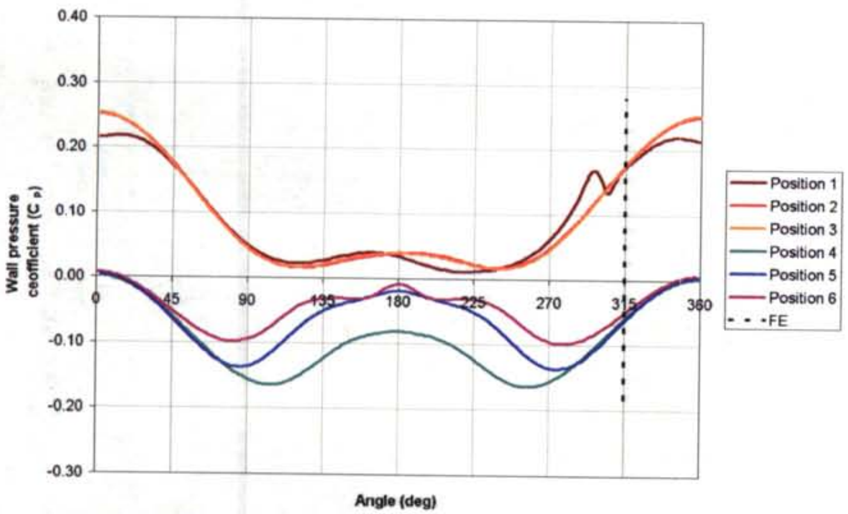

Figure C46 : Wall pressure profiles with 1 FE at 315° and 10° AOA

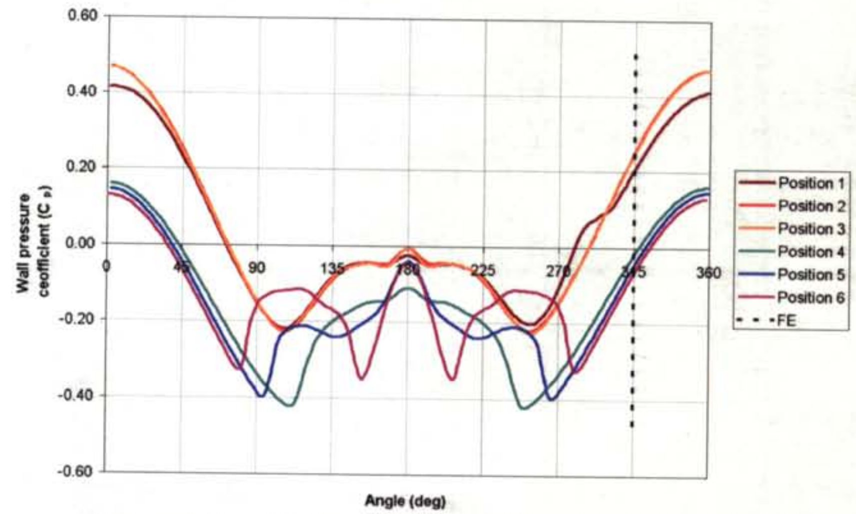

Figure C48 : Wall pressure profiles with 1 FE at 315° and 20° AOA

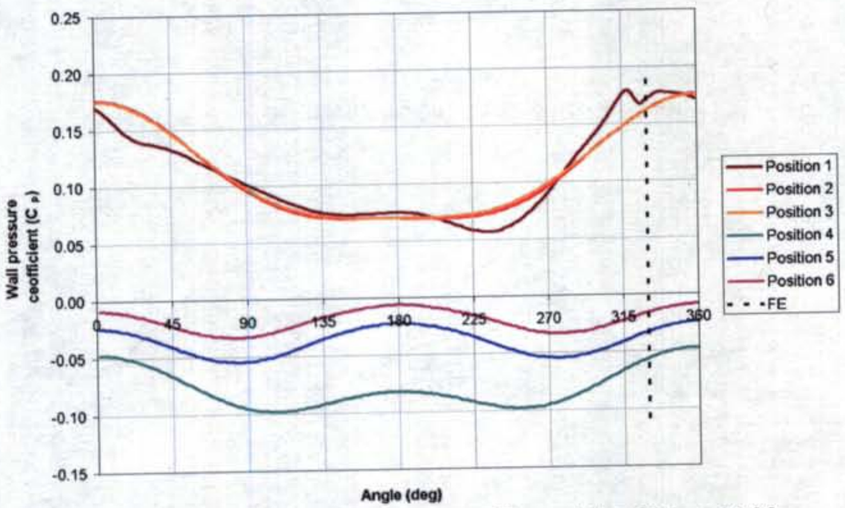

Figure C49 : Wall pressure profiles with 1 FE at 330° and 5° AOA

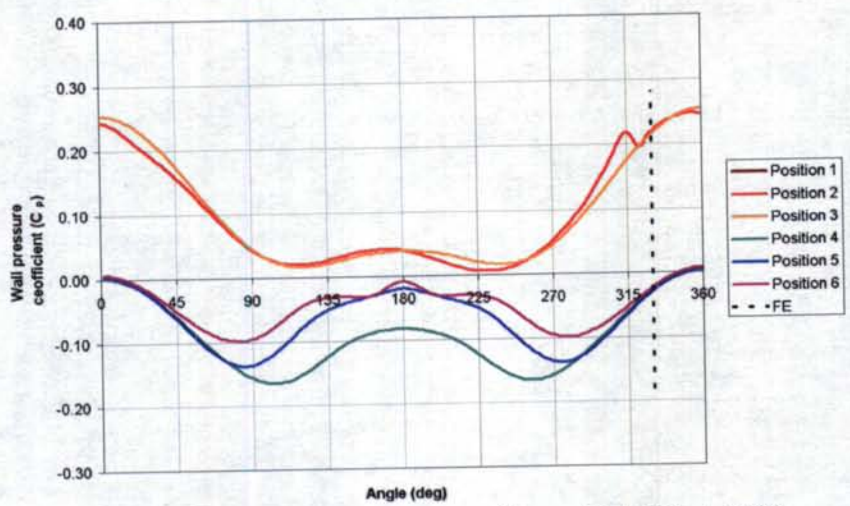

Figure C50 : Wall pressure profiles with 1 FE at 330° and 10° AOA

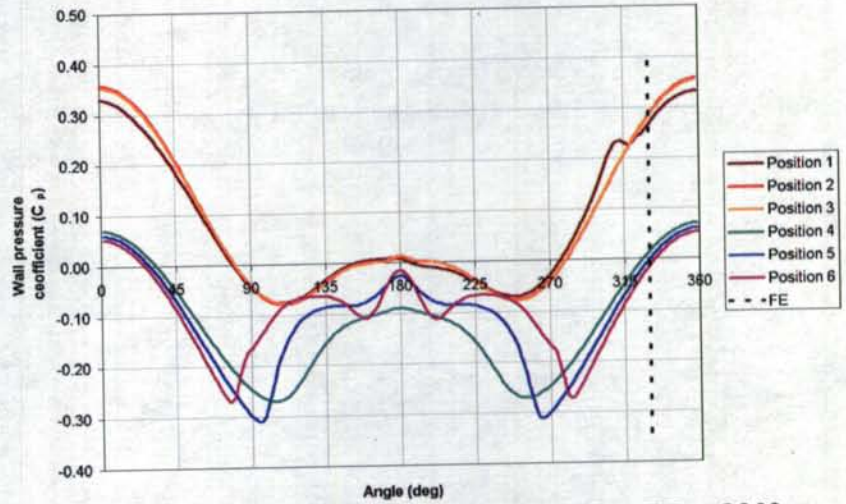

Figure C51 : Wall pressure profiles with 1 FE at 330° and 15° AOA

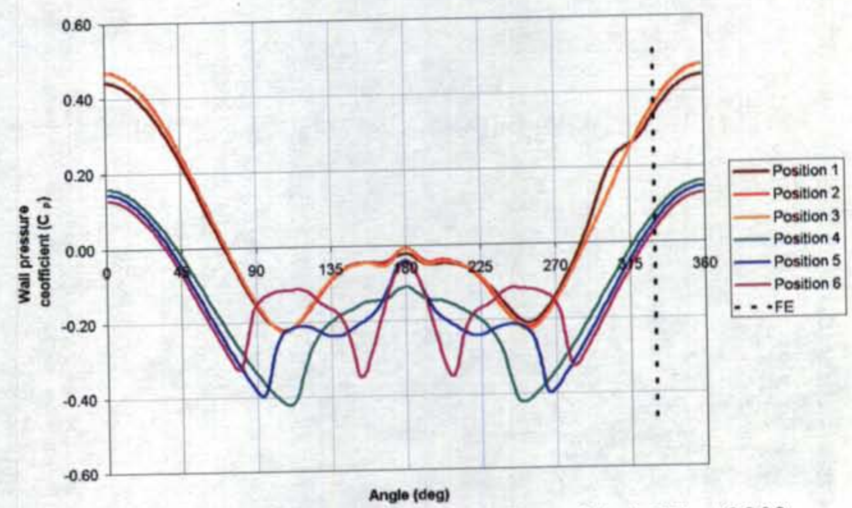

Figure C52 : Wall pressure profiles with 1 FE at 330° and 20° AOA

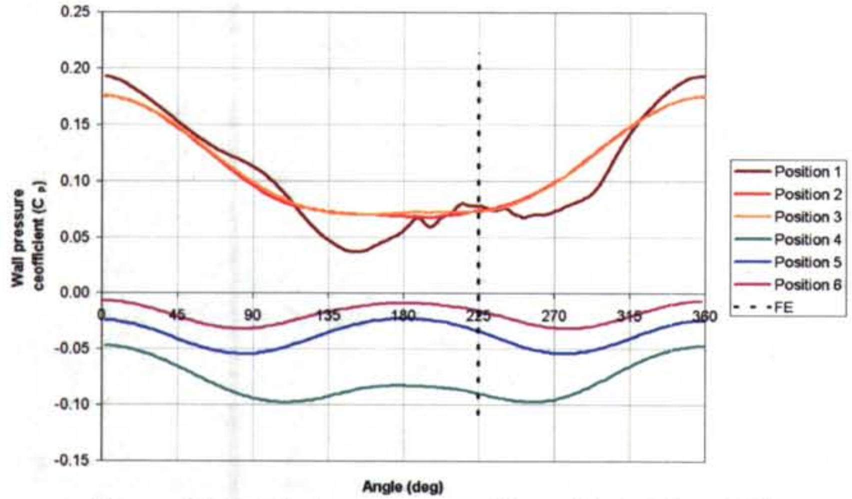

Figure C53 : Wall pressure profiles with 3 FE at 225° and 5° AOA

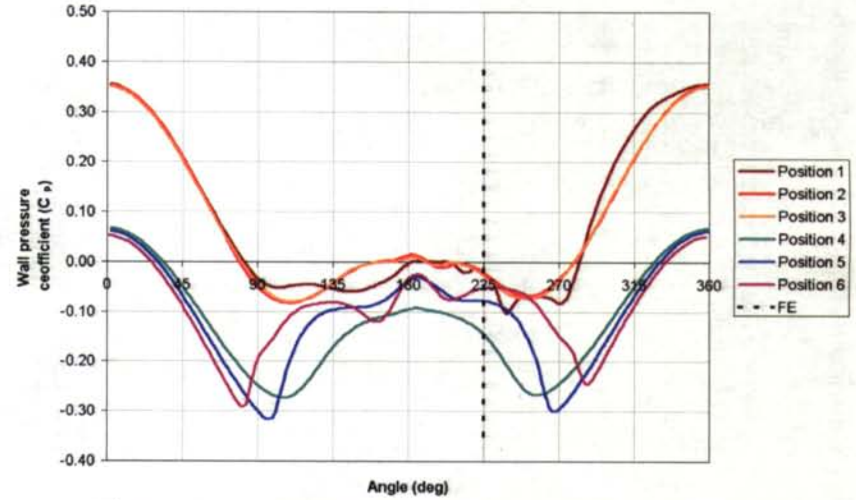

Figure C55 : Wall pressure profiles with 3 FE at 225° and 15° AOA

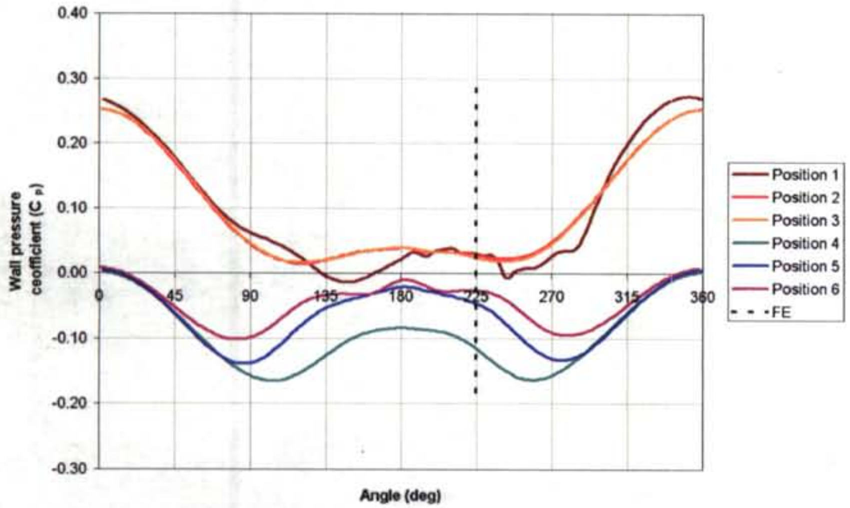

Figure C54 : Wall pressure profiles with 3 FE at 225° and 10° AOA

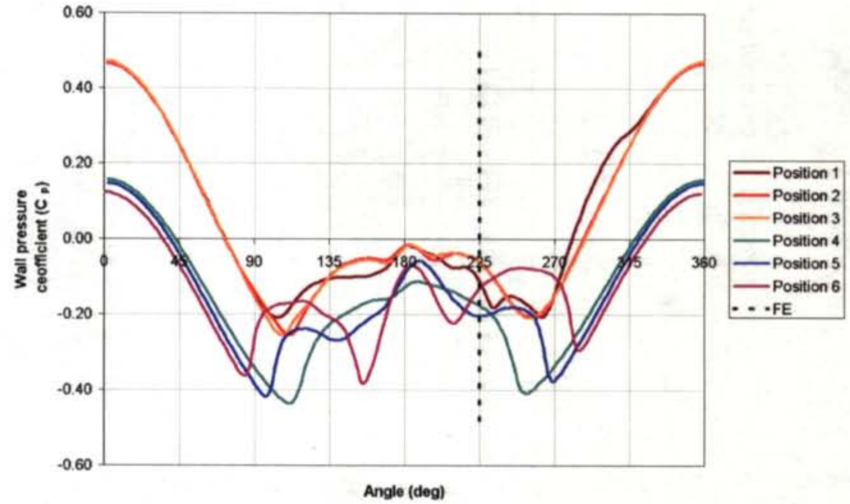

Figure C56 : Wall pressure profiles with 3 FE at 225° and 20° AOA

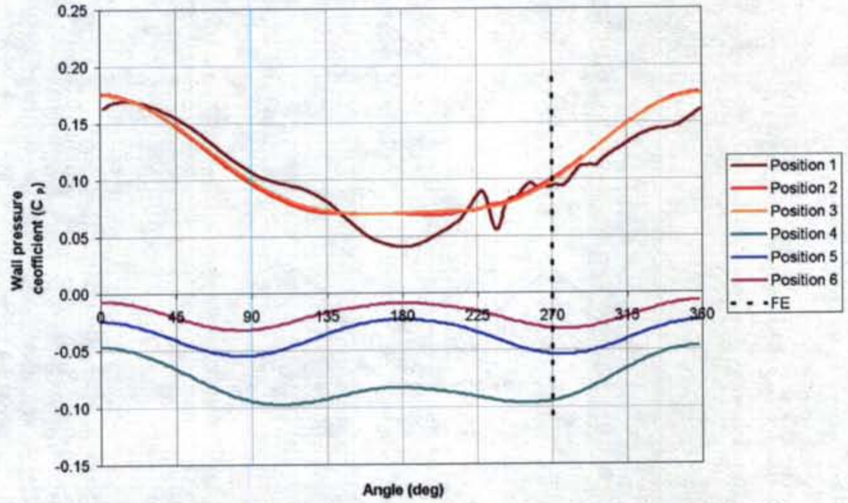

Figure C57 : Wall pressure profiles with 3 FE at 270° and 5° AOA

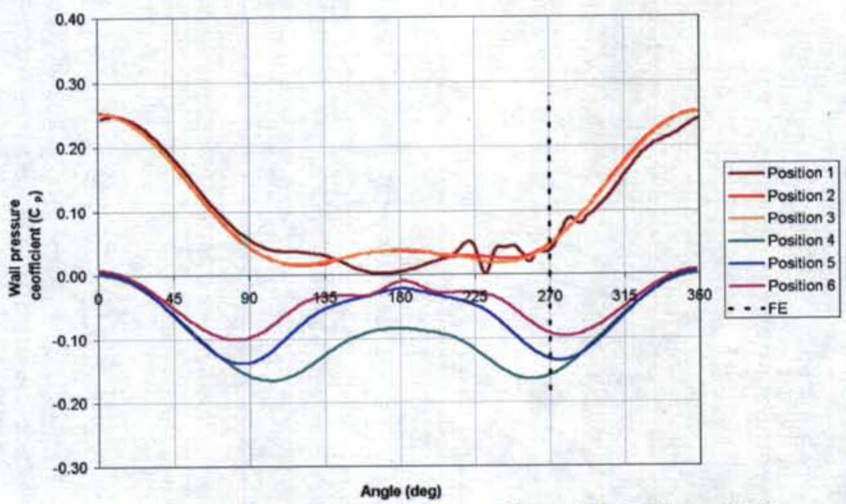

Figure C58 : Wall pressure profiles with 3 FE at 270° and 10° AOA

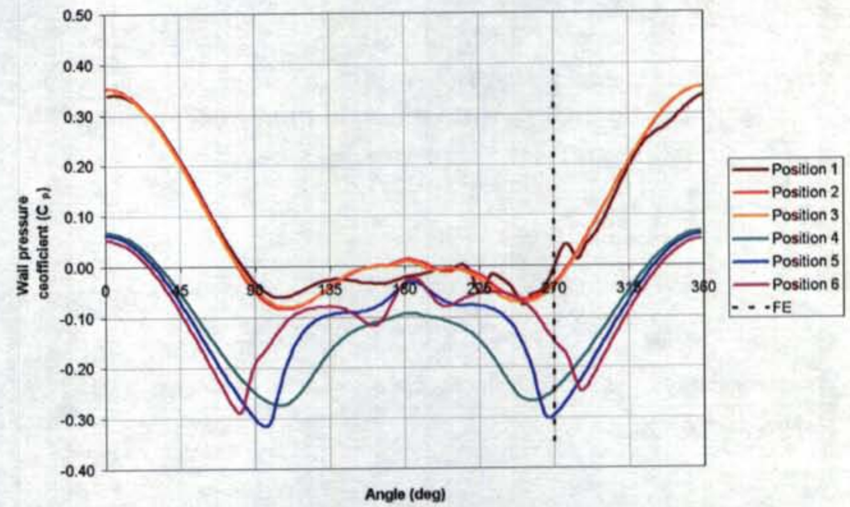

Figure C59 : Wall pressure profiles with 3 FE at 270° and 15° AOA

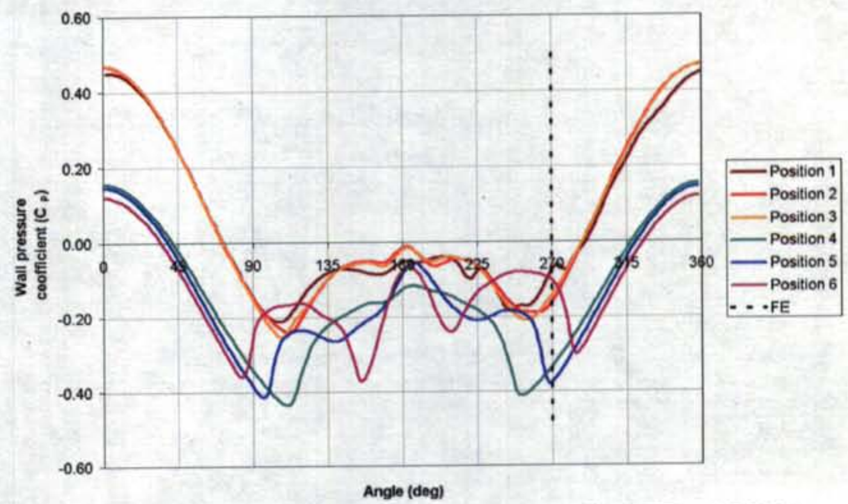

Figure C60 : Wall pressure profiles with 3 FE at 270° and 20° AOA

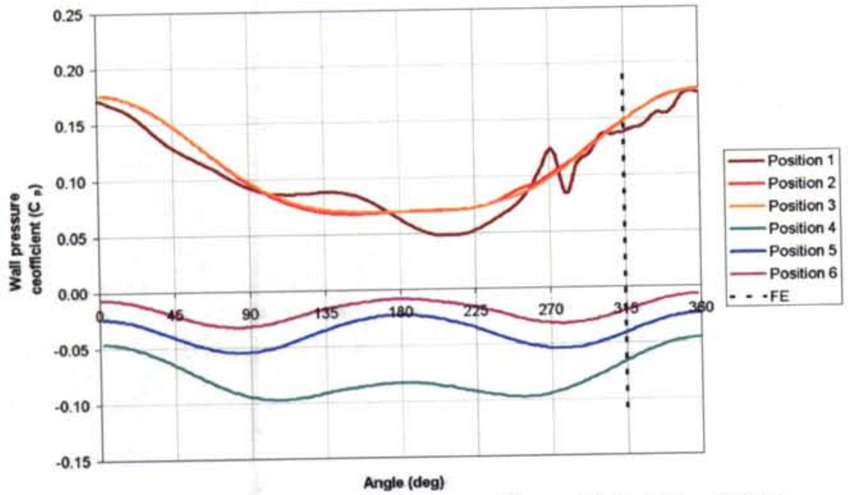

Figure C61 : Wall pressure profiles with 3 FE at 315° and 5° AOA

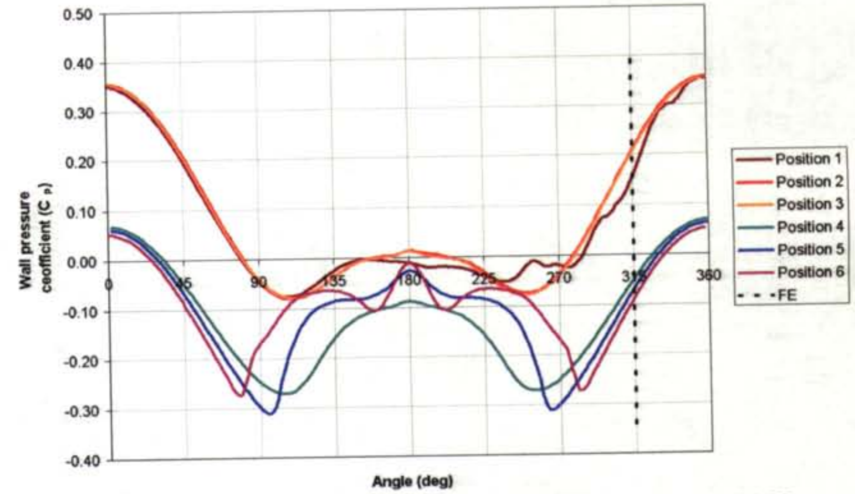

Figure C63 : Wall pressure profiles with 3 FE at 315° and 15° AOA

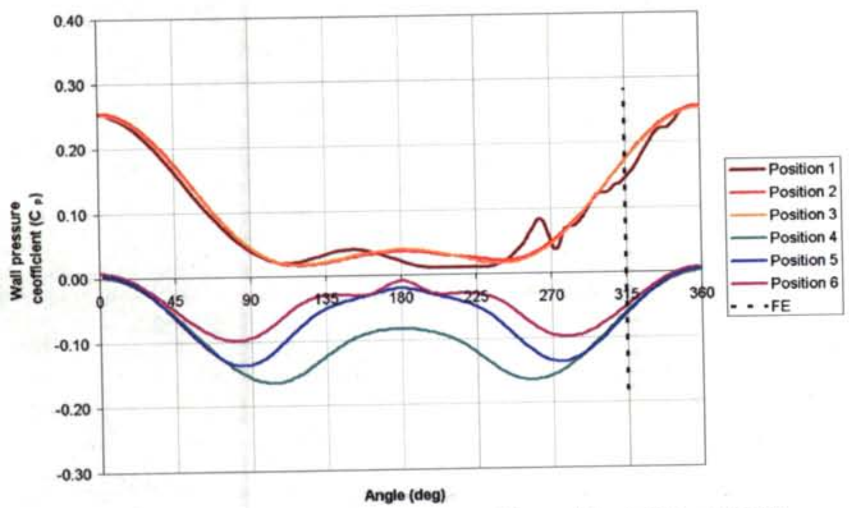

Figure C62 : Wall pressure profiles with 3 FE at 315° and 10° AOA

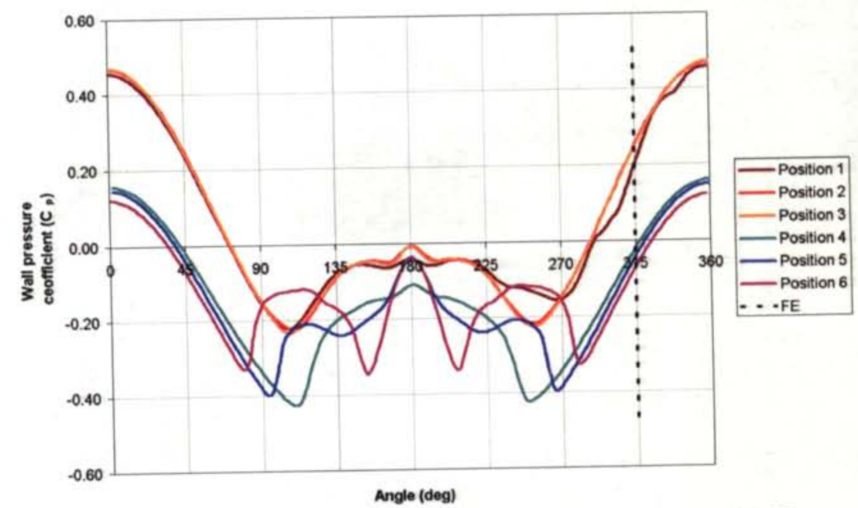

Figure C64 : Wall pressure profiles with 3 FE at 315° and 20° AOA

Wind tunnel measurement show a transition point of the main vortex structure at an AOA around 17 degrees. Theory propose that the transition happen at an AOA equal to the cone angle of 19 degrees. Additional calculation was done to know if it is possible to capture the transition of the main vortices with the calculation code, Fluent™. Calculation with one rectangular FE placed at a roll angle position of 225 degrees and an AOA 25 degrees and calculation without FE at an AOA of 25 degrees and 30 degrees was done.

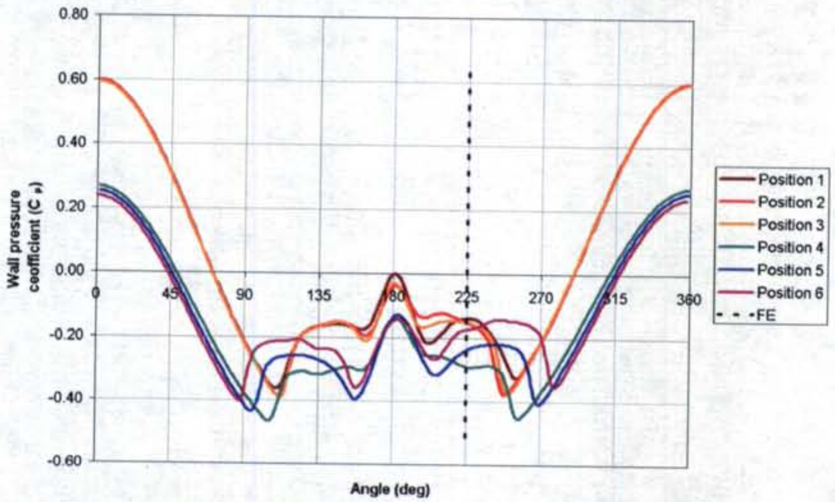

Figure C65 : Wall pressure profiles with 1 FE at 225° and 25° AOA

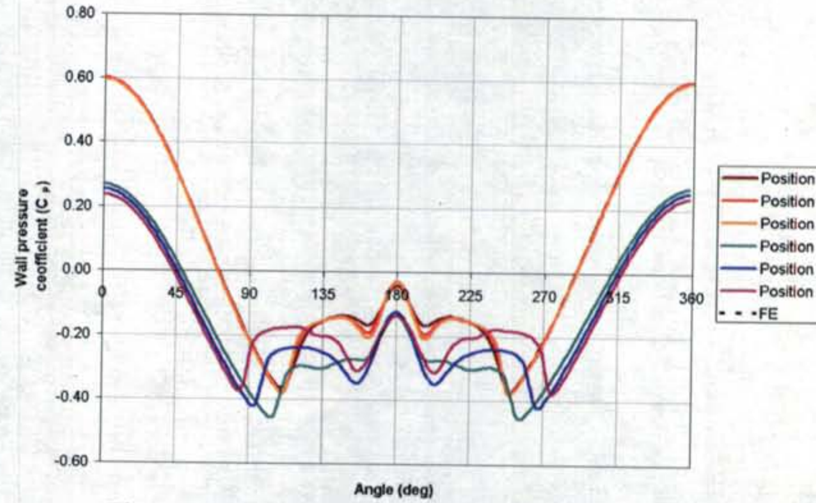

Figure C66 : Wall pressure profiles without FE and 25° AOA

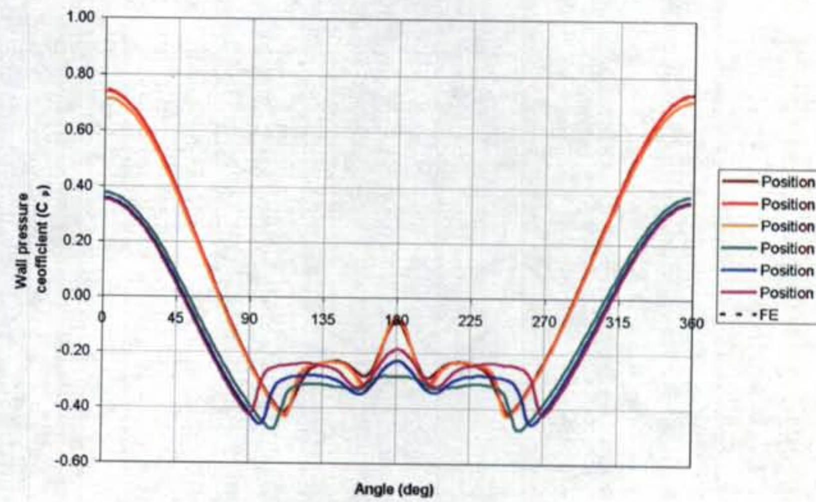

Figure C67 : Wall pressure profiles without FE and 30° AOA

APPENDIX D

COMPARISON OF WALL PRESSURE PROFILES

62

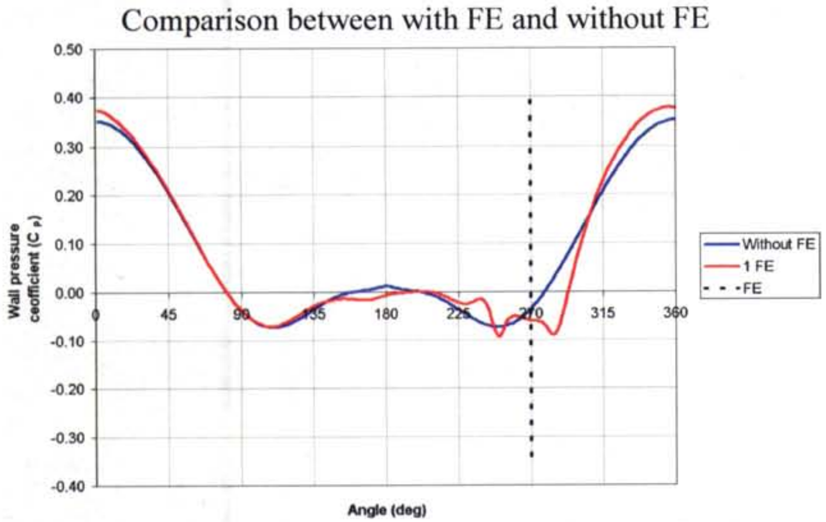

Figure D1 : Wall pressure profiles at 270° and 15° AOA with pressure tap 1

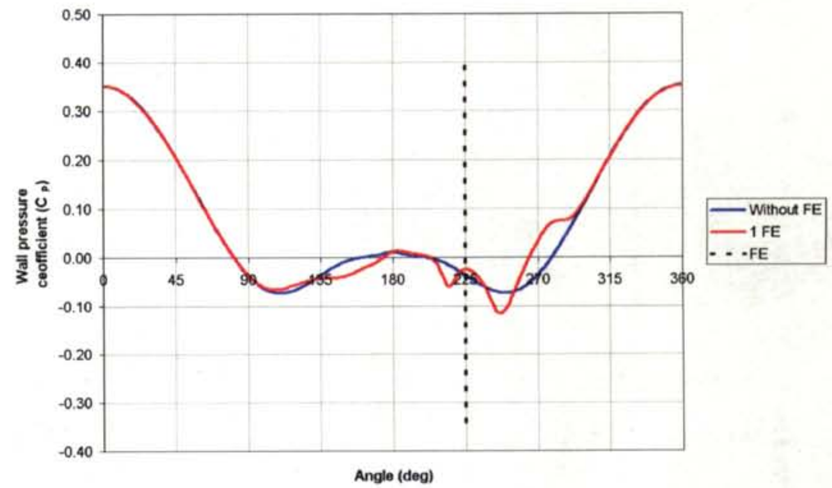

Figure D3 : Wall pressure profiles at 225° and 15° AOA with pressure tap 1

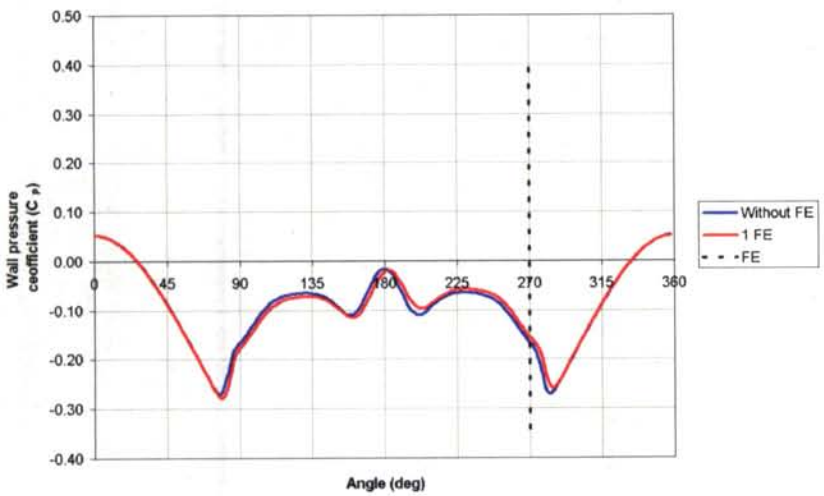

Figure D2 : Wall pressure profiles at 270° and 15° AOA with pressure tap 6

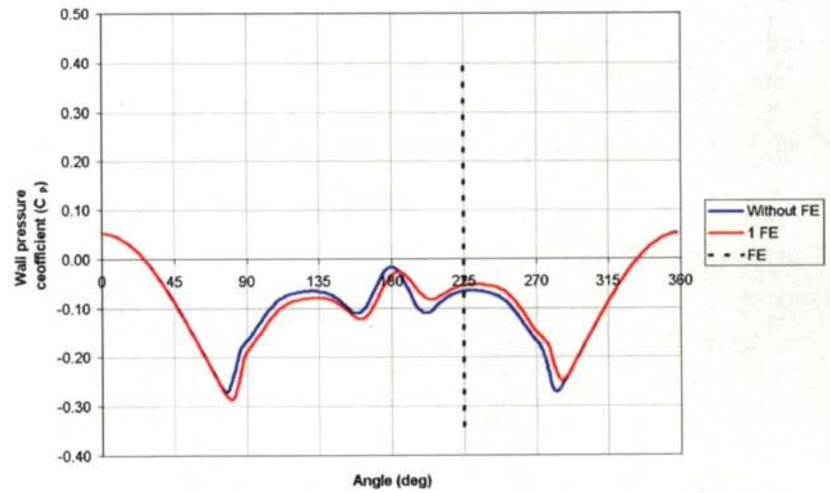

Figure D4 : Wall pressure profiles at 225° and 15° AOA with pressure tap 6

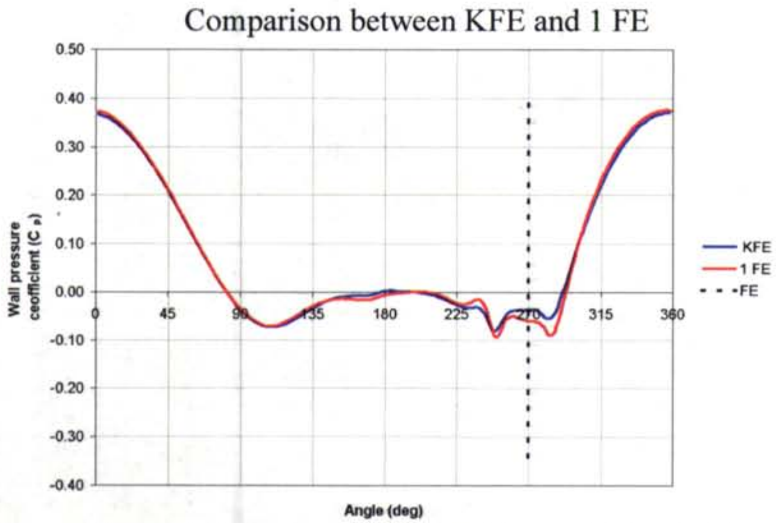

Figure D5 : Wall pressure profiles at 270° and 15° AOA with pressure tap 1

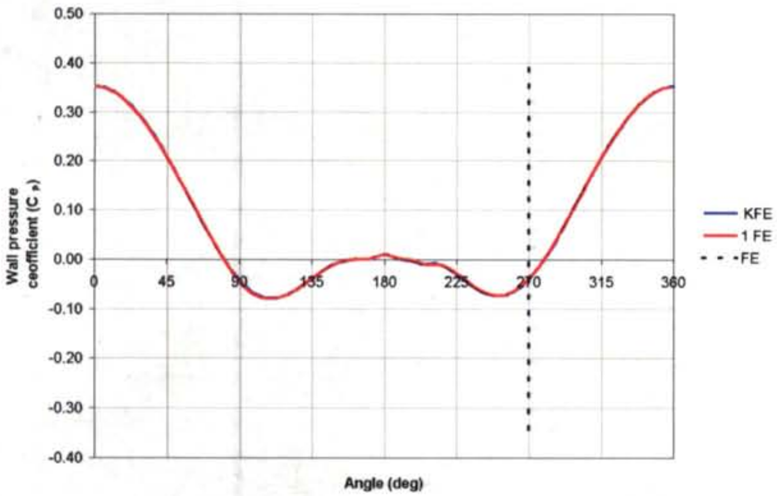

Figure D6 : Wall pressure profiles at 270° and 15° AOA with pressure tap 2

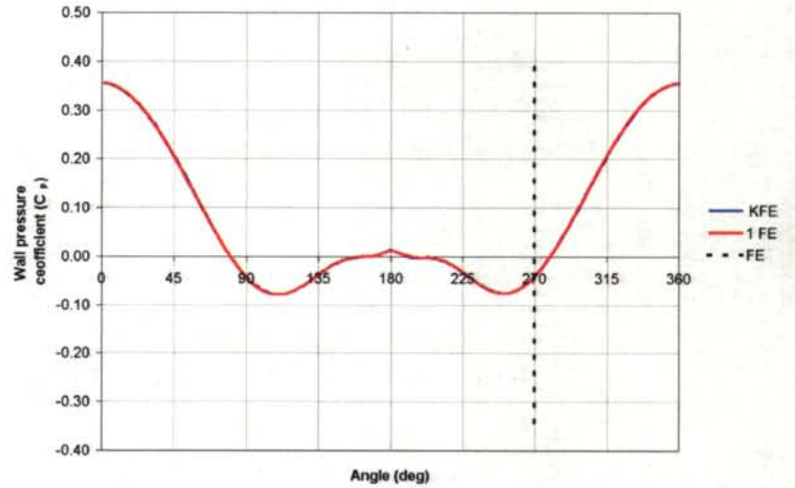

Figure D7 : Wall pressure profiles at 270° and 15° AOA with pressure tap 3

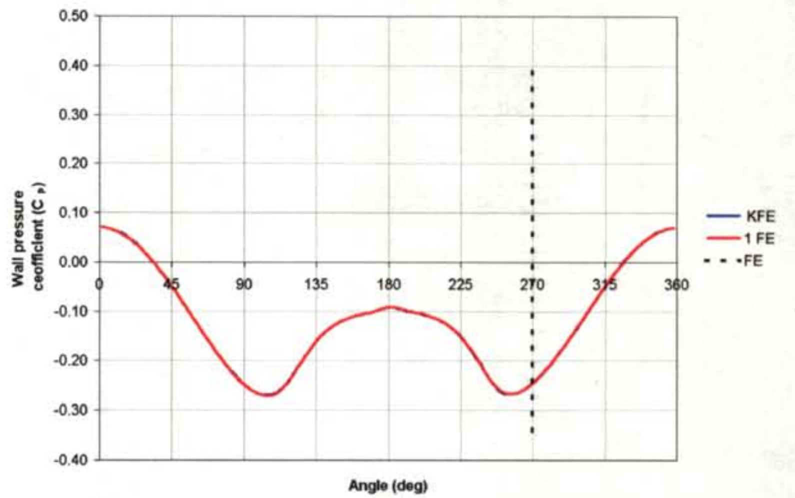

Figure D8 : Wall pressure profiles at 270° and 15° AOA with pressure tap 4

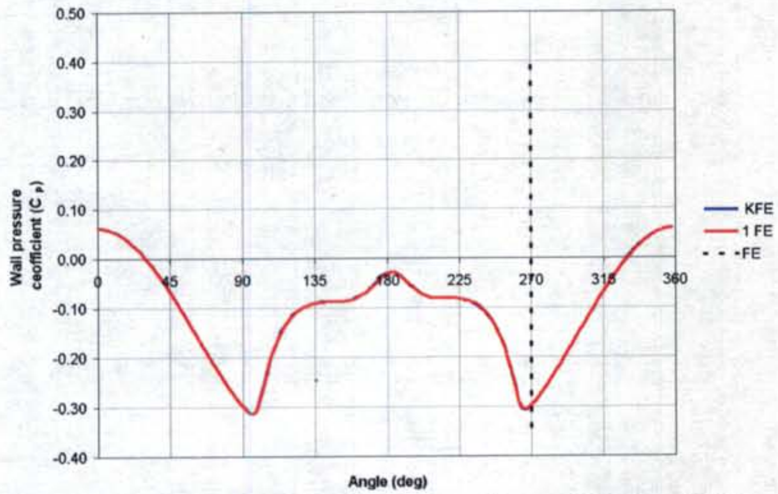

Figure D9 : Wall pressure profiles at 270° and 15° AOA with pressure tap 5

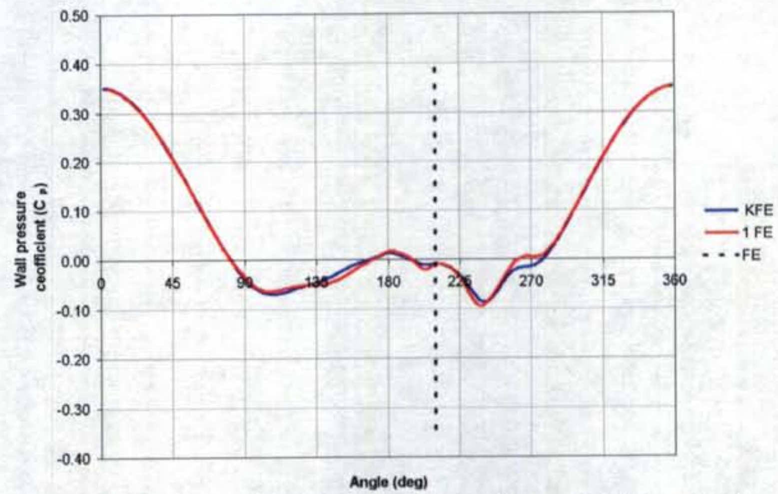

Figure D11 : Wall pressure profiles at 210° and 15° AOA with pressure tap 1

64

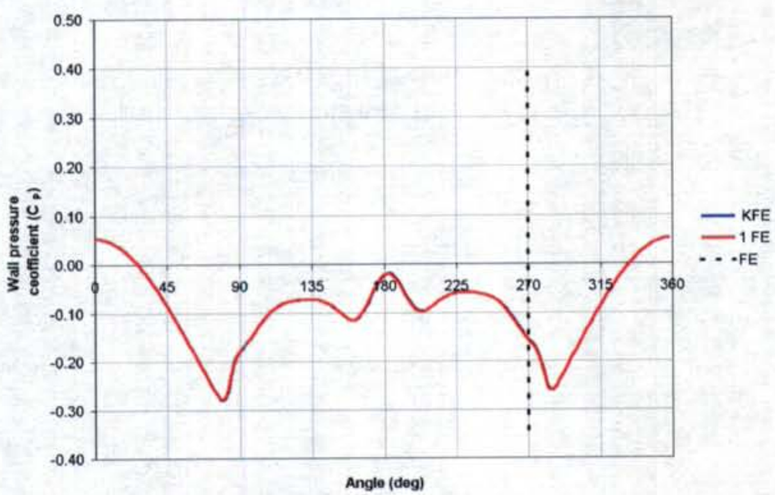

Figure D10 : Wall pressure profiles at 270° and 15° AOA with pressure tap 6

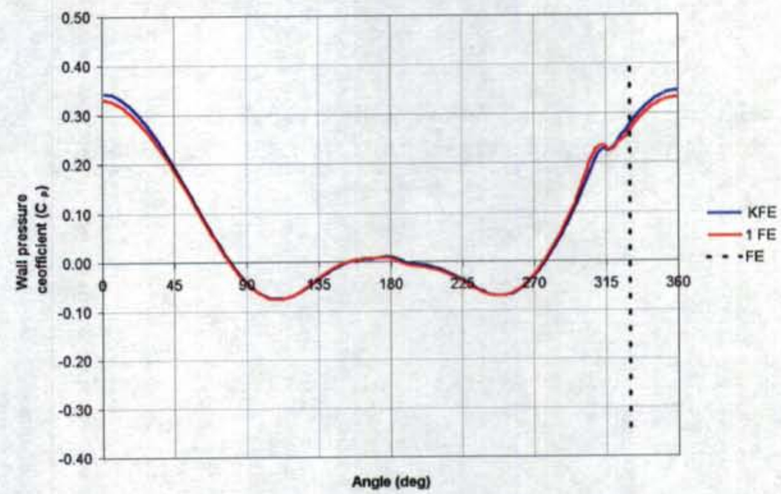

Figure D12 : Wall pressure profiles at 330° and 15° AOA with pressure tap 1

APPENDIX E

MISSILE AND FE GEOMETRY DRAWING

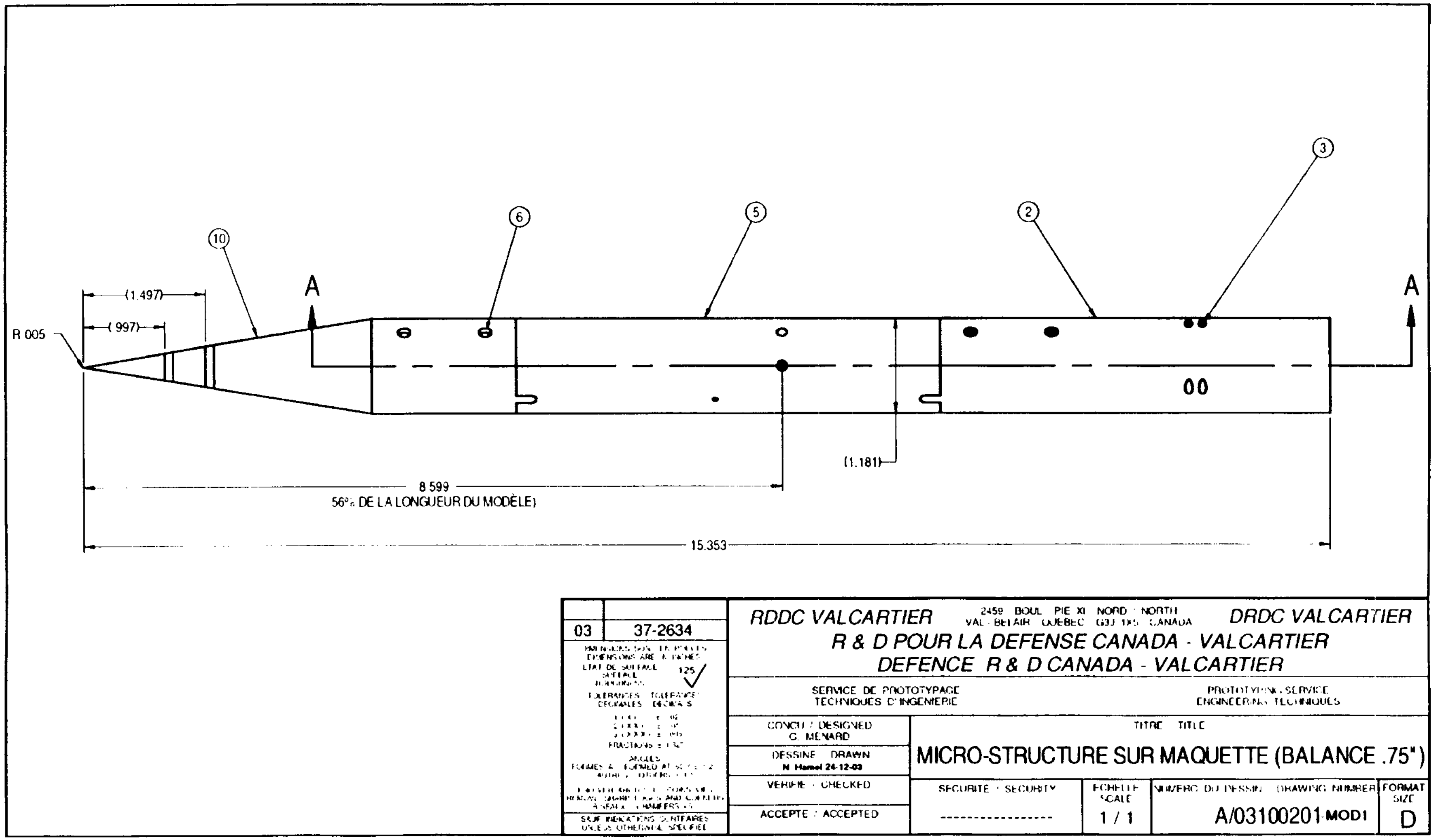

Figure E1 : Missile body dimension

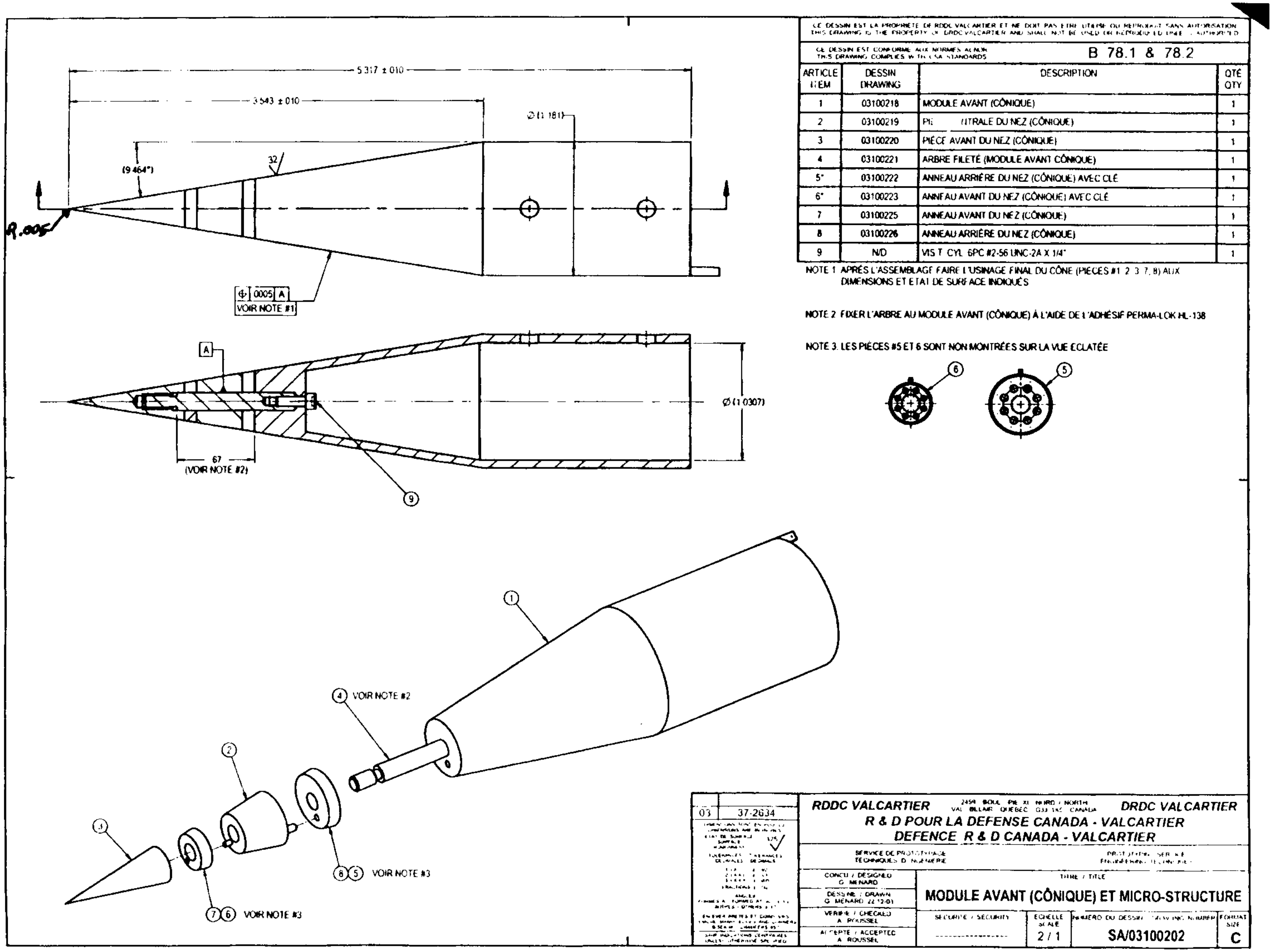

Figure E2 : Missile nose dimension and assembly

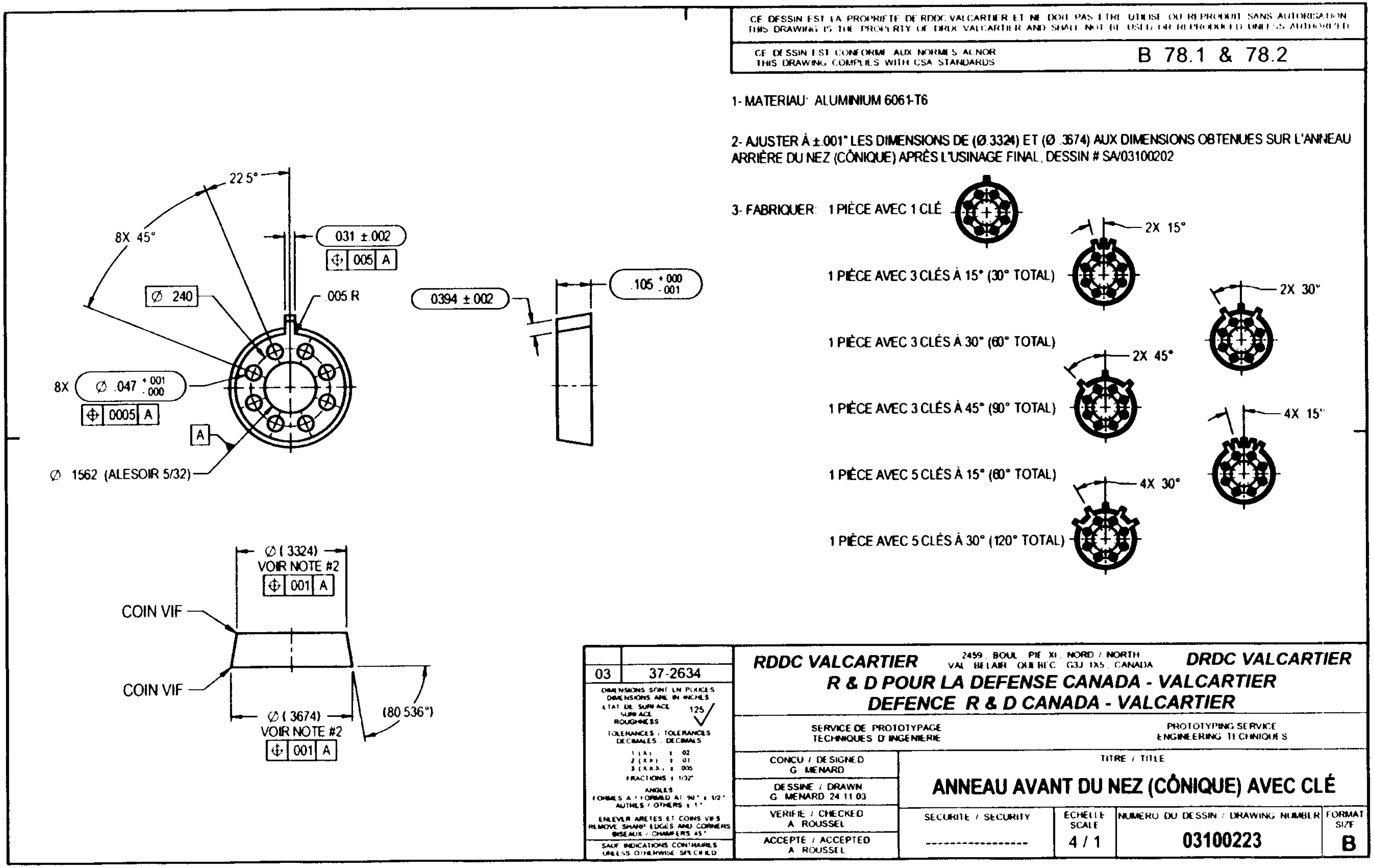

Figure E3 : FE dimension and position

Distribution List

INTERNAL DISTRIBUTION

1 – Deputy Direction General
3 – Document Library
1 – F. Wong
1 – É. Fournier
1 – F. Lesage
1 – D. Corriveau
1 – N. Hamel (Scientific Authority)
1 – C-A. Rabbath

EXTERNAL DISTRIBUTION

1 – Director Research and Development Knowledge & Information Management (unbound copy)
1 – Director Air Requirement 5
1 – Director Science and Technology Air
1 – Director Science and Technology Air 4
1 – Director Science and Technology Maritime
1 – Director Science and Technology Land

1 – M. Khalid
1 – S Chen
1 – S. McIlwain

Institute for Aerospace Research
National Research Council of Canada
Building U-66
1200 Montreal Road
Ottawa, ON, Canada
K1A 0R6

DOCUMENT CONTROL DATA

1. ORIGINATOR (name and address) Defence R&D Canada Valcartier 2459 Pie-XI Blvd. North Val-Bélair, QC G3J 1X8	2. SECURITY CLASSIFICATION (Including special warning terms if applicable) UNCLASSIFIED

3. TITLE (Its classification should be indicated by the appropriate abbreviation (S, C, R or U)
Performance Study for Guidance of a Missile using Flow Effectors at Different Roll Angle Positions (U)

4. AUTHORS (Last name, first name, middle initial. If military, show rank, e.g. Doe, Maj. John E.)
Rainville, Pierre-Antoine, Gosselin, Pierre

5. DATE OF PUBLICATION (month and year) December 2004	6a. NO. OF PAGES 66	6b .NO. OF REFERENCES 14

7. DESCRIPTIVE NOTES (the category of the document, e.g. technical report, technical note or memorandum. Give the inclusive dates when a specific reporting period is covered.)
Contract Report

8. SPONSORING ACTIVITY (name and address)

9a. PROJECT OR GRANT NO. (Please specify whether project or grant) 13eg16	9b. CONTRACT NO. W7701-0-24237/001/QCA
10a. ORIGINATOR'S DOCUMENT NUMBER DRDC-Valcartier-CR-2004-460	10b. OTHER DOCUMENT NOS N/A

11. DOCUMENT AVAILABILITY (any limitations on further dissemination of the document, other than those imposed by security classification)

- [x] Unlimited distribution
- [ ] Restricted to contractors in approved countries (specify)
- [ ] Restricted to Canadian contractors (with need-to-know)
- [ ] Restricted to Government (with need-to-know)
- [ ] Restricted to Defense departments
- [ ] Others

12. DOCUMENT ANNOUNCEMENT (any limitation to the bibliographic announcement of this document. This will normally correspond to the Document Availability (11). However, where further distribution (beyond the audience specified in 11) is possible, a wider announcement audience may be selected.)

13. ABSTRACT (a brief and factual summary of the document. It may also appear elsewhere in the body of the document itself. It is highly desirable that the abstract of classified documents be unclassified. Each paragraph of the abstract shall begin with an indication of the security classification of the information in the paragraph (unless the document itself is unclassified) represented as (S), (C), (R), or (U). It is not necessary to include here abstracts in both official languages unless the text is bilingual).

This project was part of DRDC technology investment found (TIF) project "Supersonic Missile Flight Control by Manipulation of the Flow Structure using Micro-Actuated Surfaces". The objective was to evaluate the performance of an active flow control in the form of a rectangular flow effectors and knife-edge flow effectors with the aim of controlling a missile. Flow effectors at different roll angle positions on the surface of the missile nose were evaluated numerically for their impact on overall system performance for a missile flying at angles of attack from five to twenty degrees.

A series of CFD analyses were carried out on an aerodynamic geometry with two different shapes of flow effectors. For the knife-edge flow effectors, five roll angle positions were analyzed. Seven roll angle positions with one rectangular flow effector and three roll angle positions with three rectangular flow effector were analysed. The experience gained during previous work was used as a guideline for determining the meshing strategy to be adopted, the turbulence model to be used with the correct near wall model with a Y+ around 1. From the gained experience, the mesh should be very fine and structured near the wall with a smooth mesh variation in the vortex perturbed region. The more accurate turbulence model was the realizable k-epsilon.

The calculations showed that a good side force generation was possible for one flow effector at roll angle position between 225 degrees and 270 degrees. Those results correlated well with wind tunnel measurement between 5 degrees and 15 degrees angle of attack. Calculations with three flow effectors showed a small improvement in the performance compared to the best performing single flow effector configuration. Finally, knife-edge flow effectors did not produce the same aerodynamic coefficients as the rectangular flow effector.

14. KEYWORDS, DESCRIPTORS or IDENTIFIERS (technically meaningful terms or short phrases that characterize a document and could be helpful in cataloguing the document. They should be selected so that no security classification is required. Identifiers, such as equipment model designation, trade name, military project code name, geographic location may also be included. If possible keywords should be selected from a published thesaurus, e.g. Thesaurus of Engineering and Scientific Terms (TEST) and that thesaurus-identified. If it is not possible to select indexing terms which are Unclassified, the classification of each should be indicated as with the title.)

Computational Fluids Dynamic, CFD, Flow Effectors, Active Flow Control, MEMS, Microstructure, Missile, Supersonic